Optical Coherence Tomography through Fibre Bundles by Angled Divergent Illumination

Hal Dorrington

School of Engineering, Mathematics and Physics

Supervisors: Prof. Adrian Podoleanu & Dr. Michael Hughes

18th July 2025

Abstract

Researchers have made numerous attempts to develop a fibre bundle Optical Coherence Tomography (OCT) system for endoscopy. However, in the 20 years since initial attempts [1], no approach has been successfully applied to clinical practice.

In this thesis, a novel method of performing OCT with a fibre bundle is presented. A compact adapter, that can transform a fibre bundle into a depth resolved imaging instrument, originally conceived as a concept in patent US11717154B2 'Imaging apparatus and method" [2], is experimentally realized, with initial results proving the validity of the concept.

The adapter enacts common-path fibre bundle OCT, utilizing angled divergent beams for the object and reference paths. These are delivered from a pair of single-mode-fibres, placed off-axis, making angled illumination onto the sample and the bundle face at 14°. At this large angular incidence of the reference beam onto the bundle, the light coupled within cores was not suitable for OCT, mainly due to a large degree of coupling into higher order modes, and a low overall coupling efficiency. Placing a thin diffuser at the bundle face achieved close to on-axis injection, enabling OCT to be performed.

A phantom consisting of metal and polymer features was imaged by the method of Full-Field Swept-Source OCT (FF-SS-OCT). It was observed that an apparent sample tilt could occur in the OCT images, owing to the superposition of angled divergent beams. However, if the two fibres are correctly aligned, the respective path lengths across the two beams effectively cancel out, and the true shape and orientation of the sample can be secured. B-scans and en-face slices identified features of the phantom, which were corroborated with scans obtained from a bench-top OCT system. With Fast Fourier Transform (FFT) processing, we secured a Signal-to-Noise Ratio (SNR) of 32 dB, and an axial resolution of 34 μm. Image processing by the Complex Master Slave (CMS) method was also explored. A significant improvement in axial resolution, reaching 20 μm, was achieved. However, the FFT method is currently preferred, as the CMS images had a poorer SNR of 27 dB, and suffered from artefact streaks.

In summary, the thesis has presented a new method of fibre bundle OCT. Rudimentary OCT imaging was demonstrated from a phantom, validating a new avenue of research towards the goal of achieving a forward-viewing Endoscopic OCT (E-OCT) system suitable for clinical enrolment. Several avenues for further research are suggested, that if perused may lead to clinical application of the new method.

Declaration

I declare that this thesis is a presentation of original research undertaken by myself for the degree of Doctor of Philosophy at the School of Engineering, Mathematics and Physics at the University of Kent.

I confirm that I have produced the work presented in this thesis, and that all contributions from other individuals have been appropriately acknowledged.

I confirm that the work presented in this thesis has not been submitted in whole or in part for any other degree at this or any other institution.

Word Count: 27,763
Number of Pages: 148

Name: Hal Dorrington

Signature:

HG Dorrington

Date: 18th July 2025

Dissemination of Research

This section lists dissemination of research resulting from the work presented in the thesis.

Publication Under Review

1. **Dorrington, H.**, Hughes, M., Podoleanu, A. (2025). *Forward-viewing full-field fiber bundle optical coherence tomography via off-axis divergent illumination.* Submitted to Journal of Optics Letters. [Under Review]

Conference Presentations

1. **Dorrington, H.**, Hughes, M., Podoleanu, A. “Miniature optical assembly solutions for fibre-bundle OCT.” *Presented at NETLAS Hybrid Conference, Canterbury, UK, (2024).*
2. **Dorrington, H.**, Hughes, M., Podoleanu, A. “Off-axis Divergent Sample Illumination and Off-axis Divergent Reference Wave for Fiber-bundle Full-field Optical Coherence Tomography.” *Presented at Photonics West, San Francisco, USA, (2024).*

3. **Dorrington, H.**, Hughes, M., Podoleanu, A. "Off-axis divergent superposition for full-field fibre-bundle optical coherence tomography." *Presented at World Congress ICO-25-OWLS-16, TU Dresden, Germany, (2022).*

4. **Dorrington, H.**, Hughes, M., Podoleanu, A."Endoscopic full-field imaging and optical coherence tomography through a fibre bundle" *Presented at Prof. Adrian Podoleanu's Career Celebration, University of Kent, Canterbury, (2022)*

5. **Dorrington, H.**, Hughes, M., Podoleanu, A. "Multicore Fibre Bundle Approach for Full-field Endoscopic Optical Coherence Tomography." *Presented at School of Physical Sciences (SPS) Postgraduate Colloquium, University of Kent, Canterbury, UK, (2020)*

Acknowledgments

EPSRC Funding

I acknowledge the Engineering and Physical Sciences Research Council (EPSRC) under Doctoral Training Account (DTA) studentship, 2290196, for funding my doctoral studentship.

Patent Disclosure

I acknowledge Dr. Michael Hughes and Dr. Adrian Podoleanu as the original inventors on patent US11717154B2 “Imaging apparatus and method”, assigned to the University of Kent. The work presented in this thesis has been based on the designs proposed in this patent.

Code Authorship

I acknowledge the original authors of certain pieces of code that I have adopted and subsequently modified towards functioning with my system.

I received help with camera integration and data collection in LabView from Dr. Manuel Marques. I adopted a simple working example code and subsequently adapted it to perform FF-SS-OCT. Manuel provided technical support in this process, particularly in my first year.

Sections of the CMS MATLAB code, executing the measurement of the g and h functions, and the matrix multiplication to produce a volume, were originally written by Dr. Adrian Bradu. I received a modified version from Dr. Alejandro Martinez Jimenez, who had made some slight alterations. I subsequently developed this script so as to work with the data collected from my system.

Contents

List of Acronyms

OCT	Optical Coherence Tomography
FF-SS-OCT	Full-field Swept Source OCT
FFT	Fast Fourier Transform
CMS	Complex Master-Slave
E-OCT	Endoscopic OCT
SNR	Signal-to-Noise Ratio
NIR	Near-Infra-Red
LCI	Low Coherence Interferometry
A-Scan	Amplitude Scan
OPD	Optical Path Difference
TD-OCT	Time-Domain OCT
FWHM	Full Width Half Maximum
FD-OCT	Fourier-Domain OCT
Sb-OCT	Spectrometer-based OCT
SS-OCT	Swept Source OCT
B-Scan	Brightness-Scan
FF-OCT	Full-field OCT
FV-E-OCT	Forward-Viewing E-OCT
MEMS	Micro-electro-mechanical systems
FOV	Field-of-View
FT	Fourier Transform
PVD	Phase Velocity Dispersion
GVD	Group Velocity Dispersion
DFT	Discrete Fourier Transform
MS	Master Slave

NA	Numerical Aperture
MO	Microscope Objective
GRIN	Gradient Index Lens
SMF	Single-mode-fibre
PCX	Plano-convex
RMS	Root Mean Square
PSF	Point Spread Function
PC	Polarization Controller
FG	Function Generator
COAX	Co-Axial (Cable)
TTL	Transistor-Transistor Logic
CL	Camera Link
VI	Virtual Instrument
TIFF	Tagged Image File Format
CS	Channelled Spectrum

List of Figures

List of Tables

Thesis Overview

Motivation

Endoscopic Optical Coherence Tomography (E-OCT) is a new medical imaging technique, providing high resolution 3D images in real-time from internal organs. Typically, E-OCT utilizes an optical fibre probe, with scanning at the distal end, [3]. However, the only widespread clinical adoption of E-OCT has been 'side-viewing', [4], which is only well-suited to imaging along tract-like organs.

There is a desire for forward-viewing E-OCT, for organs in which side-viewing is not appropriate. However this has been hard to achieve in practice, mainly due to the difficulty of assembling forward-viewing scanners, that can be contained within an endoscope, yet are capable of obtaining clear images. Any reported cases have been unsuitable for clinical application, due to, for instance; being too wide [5], having too low frame rates leading to motion blurring [4], or simply having an insufficient image quality and field-of-view [6].

Researchers have proposed an alternative approach of using an imaging fibre bundle [7], a thin and flexible imaging conduit formed from several thousands of optical fibre-cores. A fibre bundle OCT system could achieve a forward-view without the need for either proximal or distal scanners, instead utilizing a wide field beam to image across an extended field-of-view simultaneously, i.e. in a Full-field OCT set-up.

Several approaches to fibre bundle OCT have been explored over the 20 years since initial attempts [1], however, due to technical difficulties, none have been suitable for clinical practice [8], [9]. Fibre bundles present several issues for OCT, and there exists a desire for alternative solutions that can bypass or mitigate these problems.

Thesis

The thesis presents and validates a new method of performing fibre bundle OCT. A compact adapter amenable to miniaturization, is shown to transform a fibre bundle into a depth resolved imaging instrument. With further miniaturization and refinement of sensitivity, the new design could present a means of achieving a forward-viewing E-OCT system suitable for clinical application.

The novelty of the new design lies in the optical arrangement of object and reference beams at the distal end of the bundle. It utilizes angled divergent illumination from single-mode-fibres to derive object and reference beams, which are superimposed at the distal face of the bundle to create a common-path coupling of the two beams. This arrangement by-passes the requirement for a beam-splitter at the distal end, providing a common-path implementation, whilst retaining a compact geometry well suited to endoscopy.

Chapter Breakdown

Chapter 1 - Introduction

This chapter introduces the reader to the basics of OCT and describes methods of E-OCT. We expand on the motivation for forward-viewing E-OCT, and introduce fibre bundles as an alternative solution. Problems with previously proposed fibre bundle OCT systems are summarised. The motivation for the new method is established and the newly proposed design is introduced.

Chapter 2 - Full-Field Swept Source OCT

This chapter describes the theory of Full-field Swept Source OCT (FF-SS-OCT), the established imaging technique foundational to the presented system.

Chapter 3 - Angled Divergent Beam Injection of Fibre Bundle Cores using a Diffuser

In this chapter, we perform experimentation with a Schott leached fibre bundle. Imaging of the distal end of the bundle onto a camera is first established. We then experiment with coupling of an angled divergent beam through the bundle. Coupling efficiency and modal behaviour are characterized, and it is concluded that the coupling is unsuitable for OCT. A solution is then presented, using a thin diffuser flush at the bundle face to achieve near to on-axis coupling. Coupling efficiency and modal behaviour are compared with and without the diffuser, and a coupling suitable for OCT is established when the diffuser is in place.

Chapter 4 - Fibre Bundle OCT Adapter

This chapter presents the new fibre bundle OCT adapter, which is based upon a 4f-telescope, equipped with angled illumination from the ends of object and reference fibres.

Experimentation of the adapter is conducted in two parts. The telescope is first assembled within a 3D-printed casing and the object fibre introduced to perform imaging of a phantom, which is used to calibrate the system. Imaging of a USAF test target is then performed to assess lateral resolution, and a Gaussian smoothing filter applied to remove the core pattern.

In the second part, the reference fibre is introduced, and OCT is performed. The effect of an apparent sample tilt due to the superposition of angled divergent beams is evaluated for two cases, a misaligned and a correctly aligned case, concluding that an approximately true representation of the sample tilt can be secured, provided the two fibres are correctly aligned.

This chapter also briefly describes the bulk aspects of the FF-SS-OCT system in which the adapter and fibre bundle operate. This includes the methods of source sweeping and the synchronized acquisition of images from the camera.

Chapter 5 - OCT Results and Image Processing Methods

This chapter presents OCT images acquired with the adapter and processed via two different methods, by FFT and by CMS. In both cases B-scans and en-face images of the phantom are presented. Quantitative metrics such as axial resolution and Signal-Noise Ratio (SNR) are characterized for the two methods.

The chapter also presents a protocol developed in MATLAB to implement the method of CMS processing. This involves band-pass filtering of raw calibration spectra, which enabled masks to be synthesized, from which an OCT volume was produced.

Chapter 6 - Conclusion

The thesis finishes with a concluding chapter. Here we assess the success of the thesis, and discuss the causes of difficulties in achieving clear images. This chapter presents avenues for further research, with the ultimate goal of developing a forward-viewing E-OCT system, from a fibre bundle, that could be employed to endoscopy.

Chapter 1

Introduction

1.1 Chapter Overview

Fibre bundles are a promising solution to the difficulties of conventional scanning based forward-viewing E-OCT. However, fibre bundles present several difficulties for OCT, and no previously proposed method has been suitable for clinical practice.

In this chapter we introduce the reader to OCT, and to the more specialised form of E-OCT, in which we motivate forward-viewing E-OCT as a potential tool for high resolution *in-situ* imaging of internal organs.

We describe some of the technical difficulties of fibre bundle OCT, and motivate the desire for new approaches. The chapter is concluded by briefly describing the proposed method presented in the thesis.

1.2 Optical Coherence Tomography

Optical Coherence Tomography (OCT) [10] is a non-invasive optical imaging modality, used principally in medicine for high resolution real-time imaging of tissue *in-vivo*. It applies the principles of interferometry with low-coherence light to obtain depth-resolved cross-sectional images, typically with 10-20 μm resolution at 1-2 mm of depth. With this depth range and resolution, OCT is extremely well suited for high resolution imaging of epithelial tissue, serving as a promising tool for early-stage detection of dysplasia and malignancies [11]. An example of a typical OCT cross-sectional image, obtained from a healthy retina, is given in Fig. 1.1

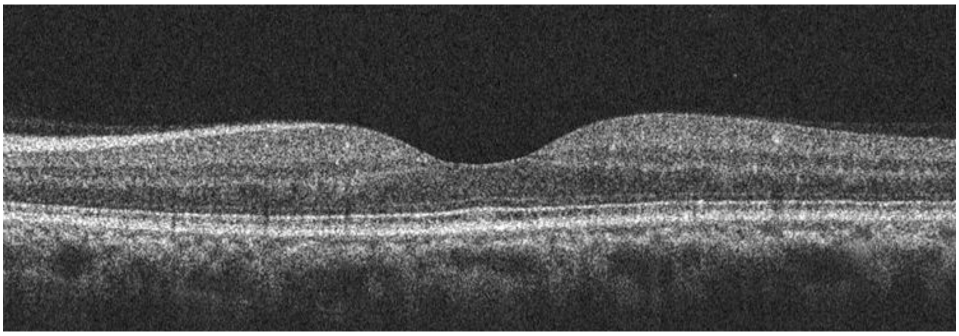

Figure 1.1: Example OCT image of a healthy retina, reproduced from [12].

OCT is perhaps one of the most promising tools for *in-situ* imaging of epithelial lesions, offering a unique balance of resolution and depth, effectively occupying a niche between Confocal Microscopy and Ultrasound, as illustrated in Fig. 1.2. The former can offer sub μm resolution but typically only tens of μm of depth, not penetrating to the deeper epithelial structures. Conversely, Ultrasound can penetrate to several cm but typically with poorer than 100 μm resolution, not sufficient for detailed imaging of tissue morphology.

OCT has also shown promise as a tool for the guiding of biopsies. Recent work has demonstrated that OCT can be performed onto tissue at the biopsy needle tip, offering greater resolution and

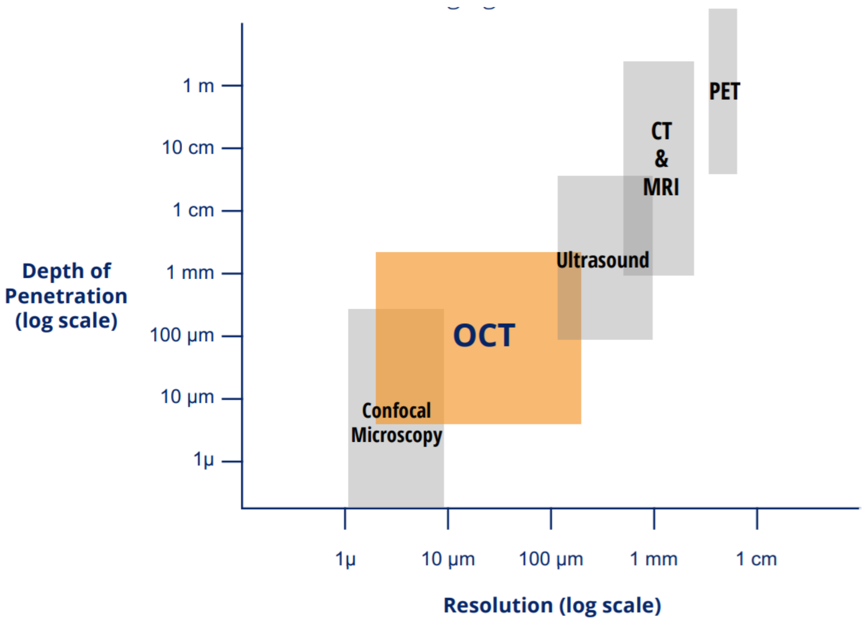

Figure 1.2: Imaging depth against resolution, for OCT vs competing imaging modalities [13].

hence potentially improved localisation of tissue when compared to conventional ultrasound-guided biopsies [14], [15].

Like Confocal Microscopy and Ultrasound, OCT is also a non-invasive method of imaging. It uses low power non-ionizing light, typically in the Near-Infra-Red (NIR) wavelength range. Unlike a biopsy or a scan with ionizing radiation, OCT does not cause any disturbance or harm to the tissue. This means the *in-vivo* micro-physiology of an organ can be observed in real-time [16], all without causing any harm to the patient.

OCT has been very successful in niche areas of medical imaging. It is most prominent in ophthalmology, where it has revolutionized the diagnosis of retinal diseases such as macular degeneration and glaucoma [17]. It has also received clinical adoption into other areas of medicine, such as; cardiology, dermatology, and intraoperative guidance. Many extended functionalities of OCT also exist, such as Doppler-OCT and OCT-Angiography, which provide additional functional information such as blood flow, and are readily used in ophthalmology and cardiology [18].

1.2.1 OCT Basics

OCT is based on the principle of Low Coherence Interferometry (LCI), in which a low-coherence light source is used in an interferometric setup to perform depth-resolved reflectometry through a sample [19]. LCI produces an axial profile of reflectivity through the sample, called an Amplitude scan (A-scan), which reveals the locations and reflectivities of internal scattering layers. To illustrate this principle, we consider a sample with well-spaced flat layers, which are all aligned and facing the OCT systems objective lens. In practice, tissue morphology is more complex, although this is a reasonable approximation for the epithelial tissue of the retina. An illustration of an A-scan corresponding to such a sample is shown in Fig. 1.3.

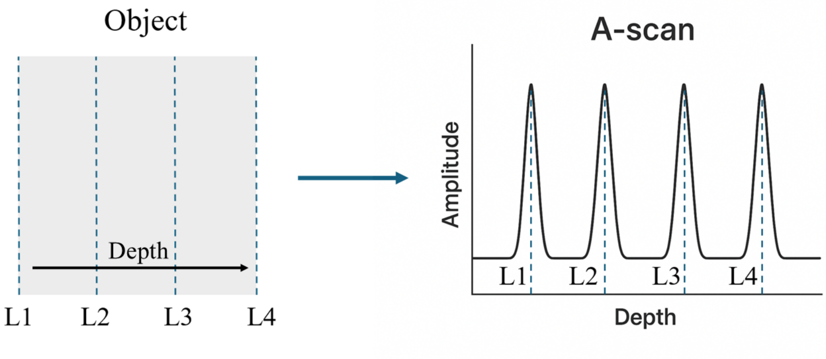

Figure 1.3: Illustration of an A-scan obtained from a layered object, whereby each reflecting layer, L1 to L4, is represented by a peak in the A-scan.

A typical LCI setup uses a Michelson interferometer, which can be implemented either in 'in-bulk', using a beam splitter, or 'in-fibre', using a fibre coupler; in either case to divide the optical power between object and reference arms.

An example of an LCI system using a fibre coupler is illustrated in Fig. 1.4. A field of low-coherence light, E_S, emitted by a broadband source reaches the fibre coupler, where its optical field is split between the object and reference arms. Assuming a lossless 50:50 coupling ratio, each arm receives half of the input fields optical power, or in terms of field amplitude, $E_S/\sqrt{2}$. At the distal end of the object arm, light is focused onto a sample, and the light backscattered from the sample is focused back into the object fibre. Similarly, in the reference arm, the light is reflected from a reference mirror and re-coupled into the reference fibre. The two returning fields, E_O and E_R, are recombined at the coupler and directed to a detector.

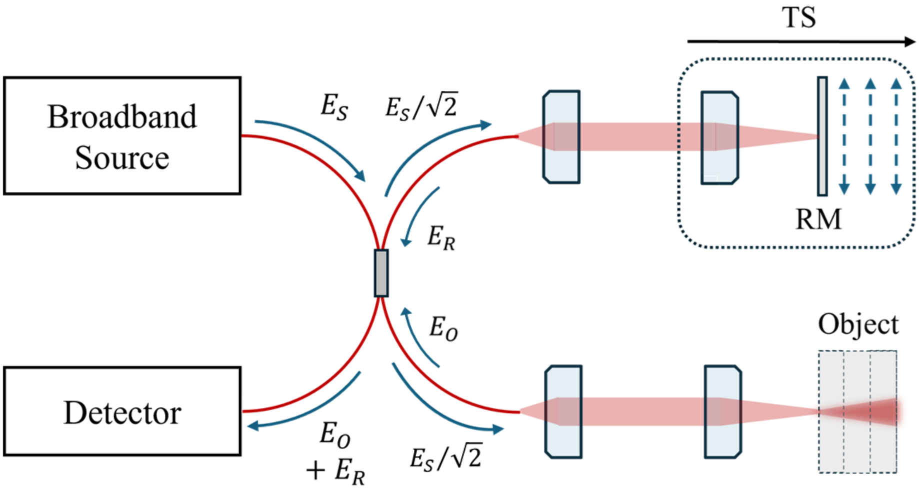

Figure 1.4: Illustration of a possible LCI system, utilizing a fibre coupler. A reference mirror (RM) is positioned on a translation stage (TS) to facilitate axial scanning.

At the detector, the optical field is measured over a finite integration time, τ. Since optical detectors follow square-law detection, the measured signal intensity, I, is the time-averaged intensity over the given integration time, given by:

$$I = \left\langle |E_O + E_R|^2 \right\rangle_\tau \tag{1.1}$$

If the optical path difference (OPD) between the two arms of the interferometer is smaller than the coherence length of the source, l_c, the fields can interfere, and the detected intensity is different from the sum of the individual intensities of each arm, I_O and I_R. That is:

$$I \neq I_O + I_R \tag{1.2}$$

When interference occurs, the detected intensity contains a modulation term, dependent on the phase difference $\Delta\phi$ between the two superimposed fields. The interference signal is given by:

$$I(\Delta\phi) = I_O + I_R + 2\sqrt{I_O I_R} \cdot \cos(\Delta\phi) \tag{1.3}$$

Interference occurs only when the OPD is within the coherence length, l_c, of the light source. This principle forms the physical basis of depth sectioning in LCI. A similar set up is used to perform depth sectioning in the originally conceived form of OCT, called Time-Domain OCT (TD-OCT).

Depth Sectioning and Axial Resolution

The object field at the detector contains light backscattered from all scattering layers of the sample simultaneously. However, only light scattered from a depth whereby the OPD is less than l_c will contribute to the interference signal at any moment. This property enacts optical sectioning in depth.

The axial resolution in LCI and TD-OCT is thereby determined by the coherence length of the source. According to the Wiener–Khinchin theorem, the temporal coherence function and the power spectral density of a light source form a Fourier transform pair. This means that the coherence length is determined from the bandwidth of the broadband spectrum, and to a lesser extent, by its central wavelength. For a Gaussian spectrum, the coherence length is given by:

$$l_c = \frac{2\ln 2}{\pi} \cdot \frac{\lambda_0^2}{\Delta\lambda} \tag{1.4}$$

where λ_0 is the central wavelength, and $\Delta\lambda$ is the bandwidth of the source.

In Fig. 1.3, it is illustrated that the Full Width Half Maximum (FWHM) of each peak in the A-scan corresponds to the coherence length of the source.

Axial scanning

In the original implementation of OCT, known as Time-Domain OCT (TD-OCT), axial scanning is achieved by translating the reference mirror along the optical axis. When the reference arm length matches that of a backscattering layer in the sample, to within an extent of l_c, an interference signal is detected. By recording the interference amplitude as the mirror is scanned, a depth-resolved A-scan is constructed.

Fourier Domain OCT

An alternative and more efficient approach is Fourier-Domain OCT (FD-OCT), which eliminates the need for mechanical axial scanning. Instead of translating the reference mirror, FD-OCT measures interference over optical frequency. This is achieved either with a spectrometer, called Spectrometer-based OCT (Sb-OCT), or with a wavelength tuned source, called Swept-Source OCT (SS-OCT).

Assuming a single reflective layer in the sample, the detected interference signal in FD-OCT takes the form:

$$I(k) = I_O(k) + I_R(k) + 2\sqrt{I_O(k)I_R(k)} \cdot \cos(2kz) \tag{1.5}$$

where $k = 2\pi/\lambda$ is the wavenumber, and z is the axial position of the scattering layer relative to the reference arm. Depth information is encoded in oscillations in wavenumber space. By applying a Fourier transform to $I(k)$, one obtains the reflectivity profile as a function of depth, i.e the A-scan, A(z):

$$A(z) = \mathcal{F}\left[I(k)\right] \tag{1.6}$$

This Fourier-domain approach offers several advantages over TD-OCT: it provides higher sensitivity [20], and faster acquisition rates, since no mechanical scanning is required to form A-scans.

The two FD-OCT approaches differ in their method of resolving frequency components. In Sb-OCT, a spectrometer is used to resolve components from a broadband source. In SS-OCT, a narrow-linewidth laser, typically with an instantaneous bandwidth in the range of 10 to 100 pico-meters, is tuned in wavelength to synthesize a broadband spectrum. A narrow instantaneous bandwidth of this order is required to secure imaging over a depth range of several mm to a few cm.

1.2.2 Lateralization: Point-Scanning vs Full-field

OCT was invented in the early 1990s, when Huang et al. [10] extended the A-scan principle into 3D imaging of biological tissue. This was achieved by laterally scanning a focused beam across a sample and sequentially acquiring A-scans to form a cross-sectional scan. A sequence of A-scans along one lateral direction forms a two-dimensional cross-section, known as a Brightness-scan (B-Scan), as in Fig. 1.1. By introducing a second lateral scanning axis, multiple B-scans can be acquired and assembled into a 3D image. This approach of scanning of a focused beam is often referred to as Point-scanning OCT.

An alternative approach called Full-field OCT (FF-OCT), was later introduced [21]. In FF-OCT, extended beams are used in the object and reference paths, with the sample illuminated over a full field-of-view (FOV) simultaneously. This by-passes the need for lateral scanning, although presents its own difficulties, such as cross-talk [22].

1.3 Endoscopic-OCT (E-OCT)

One of the major areas of research within the OCT community is the application of OCT to endoscopy, referred to as Endoscopic-OCT (E-OCT) [4]. Typically, an optical fibre probe is relayed through an endoscope, and the emitted beam scanned across tissue *in-situ* to perform OCT.

The extension of OCT to endoscopy has opened a wide range of new applications. In theory, an E-OCT system is able to perform an OCT scan onto any external region of the body, at locations not easily accessed with an 'in-bulk' system, as well as onto tissues of internal organs, accessed through natural orifices. Needle-like E-OCT systems have also been proposed [23], [24], which could be inserted to deeper regions of the body, not accessible through a natural orifice.

E-OCT could potentially serve as an effective means of performing high resolution morphological assessment *in-situ*, either from a region over the body or from an internal organ. Currently, in endoscopy, to achieve micron-scale resolution imaging of a suspicious region of an organ for diagnosis, a physical excision of tissue is extracted and prepared for *ex-vivo* histological examination under a microscope. This procedure takes up resources and time. By the practice of E-OCT a similar examination could be made instantly, enabling for a quick diagnosis. For time-crucial diseases such as the growth of cancerous tissue, this could mean early detection and hence earlier treatment. An E-OCT screening could be relatively quick, easy, and affordable to perform, when compared to a biopsy and the subsequent processing of biopsy samples. This could have the effect of making examinations more readily available, and is very attractive for organs such as the throat and lungs [25], [26].

An E-OCT optical biopsy may also enable for the living dynamics of an organ to be observed in real-time. This real-time visualization has been suggested for assessment of hollow organs such as the gastrointestinal or respiratory tract [27].

The conventional practice of excision also comes with the risk of complications, such as a rupture to vessels, infection, and in some cases, causing a spread of cancerous tissue, although the risk of this happening is typically very low [28]. Another weakness in typical excision-based biopsy is that of under sampling, by which a malignant tissue may go undetected. With E-OCT, an unlimited number of scans could be taken, and hence adequate sampling would be ensured. Another application of E-OCT may be as a surgical aid, acting as an accurate guidance tool for delicate operations.

1.3.1 Side-viewing E-OCT

A key factor to the motivation of the thesis is the understanding that most E-OCT systems currently enrolled into clinical settings have only achieved a side-viewing mode of operation. Side-viewing E-OCT has been performed in a number of ways. In most cases the beam is emitted at 90°to the fibre end, typically achieved with a prism or a mirror at the distal end. This is accompanied by translation of the fibre through an organ to acquire the third dimension and create an OCT volume.

One such successful approach is that of radial scanning, in which an orthogonal emitted beam is circumferentially scanned while the fibre probe is translated through a lumenal organ [29]. An illustration of side-viewing E-OCT by radial scanning is given in Fig. 1.5, in which an emitted beam is deflected at 90°by a small mirror, and focused onto the tissue through a lens.

Side-viewing E-OCT is straightforward to miniaturize but is only well-suited to imaging luminal organs such as the gastrointestinal tract, as well narrower organs such as the arteriole and pulmonary vessels.

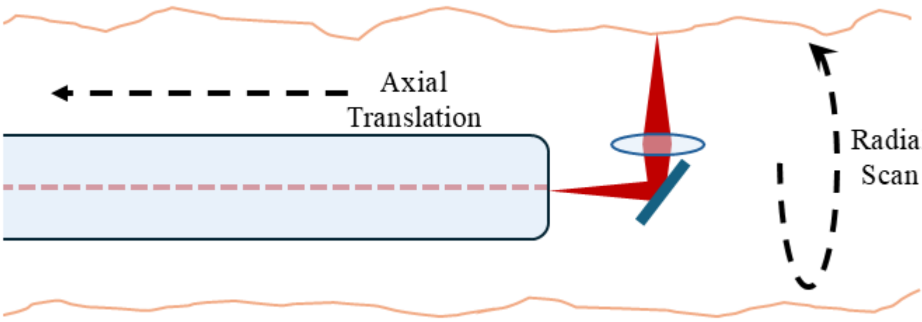

Figure 1.5: Illustration of Side-viewing E-OCT, by radial scanning with axial translation.

Clinical success

Side-viewing E-OCT has had notable clinical success in intravascular imaging. Commercially available systems have been developed by Abbott Laboratories, such as OPTIS™ [30]. These systems deliver highly accurate imaging and systematic quantification of the morphology and plaque deposits along arteries and veins, providing greatly improved resolution over previously established methods such as intravascular ultrasound. Such commercialized systems serve as a good example of the possible translation of E-OCT technologies from physical and engineering principles into a matured clinical practice.

1.4 Forward-viewing E-OCT

There is a strong desire for Forward-viewing E-OCT (FV-E-OCT), as there are many forms of endoscopy for which the side-viewing mode is not appropriate. One example is for imaging within the upper airway, ear, nose and throat. Currently, in such examinations, forward-viewing imaging is only performed at the macroscopic level, imaging large regions of an organ without any imaging from below the surface. As such, taking excisions is the common practice for sub-surface examination. A forward-viewing OCT endoscope would enable for structural imaging of tissue from below the surface and is hence very desirable in the pursuit of *in-situ* micron-scale imaging from non lumenal-like organs.

However, it has been difficult to achieve a forward-viewing E-OCT system, principally as it is hard to contain forward-viewing scanners at the endoscope tip that are sufficiently small, yet capable of capturing high quality images with a large field-of-view and at real-time speeds. To date, FV-E-OCT has only been demonstrated in research settings, where it is typically performed with micro-electro-mechanical systems (MEMS), with scanners *in-situ* at the 'distal' end of the endoscope [31], [32]. Designs incorporating MEMS also require an externally supplied driving voltage which could cause harm to the tissue if not correctly contained [31].

1.4.1 Fibre bundles for FV-E-OCT

A possible means of performing FV-E-OCT is to utilize an imaging fibre bundle. Fibre bundles are thin and highly flexible light conduits, formed from a plurality of optical fibre cores bundled together within a single cladding.

Imaging fibre bundles are a special case, in which the arrangement of cores at each end of the bundle are matched. As illustrated in Fig. 1.6, an image projected at the distal end is transported though the bundle, and a pixelated image, resembling the core pattern, is projected from the proximal end, with each fibre core effectively acting as a single pixel. Typical bundles can house up to tens of thousands of fibre cores within a mm order diameter, enabling for a high resolution image to be retrieved through an endoscope.

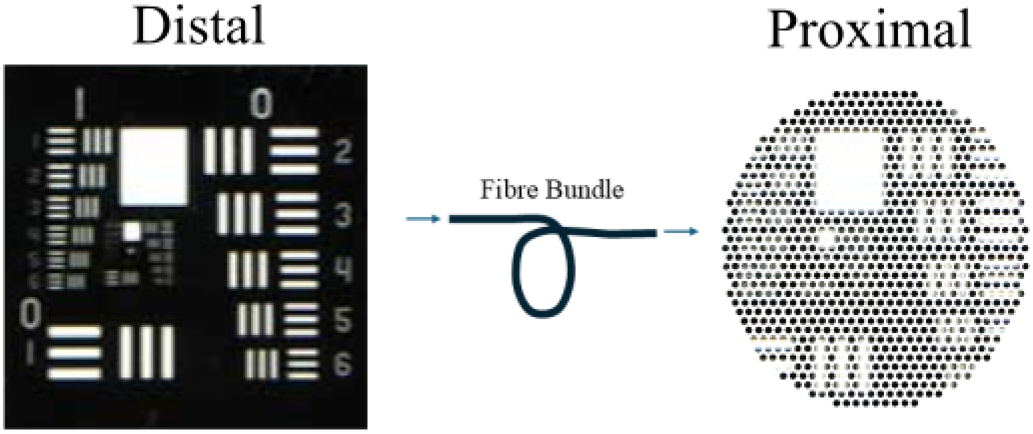

Figure 1.6: Illustration of the role of an Imaging fibre bundle. An image (USAF Target) is projected onto the distal end, and the image represented with the core pattern at the proximal end.

By using a fibre bundle it could be possible to surpass the requirement for scanners at the distal end, instead achieving a forward-viewing E-OCT system by capturing an entire field-of-view across the face of the bundle. In this case, each core would contribute a single A-Scan to the OCT image.

Small-form cameras

Small-form cameras are also used in endoscopes and could be seen an alternative route for FV-E-OCT. Such miniature cameras have sensors only a few mm in size and with close to megapixel resolution, such as an OmniVision [33]. However, there are many barriers to their use for FV-E-OCT.

Let us consider performing Swept Source OCT with a small-form camera, i.e. Full-field SS-OCT (FF-SS-OCT). In order to perform FF-SS-OCT, a stack of images at different wavelengths must be captured to process a single OCT volume.

Small-form cameras are not typically capable of real-time high-data output, therefore the images could not be relayed at a sufficient speed for real time imaging. Secondly, these cameras are not typically externally trigger-able and therefore could not be synchronized with a tuned light source, meaning FF-SS-OCT could not be performed.

Finally, these cameras are slow. At a full frame size these are typically limited to less than a 100 fps. At this speed it would take several seconds to capture an OCT volume, causing motion artefacts.

1.5 Fibre Bundle OCT

Let us consider how a FV-E-OCT system utilizing a fibre bundle could be achieved, by reviewing the literature of fibre bundle OCT and characterizing the different approaches and their difficulties.

1.5.1 Single-path

In conventional E-OCT systems, the object fibre from a fibre-coupler is housed within an endoscope, to facilitate illumination of tissue and collection of the backscattered light. The beam is scanned across the sample at the distal end, and the returned light at the proximal end of the fibre superimposed with a reference beam at a detector to perform OCT.

Perhaps the most obvious adaption of E-OCT to a fibre bundle OCT system, would be to lay the bundle into the object path, emulating the configuration in typical E-OCT. This can be referred to as a 'single-path' arrangement of the bundle. In this set up there are two main options to facilitate lateralization and imaging.

In one case, Point-scanning OCT is performed [34]. A beam is focused onto a single core at the proximal end, and scanned across the proximal face to inject light into each core in-turn. At the distal end, the beam emitted from each core in-turn is focused onto the tissue and the backscattered light returned to proximity, returning through the same core. Imaging is achieved across a field-of-view by scanning across all cores.

Alternatively, FF-OCT may be performed [35]. A wide-field beam can be projected onto the proximal face, relaying an extended beam, interrupted into the core arrangement, onto the tissue at the distal end. The backscattered light from an extended area is formed into an image on the distal face. The whole image is relayed to the proximal end and then superimposed with a reference field onto a camera detector to perform Full-field OCT.

Difficulties of single path

There are many effects from the bundle that make a single-path incorporation undesirable and impractical for OCT. The first demonstration of a fibre bundle OCT system implemented a single-path arrangement [1]. Here, a beam was focused onto the proximal end of the bundle and scanned across the face to inject light into each core in turn. This however was only demonstrated with a fused rigid bundle, with poor amenability to endoscopy.

A key finding of this paper, presenting a problem to the single-path design, was the effect of multimoding, the phenomenon by which multiple modes of light are supported through the cores of the bundle. The cores of typical fibre bundles are usually in the range of 2 to 12 μm, meaning multiple modes are supported. These modes travel a different optical path length through the bundle, and as such spurious artefacts are observed in the OCT image, referred to in the literature as ‘ghost artefacts’.

1.5.2 Common-path

An alternative approach was later demonstrated, that employed a 'common-path' arrangement, in which both object and reference fields share a common-path through the same bundle. In this case, object and reference fields are superimposed at the distal end of the bundle, before being transmitted to proximity for detection.

There is a distinction here to be made between the use of the word common-path in this context versus its more conventional meaning in fibre bundle imaging. Typically, in fibre bundle imaging techniques, common-path means that illumination and collection of light both occur though the same fibre bundle. However in the context of fibre bundle OCT, it can instead refer to the superposition of object and reference fields at the distal end of the bundle, meaning that both fields share a common-path through the bundle. Throughout the thesis we will use the word common-path referring to this OCT specific meaning.

The first reported common-path arrangement was used to perform Full-field TD-OCT, free from any lateral scanning at either the proximal or distal end [35]. Here a wound bundle was used, with a more appropriate flexibility for endoscopy than rigid bundles, though still not readily applicable to endoscopy. In this system the proximal face of the bundle was illuminated with a wide-field beam. At the distal end imaging was performed with a 4f telescope. To create a common-path arrangement, reflections from the distal end of the bundle were utilized as the reference wave, enabling for a distal superimposition of object and reference fields. In creating a common-path arrangement, the authors were able to achieve 'down-lead insensitivity', an insensitivity to the effects induced by bending, twisting, or movement of the bundle during operation. However, the system reported a poor SNR of 16 dB, far too low to perform imaging of tissue.

Later, alternative approaches were presented in which a beam splitter was used at the proximal end to create a common-path system [35], [7]. With this design it was possible to achieve a much greater SNR, ranging from 30-40 dB and 30-50 dB respectively in each of the two cited papers. However it is difficult to miniaturize a beam splitter to the sizes amenable to endoscopy. As such any designs incorporating a beam-splitter at the distal end are not ideal solutions to achieving a FV-E-OCT.

1.6 Presented common-path design

Let us briefly introduce the new common-path design at the heart of the thesis. In later chapters the design and the components will be expounded and justified.

We discussed that a common-path arrangement is desirable for fibre bundle OCT, and therefore we must envision a means of generating a superposition of object and reference fields at the distal end of the bundle, that does not require a beam splitter, or rely on weak reflections from the bundle end.

An illustration of the new common-path design at the distal end of a bundle is presented in Fig.1.7(a), along with the proximal components of the complete OCT system in Fig.1.7(b). In all of the cited common-path designs, a 4f telescope was used to produce an image onto the bundle end. In our design we also utilize a 4f telescope, created by two identical lenses, denoted as L1 and L2, which are held together in a casing and separated by a spacer.

In the common-path designs previously cited, illumination was achieved through the fibre bundle, in this sense being common-path both in terms of OCT, but also in the strict sense of performing illumination and collection both through the bundle. However, in our design illumination is achieved from an auxiliary optical fibre, denoted by Obj in Fig.1.7, that runs to the front edge of the telescope, terminating at the edge of L1 and illuminating the sample from off-axis, at angle α. The sample is then imaged onto the bundle face through the 4f telescope.

As shown in Fig.1.7(b), a fibre coupler is used to derive the object fibre, along with a reference fibre, denoted as Ref. The reference fibre is delivered to the edge of L2, projecting light onto the bundle face from off-axis at the same angle α. In this way the reference field comes into superposition with the object image formed at the distal face of the bundle. This in theory secures a superposition of object and reference fields directly at the distal face of the bundle, hence achieving a common-path of object and reference fields.

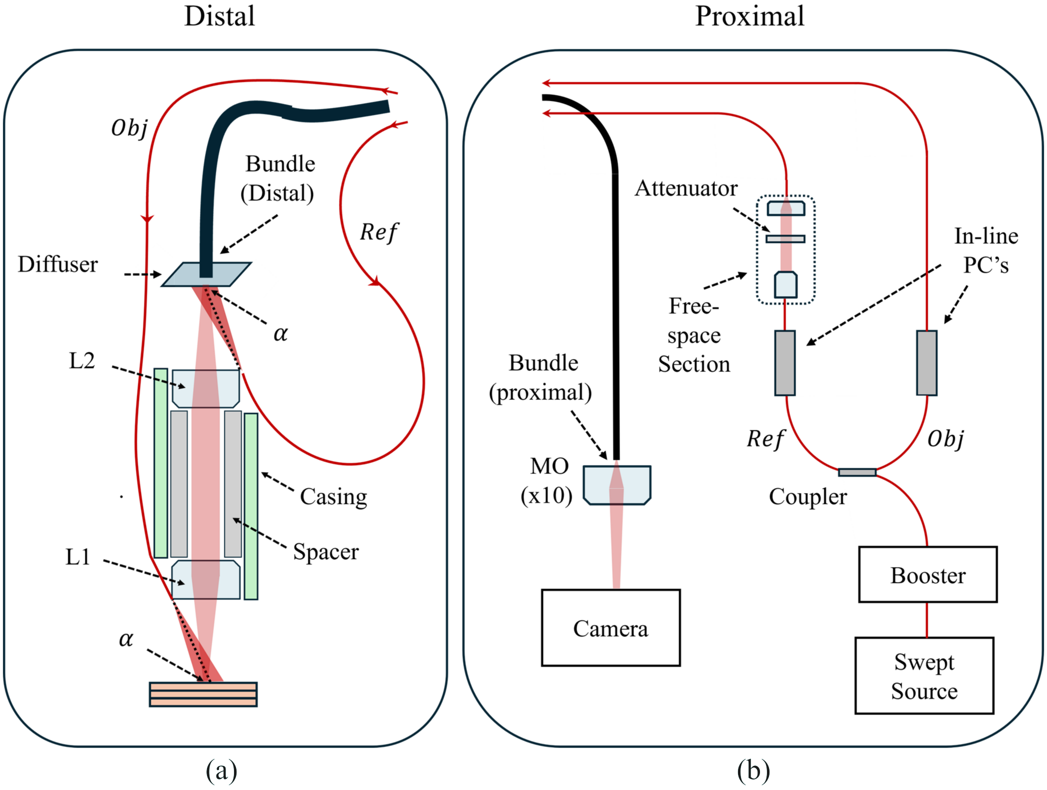

Figure 1.7: Illustration of presented common-path fibre bundle OCT system. (a) Distal components, whereby a superposition of object and reference fields is achieved at the distal face of a bundle, L1 and L2: lenses, α: angle of illumination. (b) Components at proximal end of bundle, MO: Microscope Objective, PC: Polarization Controller.

This design does not require a beam-splitter at the distal end, and has a cylindrical geometry with the potential of being miniaturized and made amenable to endoscopy. Secondly, unlike designs relying on back reflections, the reference power can in theory be adjusted, via attenuators located in a free-space section within the reference arm, potentially helping to achieve a greater SNR.

OCT could be performed in this arrangement by utilizing at the proximal end, a swept source for illumination, and a camera for capturing images relayed through the bundle. In this set up, it should be possible to perform fibre bundle OCT by the established method of Full-field Swept Source OCT [36]. To create the system we must first understand the theory of FF-SS-OCT, which is presented in chapter 2.

The new common-path design requires angled injection of a divergent beam into cores of a fibre bundle, which to the best of my knowledge has not previously been explored. Therefore a first line of experimentation is to validate the possibility of angled injection of fibre bundle cores, which is presented in chapter 3. A diffuser is shown at the distal face of the bundle in Fig.1.7, which was found to be a necessary component, as is presented in Chapter 3.

The design and construction of the system, as shown in Fig.1.7, is presented in Chapter 4. Here, we describe the assembly of an adapter, which facilitates the common-path superposition of object and reference fields in a compact form, well-suited to miniaturization. The inclusion of a booster, a free-space section with an attenuator, and in-line polarization controllers at the proximal end, are all explained and justified. Finally we discuss the potential for a varying OPD across the bundle face, owing to the relative positions of the object and reference beams.

In the final chapter we demonstrate OCT imaging with the adapter, presenting B-Scans and En-face images acquired from a phantom. Two alternative methods of image processing are presented, an FFT approach and a CMS approach, and the performance of each method is quantitatively analysed.

Chapter 2

Full-Field Swept Source OCT

2.1 Introduction

In Chapter 1, we briefly described our proposed full-field fibre bundle OCT system, in which a superposition of extended beams is made at the distal face of the bundle. We therefore intend to perform Full-field OCT, using a camera to capture the relayed superimposed fields at the proximal end of the bundle.

As mentioned in Chapter 1, the main forms of OCT are TD-OCT and FD-OCT. Our motivation is for a simple OCT system, free of mechanical scanning at either end of the bundle, and so we have selected the FD-OCT method. We have also mentioned the general superiority of FD-OCT over TD-OCT, further favouring this decision.

With regards to which type of FD-OCT to perform, we consider that for Sb-OCT, a spectrometer is needed before the detector, to disperse polychromatic light into its frequency components. With a full-field fibre bundle OCT system, this would mean directing the light emitted from each core at the proximal end through a spectrometer, which is not practically feasible.

SS-OCT on the other hand represents a much simpler solution.

With SS-OCT, the frequency components are already resolved in time as they emerge from the proximal end of the bundle over the course of a sweep. We therefore only need to image this emitted light onto a camera, and we can perform OCT. We therefore decide to employ the technique of Full-Field Swept Source OCT (FF-SS-OCT).

Chapter Overview

This chapter is dedicated to explaining the basic theory of FF-SS-OCT. We begin by explaining the fundamentals of OCT, introducing the theory of Michelson interferometry, first with an ideal case of monochromatic light, and then a real-case with broadband light, introducing the concept of coherence.

We give an expression for the detected current at the output of the interferometer, which contains a sinusoidal interference term, representing the position and reflectivity of the layers in depth through a sample. We explain how the A-Scan, resembling the reflectivity profile through the sample, can be produced by taking a Fourier Transform of the detected current

The specifics of SS-OCT are then explained, such as the concept of instantaneous coherence, owing to the instantaneous linewidth of the swept source, which results in a decay curve of interference amplitude with OPD. We present an expression for the detected photocurrent and the resultant A-scan in SS-OCT, discussing features of the A-scan, such as axial resolution, the sensitivity decay curve, and the effects of dispersion onto the A-scan.

We present two alternative methods of processing the A-scan, the conventional Fast Fourier Transform (FFT) approach, and the specialised Complex Master-Slave (CMS) approach.

Finally, we present the Full-field approach to lateralization of swept source A-scans, namely FF-SS-OCT. We discuss the implications of the camera parameters, such as frame speed and bit-depth. We also discuss the effects of spatial coherence, which are unique to FF-OCT and are not typically a problem in scanning based OCT.

2.2 Fundamentals of OCT

2.2.1 Interferometry

Let us imagine a source emitting a monochromatic plane wave, $\boldsymbol{E_S}$, of wavelength λ, travelling in the axial direction, $\hat{z}$, given by:

$$\boldsymbol{E_S} = E_S(k,\omega) \cdot e^{i[kz-\omega t]} \cdot \hat{z} \tag{2.1}$$

Here, $E_S(k,\omega)$, is the electric field amplitude, which is dependent on wavenumber, k, related to wavelength, λ, by $k = \frac{2\pi}{\lambda}$, and angular temporal frequency, ω. The phase of the electric field at time, t, and position, z, is given by $kz - \omega t$. The unit vector $\hat{z}$ indicates that the plane wave is travelling in the axial direction.

We consider an in-bulk Michelson interferometer with a lossless 50/50 beamsplitter, containing a single layer sample in the object path, with reflectivity r_O at axial position z_O, and a mirror in the reference path, with r_R and z_R, as illustrated in Fig. 2.1.

The amplitude, E_S, is equally divided by the beamsplitter, and $\frac{E_S}{\sqrt{2}}$ is delivered to the sample and the reference mirror. The fields of light returned along either arm obtain respective reflectivity factors, r_O and r_R, and phase factors, $2kz_O$ and $2kz_R$, as illustrated in Fig. 2.1. The phase changes represent the round-trip delay along the respective paths of the interferometer. The two electric fields superimposed at the detector, after passing through the beamsplitter, $\boldsymbol{E_O}$ and $\boldsymbol{E_R}$, are given by:

$$\begin{aligned} \boldsymbol{E_O} &= \frac{1}{2}E_S(k,\omega) \cdot r_O \cdot e^{i[2kz_O-\omega t]} \cdot \hat{z} \\ \boldsymbol{E_R} &= \frac{1}{2}E_S(k,\omega) \cdot r_R \cdot e^{i[2kz_R-\omega t]} \cdot \hat{z} \end{aligned} \tag{2.2}$$

and the irradiance of the superimposed beam is calculated by:

$$I = \frac{1}{2}\langle(\boldsymbol{E_O} + \boldsymbol{E_R}) \cdot (\boldsymbol{E_O} + \boldsymbol{E_R})^*\rangle_\tau \tag{2.3}$$

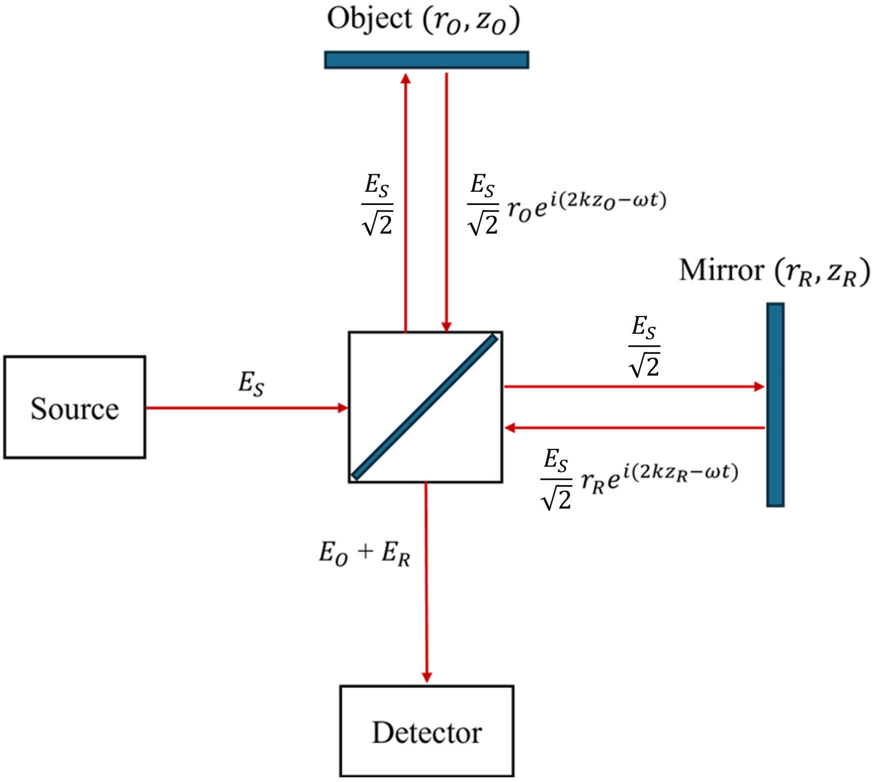

Figure 2.1: Schematic of Michelson Interferometer with a 50/50 beamsplitter and a single layer object.

Where $*$ represents the complex conjugate operation and $\langle\rangle_\tau$ represents averaging over an integration time, τ. In practice, the detected signal is a photocurrent, i_D, dependent on the responsivity of the detector, ρ.

$$i_D = \rho \cdot I \tag{2.4}$$

In the process of square-law detection, integrating the field amplitude over an integration time, τ, the dependency on ω is lost, resulting in a current that varies only with k and z, given by:

$$i_D(k,z) = \frac{\rho}{4} \cdot \langle E_S(k)\rangle_\tau \cdot [{r_O}^2 + {r_R}^2 + 2 \cdot r_O r_R \cdot cos(2k(\Delta z))] \tag{2.5}$$

Here, we have made the substitution $\Delta z = z_O - z_R$, which represents the real distance between the object layer and reference mirror. The expression can be interpreted by considering Fig. 2.1. At a fixed k with fixed Δz, a constant value of current is measured. By adjusting, Δz, the measured current will vary sinusoidally, likewise for fixed Δz with changing k.

Power Representation

We can re-write the expression from optical field amplitude, $E_S(k)$, into optical power, $S(k)$. To do this we introduce the definitions of the power spectrum, $S(k) = \langle E_S(k) \rangle_\tau$, and the power reflectivity, $R = r^2$. We then arrive at the expression for the detected photocurrent in terms of optical power:

$$i_D(k,z) = \frac{\rho}{4} \cdot S(k) \cdot [R_O + R_R + 2 \cdot \sqrt{R_O}\sqrt{R_R} \cdot cos(2k(\Delta z))] \quad (2.6)$$

2.2.2 Coherence

In practice, any real source emits polychromatic light, with a spectrum spanning a finite optical bandwidth, $\Delta\lambda$. The power spectrum of a real source can be approximated by a Gaussian function, centred about the central wavenumber, k_0, with a spectral bandwidth, Δk. In its normalized form it can be expressed as:

$$S(k) = \frac{1}{\Delta k\sqrt{\pi}} \cdot \exp - \left[\frac{k - k_0}{\Delta k}\right]^2 \tag{2.7}$$

With a real light source, the interference fringes are enveloped within a coherence function, $\gamma(\Delta z)$, which by the Wiener Khinchin theorem, is defined as the FT of the power spectrum, given by:

$$\gamma(\Delta z) = e^{-\Delta z^2 \cdot \Delta k^2} \tag{2.8}$$

or in terms of optical wavelength, by:

$$\gamma(z) = \exp\left[-\left(\frac{\pi\,\Delta\lambda \cdot z}{2\ln 2 \cdot \lambda_0^2}\right)^2\right] \tag{2.9}$$

The detected interference fringes are enveloped within the coherence function, such that interference will only occur within the span of the function. At $\Delta z = 0$, a maximum fringe contrast is obtained. For $\Delta z > 0$ the fringes decay, eventually vanishing at the tail of the coherence envelop. The coherence length, l_c, can be defined as the FWHM of the coherence function, giving:

$$l_c = \frac{2\ln 2}{\pi} \cdot \frac{\lambda_0^2}{\Delta\lambda} \tag{2.10}$$

The expression for the detected photocurrent from a single layer sample, when considering a real source with a finite coherence length, is obtained by multiplying the fringes with the coherence function, giving:

$$i_D(k,z) = \frac{\rho}{4} \cdot S(k) \cdot \left[R_O + R_R + 2\sqrt{R_O R_R} \cdot \gamma(\Delta z) \cdot \cos(2k\Delta z)\right] \tag{2.11}$$

2.2.3 Multilayered sample

Let us now consider replacing the single layer object with a multilayered sample, with N reflecting layers. The axial position and optical reflectivity of each layer, in an axial line through the sample, is referred to as a reflectivity profile, $r(z)$. In OCT, this is what is represented in the A-scan. It can be expressed as a sum of Dirac delta functions, $\delta[z - z_n]$, each at a given position z_n, with reflectivity r_n, and is given by:

$$r(z) = \sum_{n=1}^{N} r_n \cdot \delta[z - z_n] \tag{2.12}$$

Detected Photocurrent

Substituting $r(z)$ for r_O in the expression for $\boldsymbol{E_O}$ and re-calculating the detected current we obtain:

$$\begin{aligned} i_D(k,z) = S(k) \cdot \Bigg[R_R &+ \sum_{n=1}^{N} R_n \\ &+ \sum_{n=1}^{N} 2\sqrt{R_n R_R}\,\gamma(\Delta z_n)\cos(2k\Delta z_n) \\ &+ \sum_{n=1}^{N} \sum_{\substack{m=1 \\ m \neq n}}^{N} 2\sqrt{R_n R_m}\,\gamma(\Delta z_n - \Delta z_m) \\ &\cdot \cos\big(2k(\Delta z_n - \Delta z_m)\big) \Bigg] \end{aligned} \tag{2.13}$$

This expression contains three distinct terms. The first term is the D.C. component, it represents a broadband Gaussian spectrum across wavenumber, with amplitude determined by $R_R + \sum_{n=1}^{N} R_n$.

The second term, called the cross-correlation term, is the signal containing the desired reflectivity profile. It is a series of sinusoids, which modulate the D.C component across wavenumber. The amplitude of the n'th modulation is determined by $2\sqrt{R_n R_R}$, while its frequency is given by $2k\Delta z_n$.

The third term is often called the auto-correlation term, and it represents undesired modulations, which result in spurious peaks in the resultant A-Scan. This term is only present in FD-OCT. In TD-OCT, a signal is only returned from the zero OPD. In an ideal OCT system, auto-correlation terms represent self-interference between scattering layers in the object. In real systems, multiple reflections can occur at all optical boundaries in either object or reference arm, such as from lenses, contributing to extra autocorrelation terms.

2.2.4 Fourier Domain OCT

The basic idea of Fourier Domain OCT is to synthesize the detected photocurrent across wavenumber, and then take an inverse Fourier Transform (FT) to produce the A-Scan. This is achieved by sampling the detected current while k is varied. By taking an inverse FT over the synthesised spectrum, modulations across the detected current in the frequency domain are transformed into a real-space representation, producing the A-scan.

2.3 Swept Source OCT

In Swept Source OCT, the detected photocurrent along wavenumber, $i_D(k)$, is synthesized over time using a wavelength tuned source, [37]. Narrowband light is effectively tuned over k and synchronized with a detector to collect a series of readings whose envelope reproduces a broadband spectrum. This effectively samples the expression for the detected current across a tuned bandwidth.

2.3.1 Source Tuning

There are many different types of swept sources, the earliest renditions employing a tunable filter [38] [39]. Here, a linewidth filter, of instantaneous spectral bandwidth, δk, is swept across a broadband source. We can model the instantaneous power spectrum, $S_{\delta k}(k(t))$, as a Gaussian, given by

$$S_{\delta k}(k(t)) = \frac{1}{\delta k\sqrt{\pi}} \cdot \exp\left[-\left(\frac{k(t) - k_0}{\delta k}\right)^2\right] \tag{2.14}$$

or, in terms of wavelength:

$$S_{\delta\lambda}(\lambda) = \frac{1}{\delta\lambda\sqrt{\pi}} \cdot \exp\left[-\left(\frac{\lambda - \lambda_0}{\delta\lambda}\right)^2\right] \tag{2.15}$$

To model sweeping we write an expression for the wavenumber as a function of time, $k(t)$. For an initial wavenumber, k_i, swept over a bandwidth, Δk, in a given sweeping period, ΔT, and assuming linearity, we can express $k(t)$ as:

$$k(t) = k_i + \frac{\Delta k}{\Delta T} \cdot t \tag{2.16}$$

In completing a single sweep, a tuned broadband spectrum, $S_{\Delta k}(k)$ is produced, which is given by:

$$S_{\Delta k}(k) = \frac{1}{\Delta k \sqrt{\pi}} \cdot \exp\left[-\left(\frac{k - k_0}{\Delta k} \right)^2 \right] \tag{2.17}$$

Instantaneous Coherence

In SS-OCT the coherence function enveloping the interference fringes across depth is determined from the instantaneous power spectrum emitted from the swept source, giving an instantaneous coherence function, $\gamma_{\delta k}(\Delta z)$.

$$\gamma_{\delta k}(\Delta z) = e^{-\Delta z^2 \cdot \delta k^2} \tag{2.18}$$

In terms of optical wavelength, this is given by:

$$\gamma_{\delta \lambda}(z) = \exp\left(-z^2 \cdot \left(\frac{2\pi \delta \lambda}{\lambda_0^2} \right)^2 \right) \tag{2.19}$$

Time-varying current

We can now write an expression for the detected photocurrent in SS-OCT as a function of time, by making the substitutions for $k(t)$ and $\gamma_{\delta k}(z)$.

$$i_D(t) = S\big(k(t)\big) \cdot \left[\sum_{n=1}^{N} 2\sqrt{R_n R_R} \cdot \gamma_{\delta k}(\Delta z_n) \cdot \cos\big(2k(t)\Delta z_n\big) \right] \tag{2.20}$$

We have neglected some of the effects of source tuning, which impact the measured current and hence the resultant A-Scan, two main factors to mention are:

Non-linearity

In practice, swept sources do not always tune linearly in optical wavenumber. Instead, tuning is typically linear in wavelength, which results in a non-uniform sampling of $i_D(t)$ [20]. Non-linearity introduces distortions and broadening of peaks in the A-scan, degrading resolution. To correct for this, the signal can be resampled, making it linear in k before applying the inverse FT. This can be achieved using either a calibration interferometer [40] or a k-clock [41].

Phase instability

There may exist phase instability between successive sweeps, for instance due to timing jitter or trigger misalignment. Jitter refers to small, random variations in the timing of the sweep initiation, which can cause fluctuations in the phase of the acquired signal.

The frequencies of phase instabilities induced by jitter and trigger misalignment scale with tuning frequency. For conventional tuning speeds of tens to hundreds of kHz, these typically manifest as MHz phase instabilities [42]. For much slower sweep rates (e.g. sub-Hz), jitter and trigger misalignment may become practically negligible, with phase instability instead becoming dominated by low-frequency drift mechanisms, such as thermal fluctuations of the source or environmentally induced mechanical vibrations.

Jittering and trigger misalignment introduce noise in the reconstructed A-scan, which can be modelled with a random phase term, $\phi_n(t)$, [43] The fringes are then given by

$$\cos\left(2k(t)\Delta z_n\right) \rightarrow \cos\left(2k(t)\Delta z_n + \phi_n(t)\right) \tag{2.21}$$

2.3.2 Channelled Spectrum

The time-varying current, $i_D(t)$, is measured a series of times while the source is tuned, resulting in a detected photocurrent, $i_D(k, z)$. This is commonly called the channelled spectrum. Considering only the D.C. and cross-correlation terms, this is given by:

$$\begin{aligned} i_D(k, z) = S_{\Delta k}(k) \cdot \Bigg[R_R + \sum_{n=1}^{N} R_n \\ + \sum_{n=1}^{N} 2\sqrt{R_n R_R} \cdot \gamma_{\delta k}(\Delta z_n) \cdot \cos(2k\Delta z_n) \Bigg] \end{aligned} \tag{2.22}$$

We see that the fringes are multiplied by the instantaneous coherence function of the swept source.

We can also use an expression that equates the number of oscillations in a given modulation, N, to the OPD of that layer over the coherence length, given by,

$$N = \frac{OPD}{l_c} \tag{2.23}$$

2.3.3 Inverse Fourier Transform

Once the channelled spectrum is obtained, an inverse FT is taken to produce the A-scan. The inverse FT of a sinusoid is a pair of Dirac delta functions, $\delta[z + z_n] + \delta[z - z_n]$. Therefore, the FT of the channelled spectrum produces a series of Dirac delta functions, which represent the reflectivity profile of the sample.

We recall the Wiener–Khinchin theorem, and hence the inverse FT of the broadband power spectrum, $S_{\Delta k}(k)$, is a broadband coherence function, $\gamma_{\Delta}(z)$. We also utilize the convolution property of the FT, which states that products in the frequency space have their inverse FT elements convolved in the spatial domain. This means that in the A-scan, the reflectivity profile is convolved with the broadband coherence function. Considering only the cross-correlation term, this gives us:

$$A_{cross}(z) = \gamma_{\Delta k}(z) \otimes \Big(\sum_{n=1}^{N} \cdot 2\sqrt{R_n R_R} \cdot \gamma_{\delta k}(z) \cdot \Big(\delta[z+z_n] + \delta[z-z_n] \Big) \Big) \tag{2.24}$$

Here $\otimes$ represents the convolution operation, $\gamma_{\Delta k}(z)$ is the tuned coherence function, and $\gamma_{\delta k}(z)$ is the instantaneous coherence function. Performing the convolution operation, and ignoring the negative Dirac delta component, gives us the expression for the real-space representation of the cross-correlation term:

$$A_{cross} = \sum_{n=1}^{N} \cdot 2\sqrt{R_n R_R} \cdot \gamma_{\delta k}(z) \cdot \Big(\gamma_{\Delta k}[z - z_n] \Big) \tag{2.25}$$

2.3.4 Full A-Scan Expression and Parameters

The full expression for the A-scan in FD-OCT, obtained by taking the inverse FT over all components of the detected photocurrent, when ignoring negative conjugates, is given by:

$$\begin{aligned} A(z) = &\gamma_{\delta k}(z) \cdot \left(R_R + \sum_{n=1}^{N} R_n \right) \\ &+ \sum_{n=1}^{N} \sqrt{R_n R_R} \cdot \gamma_{\Delta k}(z - \Delta z_n) \\ &+ \sum_{n=1}^{N} \sum_{\substack{m=1 \\ m \neq n}}^{N} \sqrt{R_n R_m} \cdot \gamma_{\Delta k}(z - (\Delta z_n - \Delta z_m)) \end{aligned} \tag{2.26}$$

The A-scan contains three components. At position $z = 0$ we have a large amplitude peak, representing the combined power returned from the object and sample. At positions Δz_n we observe the desired cross-correlation peaks, representing the reflectivity profile. At positions $\Delta z_n - \Delta z_m$, we observe autocorrelation peaks.

Axial Resolution

It is clear that each layer in the reflectivity profile is now resembled in the A-scan by the tuned coherence function. The axial resolution is hence determined by the tuned coherence length, which is typically measured as the FWHM of the tuned spectrum. Unlike in TD-OCT and Sb-OCT, where a broadband source is used with an approximately Gaussian spectrum, in SS-OCT the tuned spectrum more closely resembles a top-hat function. In TD-OCT and Sb-OCT, with a close to Gaussian resembling spectrum, the typically cited resolution is $\gamma_{\Delta k}(z)_{FWHM} = \frac{2ln(2)}{\pi} \cdot \frac{{\lambda_0}^2}{\Delta\lambda}$.

However, in SS-OCT, with closer to a top-hat resembling spectrum, a different co-efficient applies, which has been demonstrated, [44], and is widely cited in the literature. They demonstrated, that for SS-OCT, a more realistic co-efficient is approximately 0.6. We use this definition for axial resolution in SS-OCT, giving:

$$\delta_z \approx 0.6 \cdot \frac{{\lambda_0}^2}{\Delta\lambda} \tag{2.27}$$

Signal-to-Noise Ratio

The signal-to-noise ratio (SNR) is used to characterise signal strength relative to background noise. SNR is defined in term of amplitude by:

$$\text{SNR} = 20\log_{10}\left(\frac{A_{\text{signal}}}{A_{\text{noise}}}\right) \tag{2.28}$$

or alternatively in terms of power, by :

$$\mathrm{SNR} = 10\log_{10}\left(\frac{P_{\mathrm{signal}}}{P_{\mathrm{noise}}}\right) \tag{2.29}$$

Let us consider our expression for monochromatic interference. The amplitude of the signal is given by, $A_{Signal} \propto \sqrt{P_O P_R}$, giving $P_{signal} = A^2_{signal} = P_O P_R$. The noise in terms of power, is given by $P_{Noise} = P_O + P_R$. Our SNR is then given by:

$$\mathrm{SNR} \propto \frac{P_O P_R}{P_O + P_R} \tag{2.30}$$

From this expression, the SNR is maximised when $P_R = P_O$, meaning that to acquire the best SNR, we control the reference power, such that is matches the power in the object beam. In SS-OCT, the SNR can be approximated by:

$$\mathrm{SNR} = 10\log_{10}\left(\frac{R_s P_s^2}{N_0 B}\right) \tag{2.31}$$

where R_s is the sample reflectivity, P_s is the optical power incident on the sample, N_0 is the noise power spectral density (e.g., thermal or shot noise), and B is the detection bandwidth.

Sensitivity

The system sensitivity, S, is defined as the minimum detectable reflectivity, R_{min}, when SNR = 1 (0 dB), and is given by:

$$S = 10\log_{10}\left(\frac{1}{R_{\mathrm{min}}}\right) \tag{2.32}$$

In typical SS-OCT systems, sensitivity values of -100 dB or better can be achieved near to zero OPD, but this sensitivity decreases with depth due to the coherence roll-off.

Sensitivity Roll-off

The instantaneous coherence function enveloping the A-scan determines a fundamental signal roll-off along depth, commonly referred to as the sensitivity roll-off. We recall that the instantaneous coherence function is symmetric about zero OPD. Hence, assuming that the sample is placed at zero OPD, only one half of the decay curve extends through the sample. Therefore, to characterise sensitivity, the FWHM of the instantaneous coherence function is measured, and then halved, giving:

$$l_{c,\delta k} = \frac{\ln 2}{\pi} \cdot \frac{\lambda_0^2}{\delta\lambda} \tag{2.33}$$

Alternatively, roll-off can be expressed with the -3dB drop off range, which is defined as the distance at which the signal has dropped by 3dB.

2.3.5 Dispersion

Phase velocity dispersion (PVD) and group velocity dispersion (GVD) both occur in SS-OCT, having different effects on the channelled spectrum and hence the A-Scan. Considering that interference fringes are measured over a broadband spectrum, GVD has the effect of a non-linear phase increase with OPD and wavenumber, i.e. $\phi \neq k \cdot OPD$. The effect of PVD is not typically an issue for OCT, as its only effect is a global shift of OPD, therefore not affecting the image.

If dispersion between the two arms of the interferometer is unmatched, either caused by the sample, or from different materials in either arm, the resulting channelled spectrum is 'chirped'. In this case, fringes are no longer evenly spaced across wavenumber, which degrades resolution in the resultant A-scan after taking an FT.

Let us consider a case where the sample and reference arms experience different GVD's. The phase difference between the two arms is given by

$$\Delta\phi(k) = 2k\Delta z + \Delta\phi_{disp}(k) \tag{2.34}$$

where $\Delta\phi_{disp}(k) = \phi_{disp,O}(k) - \phi_{disp,R}(k)$, i.e. the difference in dispersion between the object and reference fields. If $\Delta\phi_{disp}(k)$ is non-linear in k, i.e. there exists higher order dispersion, of GVD's and above, then this has the effect of distorting the channelled spectrum, smearing out the sinusoidal fringes and thereby broadening the peaks in the A-scan.

Dispersion Compensation

One approach of compensation is to introduce lengths of glass into the reference arm of the interferometer, thereby physically matching dispersion between arms of the interferometer.

Another approach is by numerical correction in post-processing, whereby a corrective phase term is applied to the channelled spectrum before taking the inverse FT. This is often done by multiplying the spectrum by a phase correction factor, $e^{-i\cdot\Delta\phi_{disp}(k)}$.

$$i_D^{corr}(k) = i_D(k) \cdot e^{-i\cdot\Delta\phi_{disp}(k)} \tag{2.35}$$

The function $\Delta\phi_{disp}(k)$ is obtained before imaging. One approach is to obtain calibration measurements, in which the spectra is measured at intervals of OPD to measure the changes in phase. The function can then be interpolated from the measured values.

2.4 Detection and Processing

In practice, the time varying photocurrent is captured at M points, generating a discrete array, $i_{D,M}$, i.e.

$$i_D(t) \rightarrow i_{D,M} = \sum_{m=1}^{M} i_{D,m} \tag{2.36}$$

Considering only the cross-correlation term, the expression for the current at each detection is given by:

$$i_{D,m} = S_{\delta k}(k_m) \cdot \left[\sum_{n=1}^{N} 2\sqrt{R_n R_R} \cdot \gamma_{\delta k}(z) \cdot \cos\left(2k_m \Delta z_n\right) \right] \tag{2.37}$$

where, $m = 1, 2, \ldots, M$, represents each sampling point, and k_m is the wavenumber at the m'th sampling point. The resultant channelled spectrum is the summation of all sampled currents:

$$i_D = \sum_{m=1}^{M} S_{\delta k}(k_m) \cdot \left[\sum_{n=1}^{N} 2\sqrt{R_n R_R} \cdot \gamma_{\delta k}(z) \cdot \cos\left(2k_m \Delta z_n\right) \right] \tag{2.38}$$

Detection bandwidth

The detected interferometric signal is convolved with the impulse response of the detector, denoted by $h_{\mathrm{det}}(t)$, which is mainly determined by the detector bandwidth and the photodiode response time. The convolution acts as a low-pass filter, and as such high-frequency components of the signal may be attenuated or distorted, limiting the axial resolution and introducing temporal smoothing into the A-scan. The measured signal can be written as:

$$i_{D,measured}(t) = i_D(t) * h_{\mathrm{det}}(t) \tag{2.39}$$

Sampling

An appropriate number of samples, M, must be taken to ensure the sensitivity curve is not shortened by undersampling. We recall that the decay curve is determined by the spectral bandwidth. Hence, if the sampling window is broader than the spectral bandwidth, the maximum permissible decay length will not be achieved, and instead the roll-off length will be reduced, compromising on SNR in depth.

Axial Range

More crucially, the number of sample points determines the axial range, i.e. the maximum depth within the sample that can be reconstructed in the OCT image.

Considering that OPD is encoded into the frequency of fringe modulations, the frequency of detection must be great enough to sample the modulations. As such, there reaches a depth at which the modulations can no longer be resolved, introducing a fundamental depth limit. This is commonly referred to as the axial range, z_{max}. If the spectrum is sampled at M points, the axial range is given by:

$$z_{max} = \frac{1}{4}\frac{\lambda_0^2}{\Delta\lambda} \cdot M \tag{2.40}$$

Aliasing

Aliasing in SS-OCT refers to when structures deeper than the axial range are folded back into the image at incorrect positions, causing artefacts. This can occur when the spectrum is undersampled, i.e. if M is too low.

2.4.1 Discrete Fourier Transform

A Discrete Fourier Transform (DFT) is applied to the discrete array of detected currents to reconstruct the A-scan. The result is a complex-valued array $\tilde{i_D}(z_n)$, where the index n corresponds to discrete depth positions z_n. This operation is typically implemented using the Fast Fourier Transform (FFT) algorithm. The DFT of $i_{D,m}$ is defined as:

$$\tilde{i_D}(z_n) = \sum_{m=0}^{M-1} i_{D,m} \cdot e^{-i2\pi nm/M} \tag{2.41}$$

The index, m represents the wavenumber sample point, while n indexes the spatial frequencies in the depth domain after transformation. The A-scan is retrieved by taking the absolute value of the complex-valued DFT result:

$$A_{\text{cross}}(z_n) = \left|\tilde{i_D}(z_n)\right| \tag{2.42}$$

The physical depth values corresponding to the DFT indices are given by:

$$z_n = \frac{n}{2\Delta k}, \quad n = 0, 1, \ldots, M-1 \tag{2.43}$$

where Δk is the uniform spacing between adjacent wavenumber samples after resampling. The factor of 2 accounts for the round-trip travel of light in the OCT interferometer.

Windowing

The expression $i_{D,m}$ is of finite length, meaning direct application of the DFT can introduce spectral leakage, due to implicit discontinuities at the signal boundaries. These effects can be mitigated by applying a windowing function prior to the DFT. A window function, w_m, smoothly tapers the signal toward zero at the edges. Commonly used window functions include the Hanning and Hamming. For example, the Hanning window is defined as:

$$w_m = 0.5\left(1 - \cos\left(\frac{2\pi(m-1)}{M-1}\right)\right) \tag{2.44}$$

Zero-padding

After windowing and before taking the DFT, zero-padding may also be applied, by adding extra zeros to the end of the windowed signal. This increases the number of points in the DFT, leading to a finer sampling in the reconstructed A-scan. It does not affect resolution, but can improve localization of peaks as well producing a cleaner appearance of A-scan peaks. Zero-padding also improves the interpolation used for linearisation of k.

2.4.2 Complex Master–Slave

The Complex Master–Slave (CMS) method [45] is an alternative approach of processing the channelled spectrum into an A-scan. It is based on the originally conceived Master–Slave (MS) method [46], [47], used in Time-Domain OCT, and later developed into the CMS method for FD-OCT processing. Unlike the FT method, CMS does not require a uniform sampling of wavenumber, and instead enables channelled spectrum obtained with non-linear tuning and system dispersion to be processed into an A-scan without suffering a degraded resolution. CMS has also been combined with advanced imaging techniques such as Gabor Fusion, achieving a constant transverse resolution over an extended depth range [48].

The A-scan is reconstructed by a matrix multiplication of the channelled spectrum, referred to as the "slave", with an array of pre-calibrated interference spectra, referred to as the "masks". The set of masks are obtained, prior to imaging, from a mirror in the object arm, which is positioned at equally spaced intervals of OPD. The spectra at each position is collected forming a single mask. A calibration function is then extrapolated from the acquired masks, capturing the non-linear phase changes across k. In principle, only two experimentally obtained spectra are required to define a set of masks, although more densely spaced calibration points can improve the resultant A-scan [49].

Theory

Each experimentally obtained mask corresponds to a complex exponential, representing the interference spectra of a layer at depth z_n. Each experimentally derived mask is given by:

$$\psi_n(k_m) = e^{i2k_m z_n}, \quad m = 0, 1, \ldots, M-1 \tag{2.45}$$

The real and imaginary components are then extracted, which together form a complex exponential. This can be achieved with a Hilbert Transform. The real part captures non-uniformity of the fringe frequency due to non-linear tuning and system dispersion:

$$g_n(k_m) \approx \Re\left[e^{i\,\phi_n(k_m)}\right] \tag{2.46}$$

Similarly, for the imaginary part, we have:

$$h_n(k_m) \approx \Im\left[e^{i\,\phi_n(k_m)}\right] \tag{2.47}$$

The obtained values are then extrapolated to construct the 'g' and 'h' functions, $g(k)$ and $h(k)$, which span over all k. Together, $g(k)$ and $h(k)$ form a complex-valued basis function,

$$\psi(k) = g(k) + i\,h_n(k) \tag{2.48}$$

Written explicitly in terms of the phase across k, $\phi(k)$, as:

$$\psi(k) = e^{i\,\phi_n(k)} = e^{i(2kz+\delta\phi(k))} \tag{2.49}$$

A-scan Reconstruction

Let $\mathbf{i}_D$ be a vector representing the channelled spectrum, i.e. the slave spectra, and let $\boldsymbol{\Psi}$ be the matrix of complex masks, where each column $\psi_n(k_m)$ corresponds to a depth point, z_n. The full complex A-scan is then computed via a matrix multiplication:

$$\mathbf{A}(z)_{\text{CMS}} = \boldsymbol{\Psi}^\dagger \cdot \mathbf{i}_D \tag{2.50}$$

Here, $\boldsymbol{\Psi}^\dagger$ is the conjugate transpose (Hermitian) of the mask matrix, and $\mathbf{A}_{\text{CMS}}$ contains the complex-valued signal at each depth z_n.

The final reflectivity profile is obtained by taking the magnitude of each complex element:

$$A_{\text{cross}}(z_n) = \left|\mathbf{A}(z)_{\text{CMS}}\right|, \quad \text{for } n = 0, 1, \ldots, N-1 \tag{2.51}$$

This operation yields the full A-scan, with each element corresponding to the reflectivity from a particular layer in depth.

2.4.3 Pros and Cons of CMS

The CMS approach offers several advantages over the traditional FFT with re-linearization method, [50].

En-face frame selection

Perhaps the main advantage of the CMS approach is that it allows for the reconstruction of single en-face frames independently. This means that a desired subset of depth layers can be reconstructed, enabling for fast extraction of a desired region. This is in contrast to the FFT approach, in which all depths must be reconstructed at once, without any way of reducing the reconstructed region to improve speed.

No zero-padding or windowing

Unlike FFT-based methods, CMS does not require zero-padding or windowing. Each depth point is reconstructed independently, which allows for better isolation of reflectors and reduced side-lobe artifacts. This can result in improved axial resolution and noise performance when implemented with well-calibrated masks.

Computational load

A disadvantage of CMS is that it is more computationally intensive than FFT-based methods, especially when reconstructing many depth points. However, since the process is parallelizable and memory-efficient, it is well-suited to modern GPU-based implementations [49].

2.5 Full-field SS-OCT

OCT systems typically employ a Point-scanning approach, in which scanners are used to scan a focused beam across the sample to acquire B-scans and volumes. Full-field OCT by-passes the requirement for scanners, by employing extended beams, and acquiring A-scans over an extended region simultaneously. With FF-SS-OCT, we can still implement the CMS method, as has been demonstrated [51].

We now consider a basic set-up of Full-field SS-OCT, using a Michelson interferometer, illustrated in Fig. 2.2. Extended beams of light from a Swept Source (SS) are projected onto the Object (O) and Reference Mirror (RM). The backscattered beams are superimposed over an extended area on the sensor of a camera, e.g a camera with a CMOS sensor.

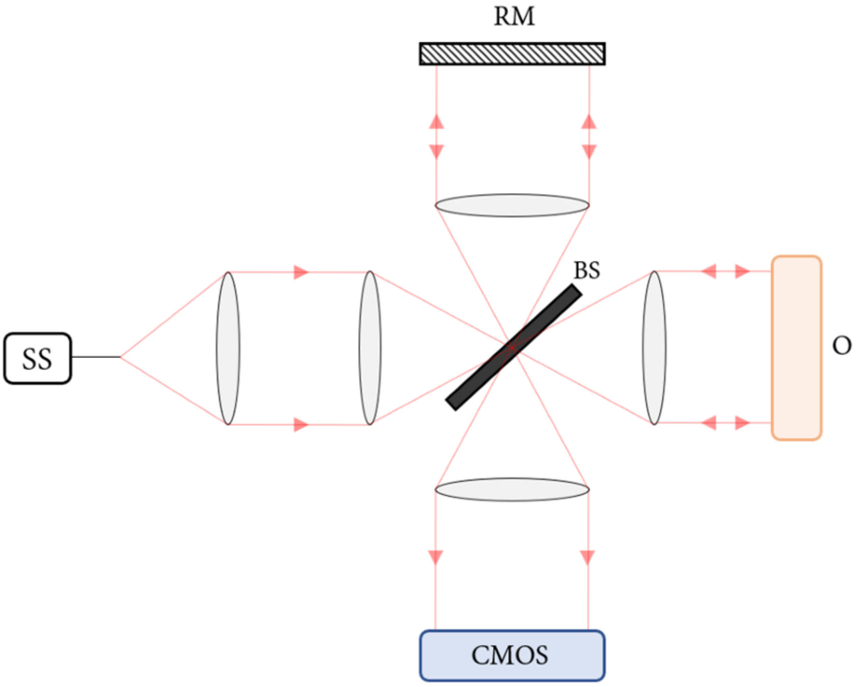

Figure 2.2: Schematic of a FF-SS-OCT System, in a Michelson interferometer set-up.

2.5.1 Acquisition

The M spectral points described earlier are now detected as M spectral frames. The number of pixels across the sensor determines the lateral size of the resultant OCT volume, in terms of the number of points along the x and y directions. To perform acquisition, the camera is triggered to capture a burst of images in synchrony with each tuning cycle of the source, such that a series of detected frames span across the tuned spectrum.

Once the spectral frames are collected, an inverse FT is applied at every pixel along the spectral direction, returning an array of A-scans which represent the OCT volume. Slices can then be viewed in the B-scan or en-face orientation. Considering the conjugate term of the inverse FT, the resulting number of points in the A-scan is $\frac{M}{2}$, and hence also the number of en-face slices and the number of points in depth along the B-scan.

2.5.2 Speed vs SNR

For a given sweeping period, ΔT, and a required number of spectral frames, M, the selected speed of the camera, in terms of frames per second (fps), is given by:

$$fps = \frac{M}{\Delta T} \tag{2.52}$$

Let us consider exposure time, with respect to camera speed, considering that SNR is proportional to exposure time. In practice, there is a readout time between each successive exposure, and hence the exposure time, τ, is slightly less than the inverse of the fps, given by:

$$\tau \leq \frac{1}{fps} \tag{2.53}$$

There is hence a balancing act between speed and SNR. The overall speed is determined by the swept source frequency, $f_{source} =$

$\frac{1}{\Delta T}$. In an ideal scenario we would sweep as fast as possible, allowing for greater object coverage within a given time, and perhaps more crucially, less motion artefacts. However, by sweeping faster, we necessarily drop the exposure time, and hence reduce SNR.

Motion Artefacts

FF-OCT is more sensitive to motion artefacts than Point-scanning OCT. Slight sample movements during the acquisition of a spectral frame can cause artefacts in the reconstructed volume. This is particularly problematic for *in-vivo* imaging. High sweep rates and short camera integration times can be employed to mitigate motion artefacts, however this must be met with the trade off of reduced SNR.

2.5.3 Lateral Resolution

The lateral resolution, Δxy, is determined by the pixel pitch of the sensor, p_{sens}, along with any magnification of the object beam onto the sensor, M, such as from the camera's objective. The expression for the lateral resolution is then given by:

$$\Delta xy = \frac{p_{sens}}{M} \tag{2.54}$$

Lateral Point Spread Function

While lateral resolution is estimated from the pixel pitch and system magnification, a fundamental diffraction limit also applies. For a system using an objective with numerical aperture (NA) and central wavelength λ_0, the diffraction-limited lateral resolution is given approximately by:

$$\Delta x \approx \frac{1.22 \cdot \lambda_0}{2\,\mathrm{NA}} \tag{2.55}$$

This defines the minimum resolvable spot size in the lateral plane. To capture this spatial resolution at the camera, we require adequate pixel sampling, such that the breadth of the focused spot is spanned by multiple camera pixels. Without correct sampling, the resolution will be limited to the camera pitch, with any smaller spatial frequencies not resolved and potentially aliased. By the Nyquist sampling criterion, a minimum of two camera pixels are required, although in practice more than two pixels may be needed to prevent undersampling. This is achieved by choosing a camera with an appropriate camera pitch, along with selecting an appropriate magnification onto the sensor.

2.5.4 Spatial Coherence and Cross-talk

The source used in SS-OCT is typically highly spatially coherent, meaning interference can be supported along an extended lateral region. Considering FF-OCT utilizes wide-field beams onto an extended sensor, interference can occur between adjacent pixels of the sensor, referred to as cross-talk. The channelled spectrum at the effected pixels are altered, resulting in degradation to the resultant A-scan peaks.

There are several established methods of mitigating the effects of spatial coherence. One approach is to use an LED with a short spatial coherence length [52]. Other methods have managed to continue using narrowband light, as in SS-OCT, either by using a rotating diffuser [53], or a multimode fibre [54].

2.5.5 Dynamic Range

The dynamic range of the camera sensor plays a crucial role in the permissible SNR. A higher bit-depth (e.g., 12–16 bits) enables for a greater potential of SNR and hence sensitivity.

The attainable dynamic range, $DynR$, in FF-OCT using a camera with a given bit-depth, is in theory given by:

$$DynR = 20log_{10}(2^{bit-depth}) \tag{2.56}$$

For instance, with a 10-bit camera, the maximum permissible dynamic range is; $20log_{10}(2^{10}) = 60dB$, while for a 12-bit this increases to 72 dB and with 16-bit reaches a dynamic range of 96 dB. However, in practice a real camera suffers from inherent noise, such as the dark current and the read noise, and a more realistic attainable SNR from a 10-bit would be up to 50–55 dB.

Camera Bandwidth

The readout speed and bandwidth of the camera must also be matched to the sweep rate of the source to avoid frame loss and maintain fidelity across the spectral sweep.

2.6 Conclusion

In this chapter, we have described the principal aspects of the theory of FF-SS-OCT. We derived an expression for the A-scan in SS-OCT and discussed its features, such as axial resolution, SNR, decay-curve and axial range. We discussed the implications of higher order dispersion and presented the CMS method as an attractive method of dispersion compensation. We established that the CMS approach also offers several other advantages over the conventional FFT approach.

We briefly discussed the theory of FF-OCT, in particular FF-SS-OCT. We discussed the inherent trade-off of speed and SNR, and discussed the attainable dynamic range of A-scans owing to the bit-depth of the camera.

Chapter 3

Angled Divergent Beam Injection of Fibre Bundle Cores using a Diffuser

3.1 Introduction

Reported cases of fibre bundle OCT have typically employed on-axis injection of light into cores, either with a point-scanned beam, e.g. [55], or with full-field illumination, e.g. [56]. With on-axis injection, the vast majority of coupled power is distributed into the first order mode, meaning there is minimal modal dispersion through the bundle, and the OCT signal can be moderately well-preserved. However, in our proposed common-path design, we require angled illumination of cores, with our divergent reference beam, and this presents several challenges for OCT. Most crucially, large angles excite higher-order modes, inducing greater modal dispersion, which results in a severe degradation of the OCT signal.

Angled illumination also means less efficient coupling of power. Fibre bundle cores exhibit an angular acceptance curve, with power coupled dropping off significantly for larger angles of incidence. The acceptance curve is determined from the core NA, and the cut off angle, θ_c, at which intensity has dropped to $\frac{1}{e^2}(\approx 0.135)$, can be approximated by;

$$\theta_c = sin^{-1}(NA) \tag{3.1}$$

The core NA of typical fibre bundles ranges from 0.2 to 0.5, though in some cases reaches up to 0.66 [57]. For a bundle with a high core NA, of say $NA = 0.5$, the cut off angle would be $\theta_c = 30°$, and this imposes a fundamental limit to the angle of illumination.

With angled injection we also increase the proportion of power coupled into the inter-core spacing, which has the effect of reducing the intensity within cores and contributing more noise across the transmitted image. Increasing the angle of incidence also increases cross-talk between cores, having the effect of a lateral dispersion of the OCT signal, degrading resolution and image clarity.

Before building our fibre bundle OCT system, (which is presented in Chapter 4), we must first characterize the effects of angled divergent illumination of cores. We must establish that an efficient coupling of low order modes can be achieved, else it would be practically impossible to perform OCT, and there would be no motivation to continue with our proposed common-path design.

3.1.1 Chapter Overview

This chapter presents experimentation with a Schott leached fibre bundle. We demonstrate greater higher order modal coupling at larger angles of incidence, quantifying coupling efficiency and qualitatively assessing modal behaviour. Our experimentation confirms the unsuitability of coupling under the demanded conditions of illumination.

We then present a discovered solution, to place a thin diffuser flush at the bundle face. This has the effect of scattering the incident beam, such that a portion of the incident light exits the diffuser at close to on-axis. This successfully achieves a majority of coupling into lower-order modes. It also achieves an increase of the total power coupled, and reduces the proportion of power within the inter-core spacing.

3.2 Schott Leached Fibre bundle

The bundle selected for experimentation is a Schott leached fibre bundle (Schott #1549304), with manufacture quoted parameters:

Metric	**Value**
Diameter, D	1.05 mm
Resolution, K	18,000
Core NA	0.5, [7]
Length	0.76 m

Table 3.1: Parameters of Schott Leached Fibre Bundle #1549304

Other crucial parameters, such as core pitch, p, and core diameter, d, are not specified by the manufacturer, and must be measured experimentally.

3.3 Imaging the Bundle

Our first step is to image the proximal end of the bundle onto a camera. Considering our experimentation is conducted towards building a fibre bundle OCT system, it makes sense to conduct our experiments with a camera suitable for FF-SS-OCT.

For this we require a camera capable of capturing several hundreds of fps, that is externally trigger-able for synchronizing with source tuning, and with a fast high-data output for real-time acquisition. Cameras meeting these specifications are conventionally called 'Machine Vision' cameras. We have selected a Mikrotron EoSens MC1360-63. The key parameters are quoted below.

Metric	**Value**
Full Sensor Size	1280 x 1024 (pixels)
Sensor Dimensions	19.92 (h) x 14.34 (w)(mm)
Pixel Size	14 x 14 (μm)
Pixel Pitch	14 (μm)
Absolute speed	1.3 $Megapixels/s$
Bit Depth	10-bit

Table 3.2: Mikrotron EoSens MC1360-63 camera parameters.

3.3.1 Proximal Magnification

To image the proximal end of the bundle onto our camera we can use a microscope objective (MO). To find an appropriate magnification, M, we calculate the ratio of bundle diameter, D to sensor width, w

$$M = \frac{w}{D} = \frac{14.34}{1.05} = 14.34 \tag{3.2}$$

The closest standard MO we can use is a x10 magnification. The set-up for imaging at the proximal end is given in Fig. 3.1. The proximal end of the bundle is fixed into a brass chuck, which is then locked into a tip/tilt/XYZ translation stage. The MO is placed at the working distance from the bundle face, and the camera sensor positioned at the tube length distance from the MO.

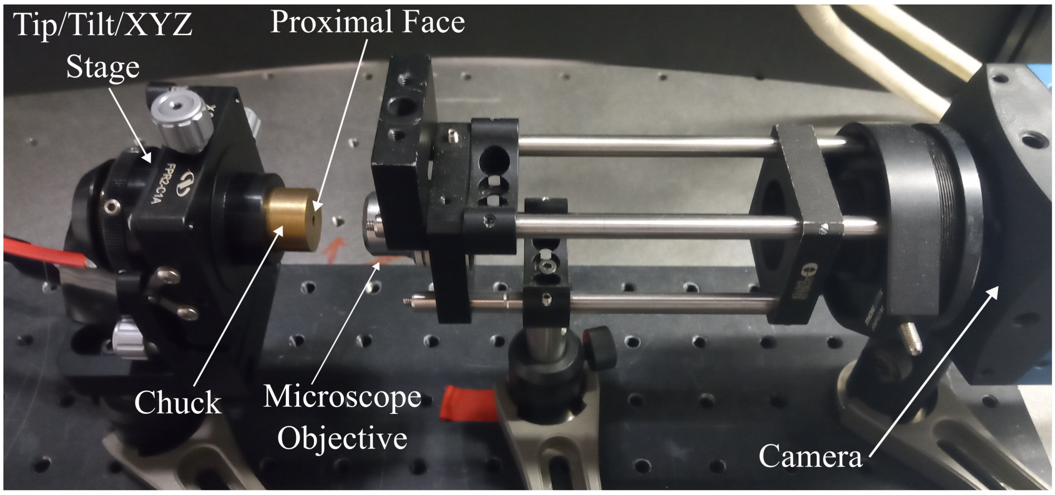

Figure 3.1: Photograph of set-up for imaging proximal end of bundle onto a camera.

Sensor Size and Speed

Given a x10 magnification, with a bundle diameter of 1.05 mm, and 14 μm pixel size, the expected sensor size covered by the bundle, in terms of number of pixels, is given by the calculation

$$X, Y = \frac{1.05\, mm \cdot 10}{14\, \mu m} = 750\ (pixels). \tag{3.3}$$

We select an image size of $\mathbf{X,Y} = \mathbf{[800,800]}$, ensuring we adequately image the entire bundle. At this frame size, the maximum camera speed is **418 fps**.

3.3.2 Distal Illumination

Let us now illuminate the distal end with narrowband light from a swept source. We use a Superlum BroadSweeper-840 BS0002, centred at 840 nm. The key metrics presented are taken from the user manual, and are given in Tab. 3.3.2

Metric	**Value**
Power, P_0	5 (mW)
Central wavelength, λ_0	849.5 (nm)
Bandwidth, $\Delta\lambda$	47 (nm)
Linewidth, $\delta\lambda$	0.04 (nm)

Table 3.3: Superlum BroadSweeper-840 BS0002 parameters.

The set-up for illuminating the distal end of the bundle is given in Fig. 3.2. The bundle end is held in a custom 3D-printed mount, and fixed into place with two screws.

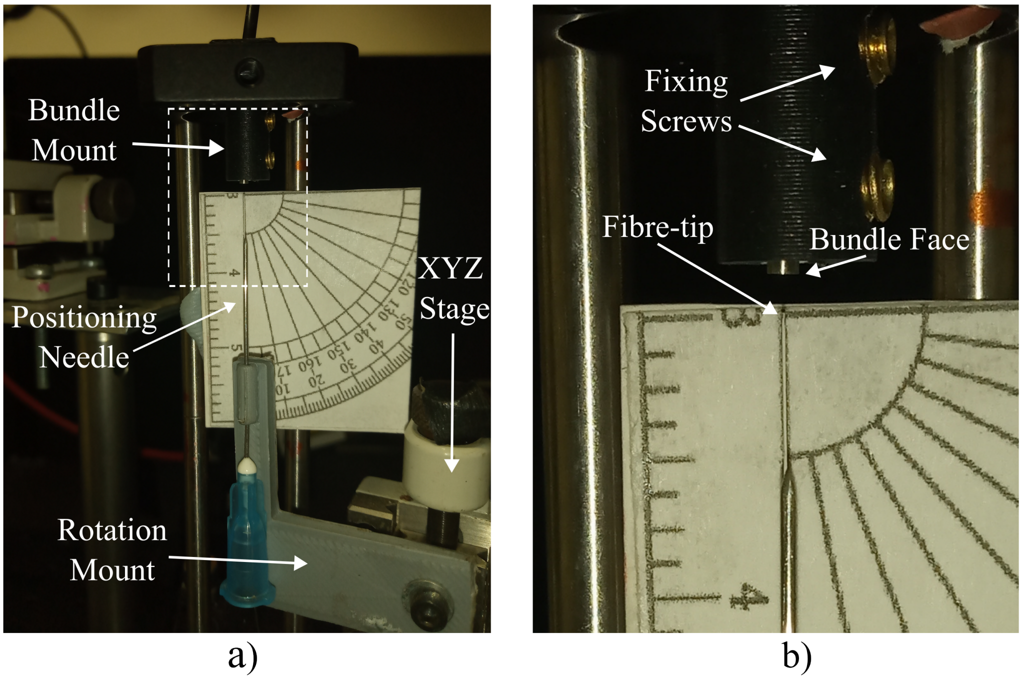

Figure 3.2: Distal illumination set-up; a) Components for fixing bundle and positioning fibre. b) Zoomed in photograph showing bundle face, fibre-tip and fixing screws.

Typically, chucks are used to fix optical fibres, which are then positioned in Tip/Tilt/XYZ stages for fine position adjustment. However these are bulky, and it was difficult to use a chuck in conjunction with an illuminating fibre. Therefore a custom fibre bundle mount was created, and positioned into a cage system. XY translation and tip/tilt were not necessary, as the bundle was positioned directly in the centre of the cage, while Z translation is given by sliding the mount up and down the cage.

To control the positioning of the illuminating fibre, the fibre is threaded through a hypodermic needle. This holds the fibre in place whilst also allowing axial translation by pulling/pushing the fibre. The needle is then inserted into a custom-made rotation mount, allowing us to vary the angle of incidence onto the bundle. The rotation mount is then fixed to an XYZ stage for fine positioning of the fibre-tip.

3.3.3 Fibre bundle Measurements

Let us first consider normal incidence, as shown in Fig. 3.2, and capture an image of the bundle face. We can use this image to measure the proximal magnification, ensuring we are correctly imaging at the proximal end. An image obtained is shown in Fig. 3.3.

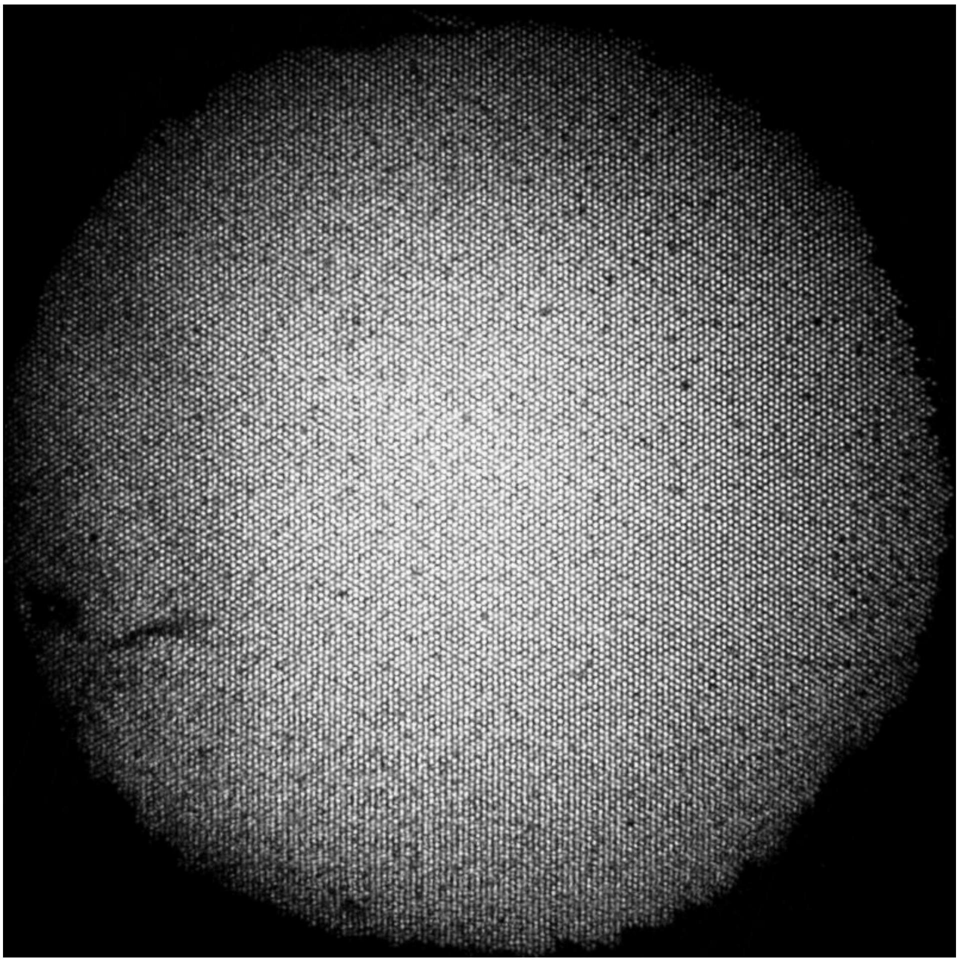

Figure 3.3: Image of proximal end of bundle, when illuminated with on-axis divergent beam at distal end.

We notice intensity is greatest at the centre of the bundle, and tapers to the edges, reflecting the divergent illumination from the fibre-tip. Due to on-axis illumination, each core resembles a Gaussian-like mode.

Measurements are taken using 'ImageJ', an image editing software developed by the National Institutes of Health and the Laboratory for Optical and Computational Instrumentation [58]. First, we measure the pixel span across the diameter of the bundle, which comes to 749 pixels. The value for M is then given by the calculation:

$$M = \frac{749 \cdot 14\,\mu m}{1.05\,mm} = 9.9867 \tag{3.4}$$

This value is approximately equal to 10, confirming that our proximal magnification is performed correctly.

Next, we measure the core pitch, by calculating the pixel coverage per pitch. We measure 3 pitches to span 17 pixels, and the core pitch is hence given by the calculation:

$$p = \frac{17}{3} \cdot \frac{14\,\mu m}{9.9867} = 7.949\,\mu m \tag{3.5}$$

We can also calculate the number of camera pixels across a single core pitch, which is given by the calculation:

$$\frac{9.9867 \cdot 7.949\,\mu m}{14\,\mu m} = 5.670\,(pixels/pitch) \tag{3.6}$$

3.4 Angular Illumination

Modal Demonstration

Considering our design demands large angular injection, let us now experiment with angled illumination of the fibre bundle. To demonstrate modal behaviour with large angular incidence we first temporarily swapped the x10 MO to a x40 MO. We fed the illuminating fibre to a collimator and projected a collimated beam at an angle onto the bundle face. The collimated beam was incident at $\alpha = 0°$ and $\alpha = 20°$. The images are cropped to illustrate the modal profiles of each core, given in Fig. 3.4. We clearly see Gaussian-like profiles for normal incidence, and annular-like profiles for angled illumination.

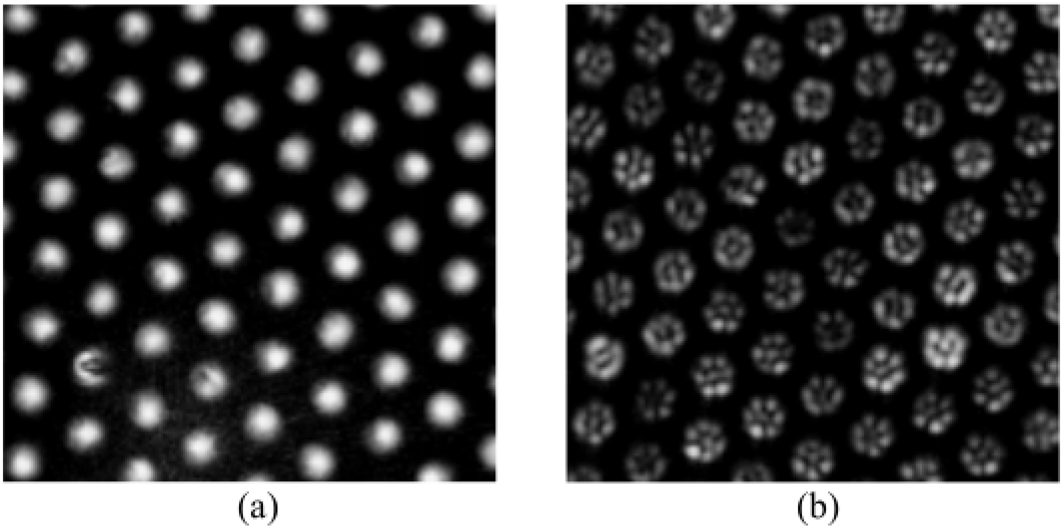

Figure 3.4: Demonstration of modal coupling from collimated beam; (a) Gaussian-like profiles for on-axis illumination, and (b) higher order coupling for 20° incidence.

Divergent injection

Next, let us return to our fibre illumination set-up, with a divergent beam projected onto the bundle, and let us return to our x10

MO at the proximal end. We can achieve control of the angle of illumination by rotating the custom made mount, and with each angle re-adjusting the position along x to re-centre the beam. A protractor is used to approximately measure the angle of the fibre. The tip of the fibre is brought close to the bundle face, so as to illuminate only a central region. The diameter of the beam is approximately matched in each case by adjusting the distance from fibre-tip to bundle face, ideally trying to match the distance at each angle. An example set-up, with $\alpha = 10°$, along with the resultant image cropped to the central 250 x 250 pixels ($\approx 350\mu m$), are given in Fig. 3.5,

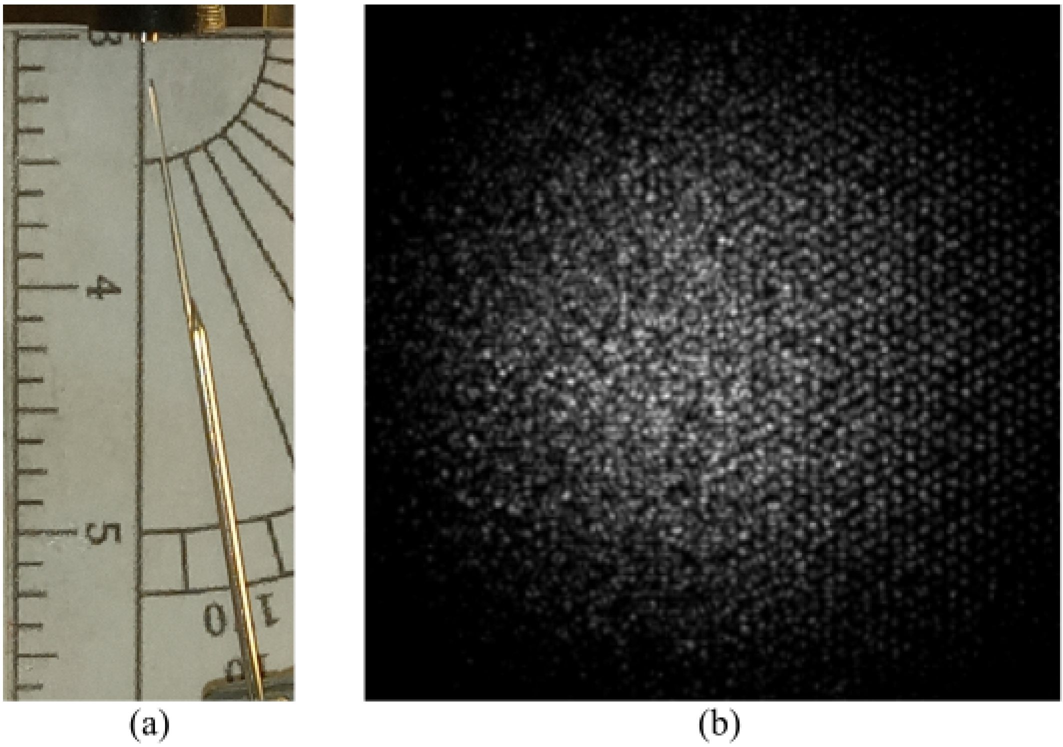

Figure 3.5: Demonstration of angular illumination; (a) photograph of fibre inclined at 10°, (b) image obtained with fibre inclined at 10°

Let us vary the angle of incidence and obtain images at each angle, matching the fibre to bundle distance for each angle. Images are captured at 0°, 5°, 10°, 15°, 20° and 25°. Due to the angular acceptance of cores, the intensity diminishes with each successive image. Ideally, the camera exposure, τ, would be set at a fixed value, such that the image at 0° is just below saturation, and the drop off of intensity then measured from 0°. However, in order to capture sufficient intensity at larger angles, we instead normalized at 5°, and for 0° reduced the exposure. Even at such an exposure, images at angles >15° are close to zero in intensity. Images at angles from 0° to 20°, cropped to a 120 x 120 pixel ($\approx 170\,\mu m$) FOV at the centre of the bundle, and shown in Fig 3.6.

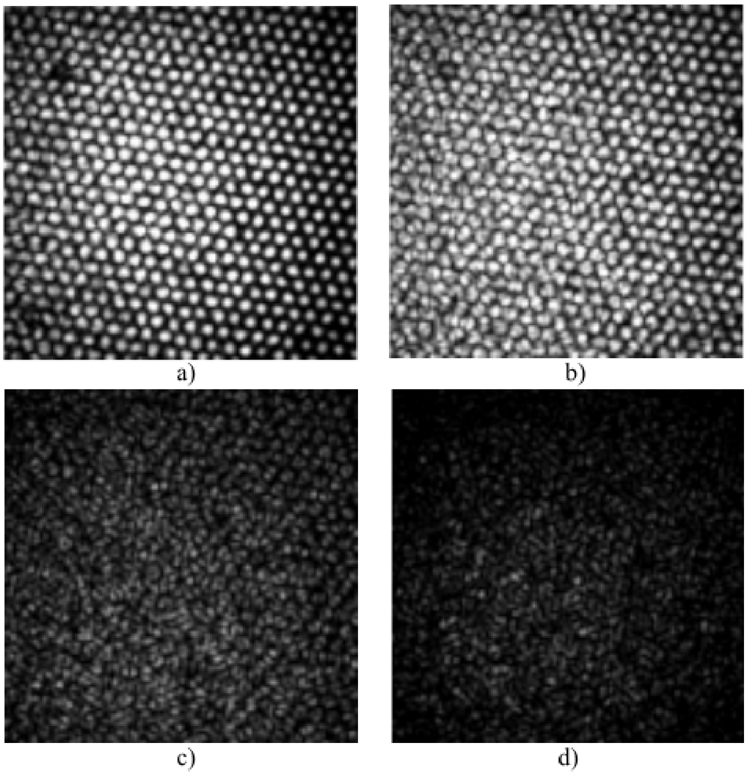

Figure 3.6: Images obtained with varying angle of fibre; a) 0°, b) 5°, c) 10° and d) 20°, each cropped to 120 x 120 pixels ($\approx 140\,\mu m$) at centre of image.

3.4.1 Angular acceptance

An angular acceptance plot was calculated for angles 5° to 20°, with the analysis performed in Matlab. First, a duplicated set of images with re-mapped contrast were obtained, using the 'imadjust' function. This increases the image contrast by mapping the image's intensity range to the full range. This allowed the beam diameter to be measured at each angle, from which a distance correction factor was obtained, relative to the diameter at 5°. The centroid of each image was then computed, from which the mean intensity in a 200 x 200 pixel ($\approx 280\ \mu m$) region about the centroid was calculated. The mean values are then multiplied by the correction factor, to normalize the intensity of light projected onto each region. The plot is given in Fig. 3.7, where values of intensity are normalised to the 5° value.

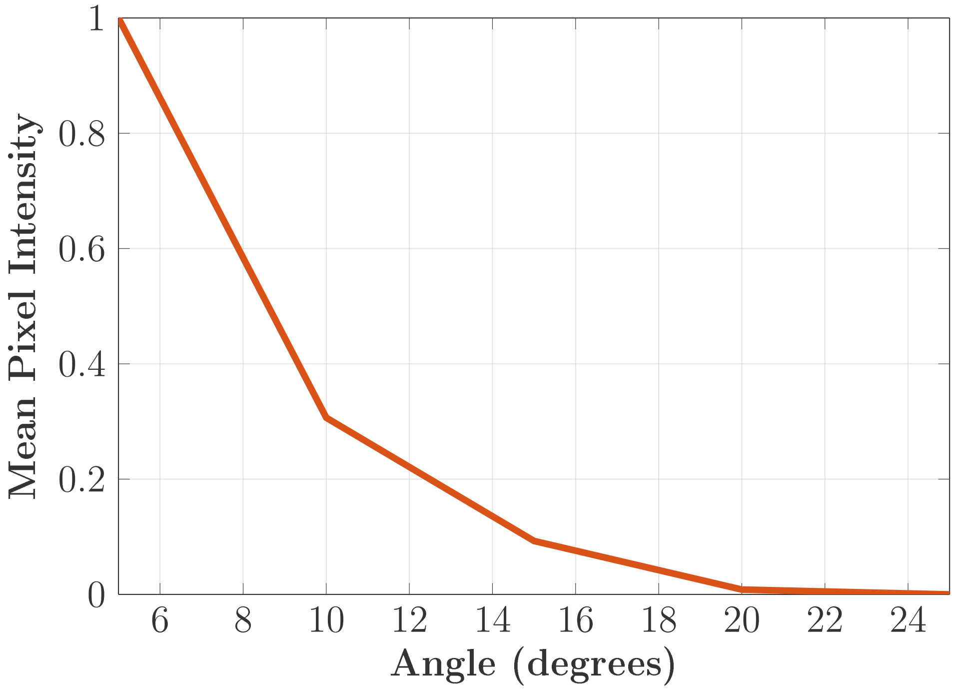

Figure 3.7: Experimentally obtained angular acceptance plot of fibre bundle when illuminated with a divergent beam, normalized to the intensity at 5°.

3.4.2 Coupling-behaviour

In addition to reduced power coupling with angle, we have also observed in our images the coupling of intensity into higher order modes, as well as coupling into the inter-core spacing. To perform OCT, we prefer light to be coupled into the first mode, as multiple effects occur due to higher order coupling which severely degrade the OCT signal.

Higher order modes experience a higher effective refractive index, and hence a greater OPD. When light is coupled into multiple modes, this results in spurious repeated artefacts in depth through the OCT image, referred to as ghost artefacts, with deeper artefacts corresponding to higher order modes with greater OPD [59]. Modal dispersion also occurs, having the effect of broadening axial resolution as well as a degrading of the shape of A-scan peaks [59]. In addition to a preference for coupling into the first mode, we also want light to be confined to within cores, reducing the extent of cross-talk.

Let us consider comparing the 15° and 0° images, cropped to an 80 µm square FOV at the centre of the bundle, to demonstrate the coupling behaviour in each case. These are given in Fig. 3.8 with 15 µm scale bars. In the 15° image we observe a departure from Gaussian-like profiles, with profiles representing higher order modes. We also observe some intensity distributed into the inter-core spacing, potentially representing cross-talk. Both of these effects make the illumination unsuitable for OCT. This can be compared to the case of on-axis illumination, where we observe Gaussian-like profiles and minimal intensity within the inter-core spacing.

To analyse the unsuitable coupling for OCT at larger angles, we produce line profiles along the central 100 pixels ($\approx 140 \mu m$) for the 0° and 15° cases. The raw images are rotated by a small angle of 8.8°, aligning cores along the vertical direction, whilst still approximately preserving the beam tilt along the horizontal direction. A vertical profile is then taken across the centre of the image through

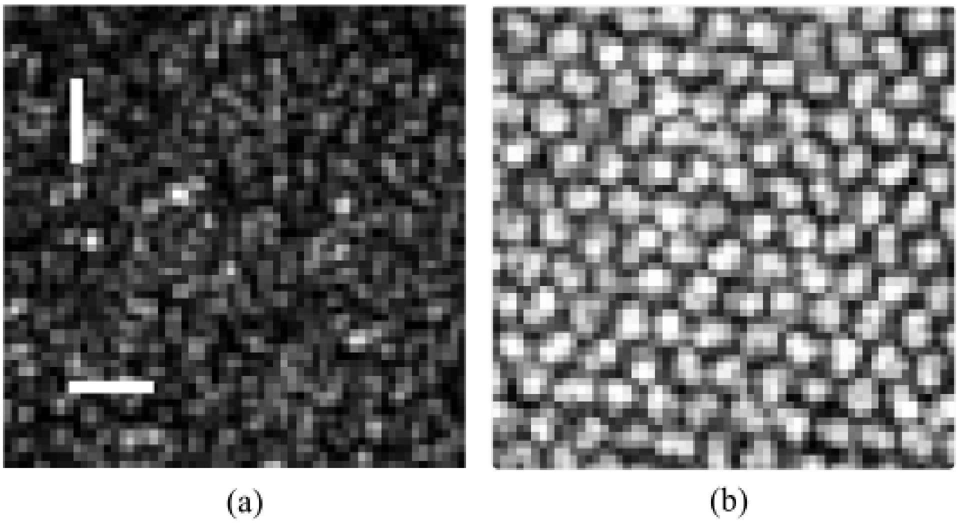
(a) (b)

Figure 3.8: Demonstration of modal and cross-coupling behaviour, for (a) 15° and (b) 0°. Images cropped to an 80 µm FOV with 15 µm scale bars.

a line of cores, approximately orthogonal to the beam direction. Values of intensity are normalized to the 0° case. The profiles are given in Fig.3.9, where 0° is given in blue and 15° in orange.

We see that for 0° we observe Gaussian resembling high intensity peaks, representing predominantly lower order coupling. For the 15° profile we observe the expected reduced total coupled intensity. We also observe a broader distribution of intensity, with no high peaks, and intensity distributed into the inter-core spacing. This suggests a presence of higher order modes, which have more of their power coupled into the cladding surrounding the cores. Intensity spread into the inter-core spacing also means more potential for cross-talk between cores.

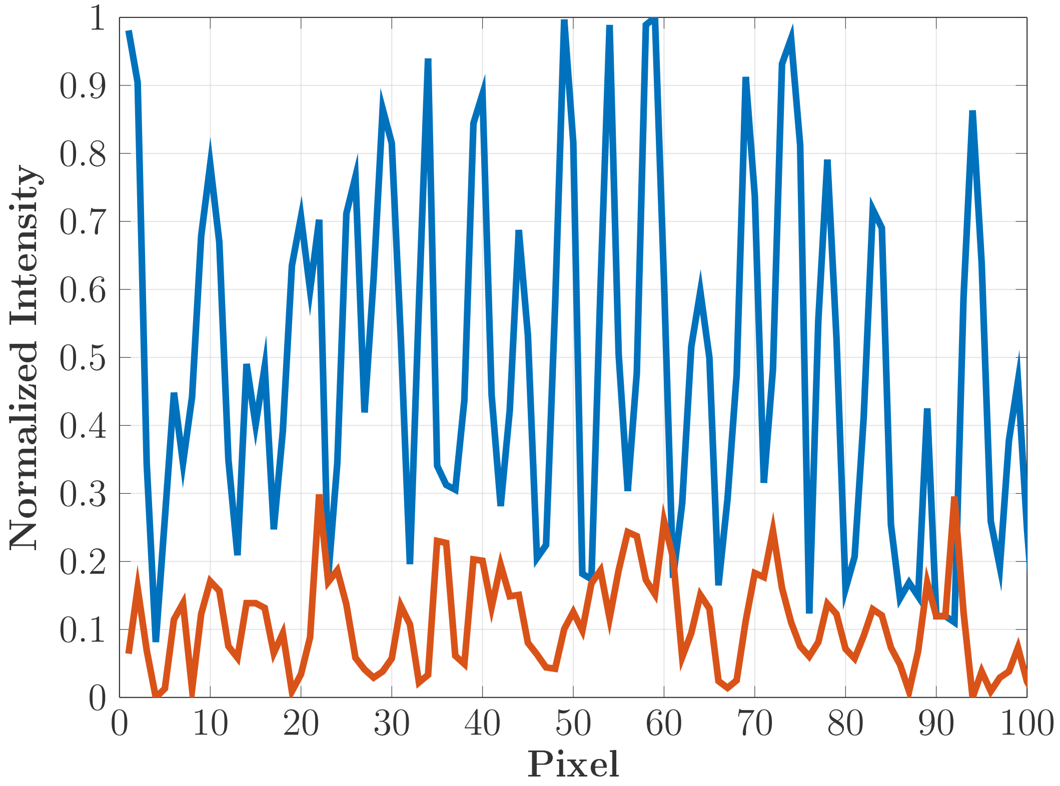

Figure 3.9: Line profile across the central 100 cores for $\alpha = 0°$ (blue) and 15° (orange).

3.5 Diffused core injection

We require a solution, such that, given large angular illumination of a divergent beam, we can obtain a close to normal incident injection of cores, therefore obtaining a coupling suitable for OCT.

The solution we have found is to place a diffuser directly at the distal face of the bundle. The action of the diffuser can be explained with reference to Fig. 3.10. A ray of light incident onto the diffuser emerges from the other side as a diverging beam. The diffuser is characterized by the diffusing angle, θ, which is the half angle of the emitted cone. As illustrated, a ray incident at α is diffused into a divergent cone, whereby the ray at the extremity is approximately on-axis. Light is still projected into the cores at many angles, however due to the far superior coupling efficiency at near to on-axis, the resulting effect is that most of the injected light is coupled into the on-axis and near to on-axis modes. In this way, in theory, the diffuser can be used to obtain near to on-axis illumination.

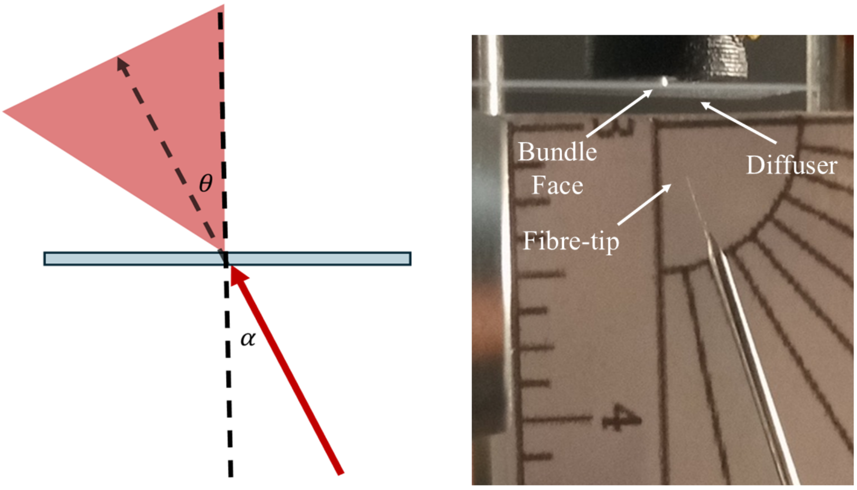

a) b)

Figure 3.10: Use of diffuser at distal face; a) illustration of effect of diffuser, and b) photograph of diffuser placed flush with bundle face

3.5.1 Diffuser Selection

The main parameters to consider are the thickness of the diffuser and the diffusing angle, θ. Thinness is required to minimise intensity loss through the diffuser and also to minimise loss of resolution, i.e when imaging onto the bundle through the diffuser. A set of diffusers with varying value of θ were obtained from Luminit. All diffusers were approximately 0.25 mm thick, which was the thinnest available. Diffusers with $\theta = 20°, 40°, 50°, 60°$ and $80°$ were acquired and tested. These represented the entire range of diffusing angles available from Luminit. Other diffusers were also acquired from different manufactures and tested. However, Luminit diffusers were found to produce the best images, in terms of generating a favourable modal coupling for OCT.

For each diffuser the fibre was inclined at approximately $\alpha = 20°$, and an image was captured. The exposure, τ, was kept constant for each diffuser. The images are shown cropped to a 200 x 200 pixel ($\approx 280\,\mu m$) FOV in Fig. 3.11.

We clearly see the improved coupling with larger diffusing angles. From the perspective of a solution to off-axis coupling, we see that diffusers 60° and 80° produce the best coupling, presenting the closest to a uniform distribution of intensity, and exhibiting predominately Gaussian-like profiles. However, we must also balance improved off-axis coupling with minimal intensity and resolution loss of light imaged through the diffuser onto the bundle. The investigation of the effects of the diffuser on the object image is presented in Chapter 4. The conclusion is that 40° provides the best trade-off. The main barrier to using larger diffusing angles is the intensity loss through the diffusers. Even when flush with the bundle face, diffusers with $\theta \geq 40°$ did not allow enough image intensity to perform OCT.

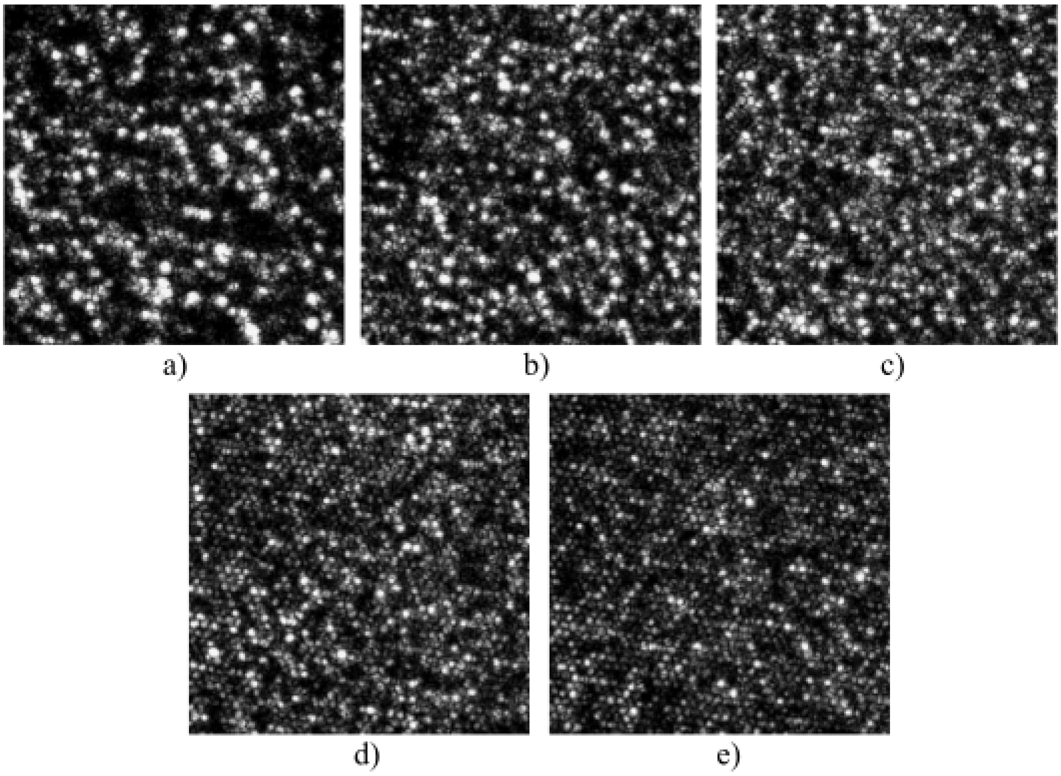

Figure 3.11: Images obtained from diffusers with different θ , with fibre inclined at 20°, cropped to central 200 x 200 pixel ($\approx 280\,\mu m$) FOV, for $\theta =$; a) 20°, b) 40°, c) 50°, d) 60° and e) 80°.

3.6 Diffuser Characterization

Let us characterize core injection from angled illumination when the 40° diffuser is placed flush at the bundle face. Images were obtained for $\alpha = 0°$ to $\alpha = 35°$, in steps of 5°. Images cropped to the central 120 pixels ($\approx 170\,\mu m$), are shown in Fig. 3.12.

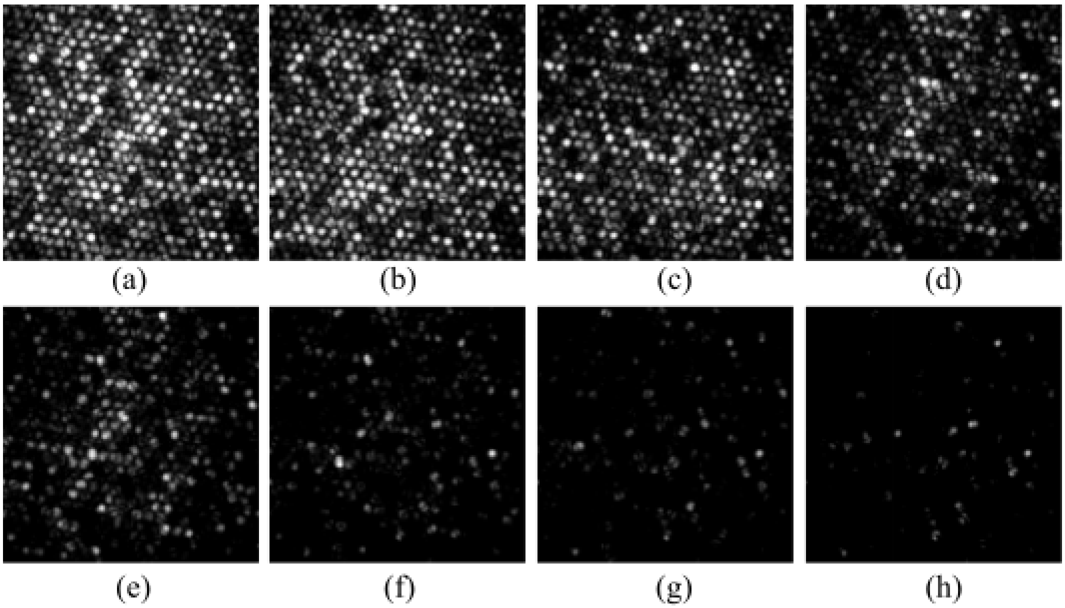
(a) (b) (c) (d)
(e) (f) (g) (h)

Figure 3.12: Images obtained with $\theta = 40°$ diffuser in place, for fibre angled at; (a) 0°, (b) 5°, (c) 10°, (d) 15°, (e) 20°, (f) 25°, (g) 30° and (h) 35°.

We observe a reduction in intensity with increasing angle of incidence. In terms of modal coupling; for lower incidence angles, (a) to (d) (0° to 15°), we see a majority of lower order modes. For higher angles (e) to (h), it is not entirely clear, as the intensity is drastically reduced, however we perhaps start to see increasing proportions of higher order modes.

3.6.1 Angular acceptance

We perform the same experiment and analysis to obtain the angular acceptance plot with the diffuser in place. This is plotted in Fig. 3.13, with acceptance with the diffuser in place in solid blue, and the previously obtained acceptance without the diffuser in dashed orange. Both plots are normalized to the 5° intensity with no diffuser in place.

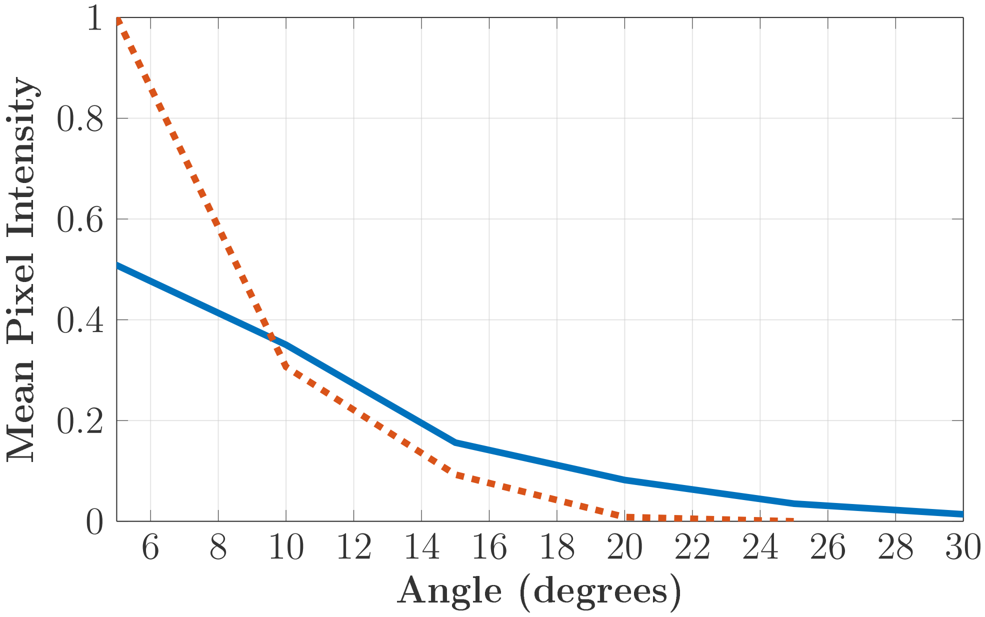

Figure 3.13: Experimentally derived angular acceptance from diverging beam; with diffuser in place (solid blue) and without diffuser (dashed orange).

We see that for $\alpha \leq 10°$, a greater intensity is achieved without the diffuser. However, for larger angles, $\alpha \geq 10°$, more power is coupled with the diffuser in place.

3.6.2 Modal behaviour

Images were obtained with and without the diffuser in place, with an angle of $\alpha = 15°$, as given in Fig. 3.14.

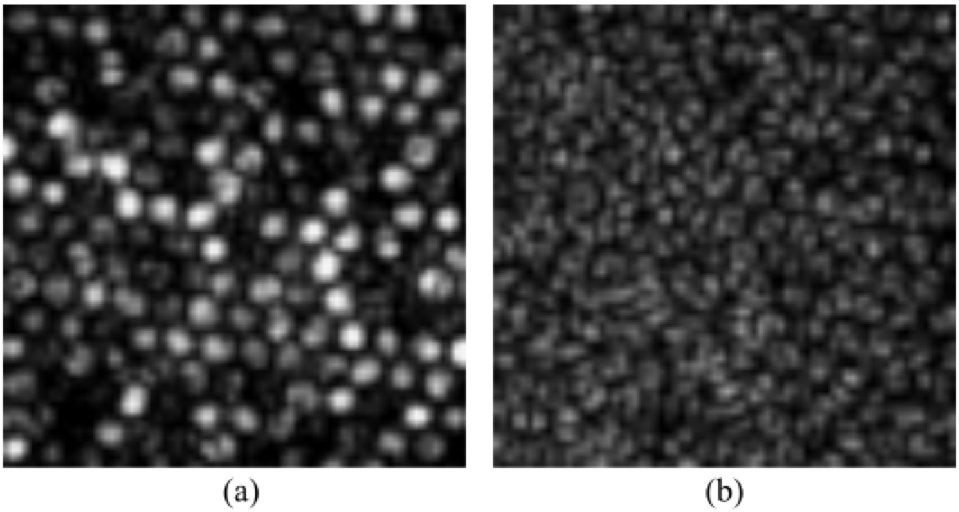

Figure 3.14: Images obtained for $\alpha = 15°$; (a) with diffuser in place, and (b) without diffuser.

We repeat the same experiment and analysis to obtain the line profiles across cores with the diffuser in place. The profiles along the central 100 pixels ($\approx 140\,\mu m$), when illuminated with $\alpha = 15°$, are given in Fig. 3.15, for the case with the diffuser in place in solid blue, and without the diffuser in place in dashed orange. Both plots are normalized to the maximum pixel intensity with the diffuser in place.

We see that with the diffuser in place we have re-obtained high intensity Gaussian-like peaks, likely resembling zero order coupling. However we can also observe that this is not uniform across the profile, with some cores presenting little to no intensity. For instance, between pixels 85-95, we see the presence of a core, exhibiting intensity without the diffuser but almost no intensity with the diffuser in place.

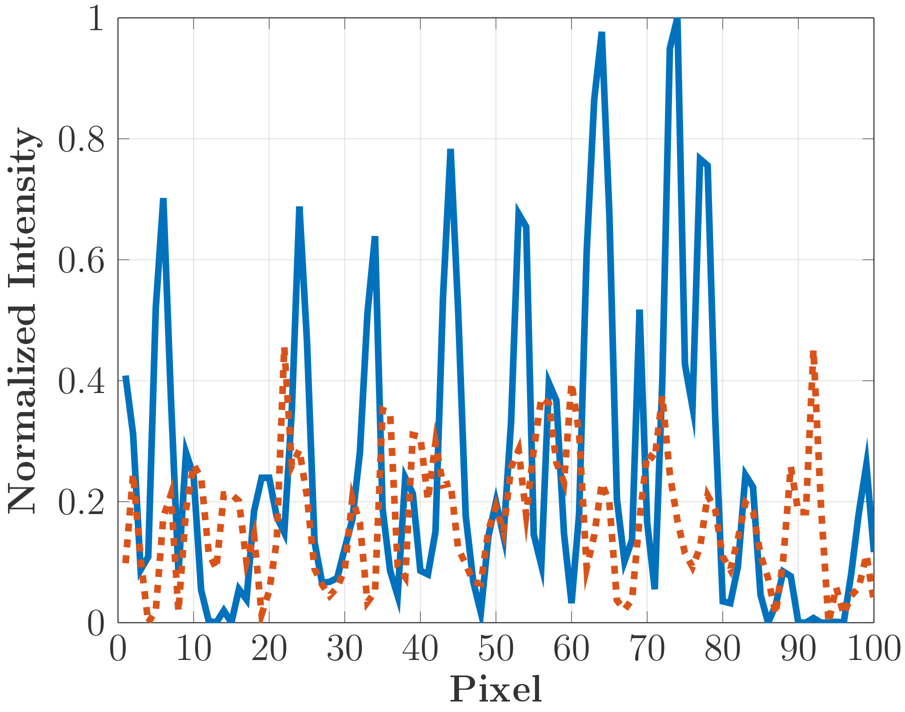

Figure 3.15: Line profile across the central 100 pixels ($\approx 140\ \mu m$) for $\alpha = 15°$, with diffuser in place (solid blue) and without diffuser in place (dashed orange).

3.7 Conclusion

This chapter addressed the problem of attaining a coupling of light into the cores of a fibre bundle that would be suitable for OCT, when injected with a divergent angled beam, as is required for our common-path design.

We initially confirmed that at large angles, we obtain a significantly reduced coupling efficiency, a greater excitation of higher-order modes, and increased cross-talk between cores. This confirmed that at large angles of incidence the coupled light is unsuitable for OCT.

In response, we proposed the use of a thin optical diffuser placed flush with the bundle face. The diffuser scatters the incident beam, resulting in greater coupling efficiency and a greater distribution of coupled power into lower order modes.

Experiments demonstrated that diffusers with higher diffusing angles resulted in a more suitable coupling for OCT. However, larger angles could not be used, as they imparted too much attenuation of near to on-axis light, meaning imaging through diffusers with larger diffusing angles would not be feasible. A 40° diffuser was found to offer the best trade-off between coupling quality and usable signal intensity.

While not a perfect solution, the diffuser enables sufficient on-axis coupling of angled illumination, making it viable for our system. This solution allows us to move forward with building the OCT setup, presented in the next chapter.

Chapter 4

Fibre Bundle OCT Adapter

4.1 Introduction

In this chapter we present our design of a forward-viewing fibre bundle OCT adapter, utilizing a 4f telescope equipped with angled divergent object illumination and an off-axis divergent injection into a bundle. This presents a compact solution for performing common-path fibre bundle OCT.

We first describe the object imaging component of the adapter, presenting the optics and discussing some of the implications of angled divergent illumination, such as the varying angle of incidence along the object. We assemble the adapter and introduce the object fibre, and perform imaging of a calibration phantom, using the known pitch of the sample to calibrate the system. We then characterize lateral resolution using a USAF target and analyse the impact to resolution from applying a Gaussian filter to remove the core pattern.

We then present the OCT functionality of the adapter, explaining the position of the reference beam, and discussing the importance of correctly aligning the reference fibre so as to be co-aligned with the object fibre. We construct the proximal components of the Full-field Swept Source OCT system and position the adapter and bundle into the OCT system. We perform OCT with the reference fibre at two cases, with the fibre correctly co-aligned with the object fibre, and with the fibre incorrectly placed anti-aligned with the object fibre. B-scans are produced for the two cases, demonstrating the expected apparent object tilt in the case of misaligned fibres.

4.2 Imaging onto the bundle

Our first step is to image an object onto the distal face of the bundle, with optics that are amenable to miniaturization and hence application in endoscopy.

4.2.1 Selection of distal optics

Several arrangements of distal optics have been explored, such as a single lens, a 4f telescope, and a gradient index (GRIN) lens [60], each presenting differing advantages and disadvantages. In either case, for practical use in endoscopy, we require lenses of a small diameter, and require a short total length of the optics.

Single lens

A single lens is the simplest and most compact option. It also has minimal optical elements, therefore creating less of a dispersion mismatch between object and reference paths.

However, a single lens is highly susceptible to aberrations, especially with off-axis illumination, limiting the usable field-of-view (FOV). Additionally, with a single lens, the inherent trade-off between FOV and lateral resolution cannot be adjusted, and is fixed by the working distance of the lens, whereby decreasing the working distance improves resolution but reduces the effective FOV, and vice versa [61].

GRIN lens

The GRIN lens is a highly compact option, typically employed with a small working distance, making it well-suited for high resolution imaging over a small FOV. With increasing working distance the GRIN lens typically exhibits greater aberrations, which are especially pronounced with off-axis illumination [62].

4f Telescope

The 4f telescope configuration offers several advantages, especially with respect to off-axis illumination. It has improved field flatness over the single lens or GRIN options, providing a larger useable FOV.

The 4f also grants more flexibility with regards to adjusting of FOV and lateral resolution. While a fundamental diffraction limited trade-off is still imposed, the two parameters can be adjusted; bringing the first lens closer to the sample to improve resolution, and similarly, moving the bundle away from the second lens to widen the FOV.

One negative of the 4f is its larger overall size, requiring a total length of 4f, making it considerably longer than the other options.

4.2.2 4f-Telescope - Angled illumination

The set-up for imaging an object onto the distal face of a bundle through a 4f-telescope, using angled divergent illumination from a single-mode fibre (SMF), is illustrated in Fig.4.1.

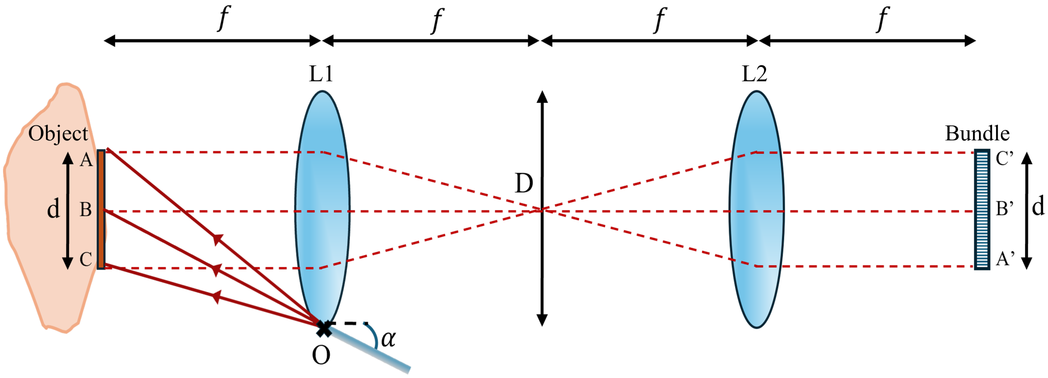

Figure 4.1: Diagram of 4f telescope with angled divergent illumination from off-axis object fibre, positioned at O and inclined at angle α.

The 4f-telescope is constructed from two identical plano-convex (PCX) lenses (Edmund Optics: 47-852), with diameter, $D = 4mm$, and focal length, $f = 8\ mm$. An alternative telescope was also assembled from achromatic doublets, (Edmund Optics: *Discontinued*), having $D = 4\ mm$ and $f = 4\ mm$. However, this telescope demanded too large of an angle of illumination for efficient core injection of the bundle suitable for OCT. Therefore the focal length was doubled, halving the angle of illumination. At the time of assembling our system we did not find any achromats having dimensions producing this minimal angle, whereas PCX were available.

A first lens, $L1$, and a second lens, $L2$, are separated by $2f$. The object is located at f from $L1$, sitting in the adapters objective plane. The bundle sits at f from $L2$, sitting in the telescope's image plane. Provided all separating distances are as stated, the two lenses form a 4f telescope with unitary magnification, mapping the object into an image on the bundle face.

Illumination is facilitated with a divergent beam incident from off-axis, emitted directly from the end of an object fibre, with no intermediary lenses. The tip of the object fibre is positioned at O, and is inclined at an angle α to the optical axis. The object fibre is taken from a port of a fibre-couple, connected to our swept source. The minimum possible angle that the fibre can be inclined at, α, is determined by D and f, given by

$$\alpha = \arctan\left(\frac{D}{2f}\right) = \frac{4\,mm}{18\,mm} \approx 14^\circ \tag{4.1}$$

The NA of the objective lens, $L1$, is given by:

$$NA = \frac{D}{2f} = \frac{4\,mm}{16\,mm} = 0.25 \tag{4.2}$$

From which the half acceptance angle, $\theta_{\frac{1}{2}}$, is therefore:

$$\theta_{\frac{1}{2}} = \arcsin(0.25) = 14.5^\circ \tag{4.3}$$

Hence, specular reflections are barely captured at the very edge of $L1's$ acceptance cone. Any captured light passes through the edge of the lens where aberrations are at their greatest. In practice, due to any slight misalignment of $L1$, no light is captured from a flat specular sample, and no image is formed onto the bundle.

As such, imaging relies on scattering from the sample, or from the tilting of a specular sample. In the case of a flat scattering sample, light is scattered in a cone about the specular reflected ray, and this cone overlaps with the lenses acceptance cone, allowing a portion of light to be imaged onto the bundle. Light scattered from the object at points on the object; A, B and C, are imaged onto points of the bundle face A',B' and C'.

Varying angle of illumination

At the centre the object, at B, the angle of illumination is equal to α. Due to the beam being divergent, the angle of illumination varies across the FOV. In the vertical plane (plane of figure), the beam angle increases in the direction of the inclined fibre. At C the angle of incidence is at its minimum, and at A is at its maximum. In the horizontal direction (orthogonal to figure), the beam angle also increases very slightly in both directions away from the centre of the object, due to the curved wavefront of the divergent beam.

Beam size

The fibre end is sufficiently far from the object such that the divergent beam covers a FOV exceeding the bundle area. In our case, using SMF with $NA \approx 0.12$, at a distance of approximately $f = 8\,mm$, the beam diameter is: $2 \cdot NA \cdot f = 1.92\,mm$, therefore comfortably exceeding our required FOV. However, this design feature must be considered with regards to further miniaturization, as the beam area will subceed the bundle area for cases of $f \leq 4.375\,mm$.

In such cases, a practical solution could be to use ball-lensed fibre tips, which exhibit increased NA. For instance, commercially available ball lenses directly fused to fibre tips can increase NA to 0.35–0.5, depending on the ball diameter and refractive index [63]. As an example, considering our bundle with a diameter of 1.05 *mm*, and a ball-lensed fibre with $NA = 0.35$, the distance could be reduced to as little as 1.5 *mm* and form a FOV equalling the bundle area.

Lateral resolution

Assuming diffraction-limited resolution, with coherent illumination, the smallest resolvable feature on the object, is given by the NA of the objective lens, $L1$;

$$\Delta_{x,y} \approx \frac{\lambda_0}{NA} \approx \frac{0.85\,\mu m}{0.25} = 3.4\,\mu m \tag{4.4}$$

However, in practice the attainable resolution is broadened, principally due to aberrations induced by lenses. Aberrations are particularly pronounced from smaller lenses, due to increased difficulty in accurately manufacturing the lenses, as well as a greater difficulty in accurately aligning the lenses. The degradation of the attainable resolution from the diffraction limited value is hence more pronounced when using smaller lenses. A more realistic estimate of the attainable resolution from small lenses, would be at least twice the diffraction limited value, e.g. $\Delta_{x,y} \geq 7\mu m$.

Given our core pitch is $p \approx 8\ \mu m$, the fundamental limit on lateral resolution is determined from the core pitch of the bundle and the magnification of the 4f telescope. Assuming $M = 1$, and considering the Nyquist sampling limit, the lateral resolution, $\Delta_{x,y}$, in terms of line pairs per mm (lp/mm), is given by;

$$\Delta_{x,y} = \left(\frac{2p}{M}\right)^{-1} \approx 62.5\, lp/mm \qquad (4.5)$$

FOV

In theory, the diameter of the FOV is determined by the bundle diameter, d, and the telescope magnification, M. Assuming unitary magnification, this gives

$$FOV_{diam} = M \cdot d = 1.05\, mm \qquad (4.6)$$

However, in practice, due to aberrations through the telescope, which are particularly apparent with off-axis illumination, the attainable FOV is likely to be less than that given by the bundle diameter.

4.2.3 Zemax Modelling

Zemax modelling of the telescope was conducted prior to assembly, to assess the expected extent of aberrations, and to consider the effectiveness of introducing an aperture stop at the centre of the telescope to mitigate aberrations.

At the time of producing the following Zemax work, we had the intention of using achromatic doublets in the telescope, and so modelling was performed with achromats. However, as previously mentioned, we later abandoned achromats for PCX's, which at the time offered a lower NA, and therefore a lower angle of injection of reference light into fibre bundle cores. Given limited research time, we did not prioritise repeating Zemax modelling with the final used lenses. However, the work is still informative, as we demonstrated, in theory, the effectiveness of using a central aperture stop.

An illustration of the modelled telescope is given in Fig. 4.2.

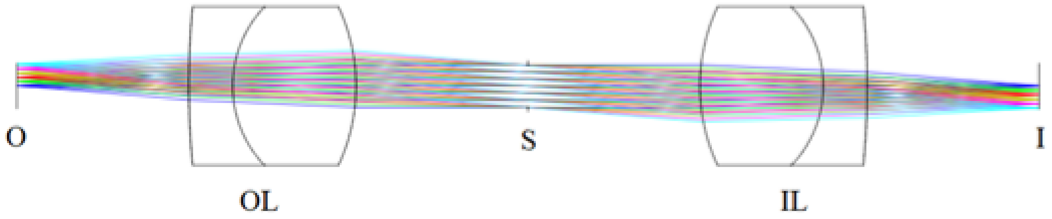

Figure 4.2: Illustration of the telescope as modelled in Zemax, in this instance formed from two identical achromats, an object lens (OL) and a image lens (IL), both oriented with their curved faces pointing towards the centre of the telescope. Light is imaged from the Object field (O) to the image plane (I).

To simulate the object field, we modelled a wavelength range representing the tuned bandwidth of the swept source. A set of 10 discrete wavelengths equally spaced from 820 nm to 875 nm were generated and weighted in power with a Gaussian function to approximately represent the tuned spectrum. The geometry of the field was circular and had a diameter of 1 mm, approximately matching that of the bundle.

Optimal Lens Configuration

We first determined the optimal configuration of two identical lenses, specifically achromatic doublets [Edmund Optics - 63714], with $D = 4\,mm$ and $f = 6\,mm$.

There are four possible configurations of two identical lenses in a 4f telescope. Let us label each configuration by referring to the faces directed toward the centre of the adapter i.e. Convex-Convex referring to the configuration illustrated in Fig. 4.2

For each configuration the Root Mean Square (RMS) of the Point Spread Function (PSF) at the edge of the image, at 0.5 mm from the centre, was measured. No central stop was included, and the stop diameter was taken as 3.7 mm, equalling the clear aperture of the lenses. The measured RMS values of the focused spot size at the edge of the FOV for each configuration are given in Tab. 4.1.

Table 4.1: RMS spot sizes for various lens configurations (in μm).

Configuration: Object Lens–Image Lens	**Edge PSF RMS (μm)**
Convex–Convex	18.6
Convex–Flat	135
Flat–Convex	454
Flat–Flat	973

Clearly, the Convex-Convex configuration is optimal. Without any central stop between the lenses, the modelled RMS of the PSF at the edge of the FOV was 18.6 μm

Aperture Stop Optimization

An aperture stop at the centre of the telescope would have the effect of reducing aberrations and achieving a better image at the edges of the FOV.

Let us use the Strehl ratio, *Strehl*, as a metric for the telescope's tolerance to aberrations, whereby typically, a system *Strehl* approximately ≥ 0.8 is considered tolerant to aberrations.

The Strehl ratio is defined as the ratio of peak intensities of the PSF's, of one measured at the edge of the FOV, with an ideal diffraction-limited PSF, and is given by:

$$Strehl = \frac{I_{edge}}{I_{dif-lim}} \tag{4.7}$$

Reducing the diameter of the stop has the effect of reducing aberrations. However, reducing the stop diameter necessarily reduces the systems overall NA, causing a broadening of lateral resolution, as demanded in (4.4). We have already established that the attainable resolution of our fibre bundle adapter features a limitation imposed by Nyquist sampling limit of the bundle pitch. With our fibre bundle core pitch of approximately 8 μm, we are therefore limited to a lateral resolution of 16 μm.

Stop size optimization was performed on three different lenses, two different achromats and one PCX. The lens catalogues of three well-known suppliers (Edmund Optics, Thorlabs and Newport), were exhausted to find the smallest readily available achromats, which had a diameter of 2 mm. PCX lenses however continued to smaller diameters, and the smallest found PCX with 1.5 mm diameter was selected for the third model.

The results, giving the stop size diameter at which a tolerable Strehl ratio is achieved, along with the resultant lateral resolution, measured as the FWHM of the PSF at the centre of the lens, are given in Tab. 4.2 for the two achromats, and in Tab. 4.3 for the PCX.

The results demonstrate in theory that placing an aperture stop at the centre of the adapter proposes itself as an effective way of mitigating aberrations, whilst also maintaining a lateral resolution below the limit imposed from the core pitch.

Table 4.2: Performance metrics for achromatic doublet lenses, with focal length (f) and diameter (D).

f & D (mm)	**Stop Diameter** (μm)	**Lateral Resolution** (μm)	**Strehl Ratio**
6 & 4	480	6.49	0.86
4 & 2	160	6.46	0.79

Table 4.3: Performance metrics for PCX lenses, with focal length (f) and diameter (D

f & D (mm)	**Stop Diameter** (μm)	**Lateral Resolution** (μm)	**Strehl Ratio**
2 & 1.5	165	6.45	0.76

4.2.4 Practical limitations

However, practical considerations should be considered with regards to including a central aperture stop. Assembling a telescope with small lenses already presents practical difficulties. We must first provide a means of assembling the telescope, and controlling the positions of the lenses. Conventional optical mounts for lenses typical only go down to a diameter of 1/4" (6.35 mm), and therefore a custom approach to mounting lenses is required, the method of which is presented in the subsequent section.

To control the exact position of a central aperture stop, less than 0.5 *mm* in diameter, would however present a great difficulty. Principally, the axial position of the stop must be accurately executed in order for the stop to function correctly. This would require fine axial adjustment of the aperture stop, and this would be very difficult to implement within the small space between the two lenses.

4.2.5 Adapter assembly

The 'adapter' refers to a compact package that houses the 4f-telescope, as illustrated in Fig.4.3. Here, we use the word compact in reference to its potential amenability to endoscopy. In practice, the assembled adapter was 8 mm in diameter, and with 36 mm of length between the bundle end and the sample. This is currently too large for endoscopy, however owing to its cylindrical geometry, the adapter has the potential for miniaturization down to sizes amenable to endoscopy.

In our set-up, for ease of experimentation, the SMF is disconnected from the adapter, as shown in Fig.4.3(b), but in theory the fibre could be embedded into the adapter for compactness, as illustrated in Fig.4.3(a).

A cylindrical tube with inner diameter matching the diameter of the lenses was 3D printed, which functions as a casing, holding the lenses in place and forming the body of the adapter. The adapter is then fixed into a vertically arranged cage system, positioned at the distal face of the bundle. Assembling the adapter into a vertical arrangement was preferred, enabling for simple and horizontal placement of samples. To fix the lenses into the correct 2f separation, a central spacer was inserted between the lenses, which was formed from an aluminium tube cut to the length of approximately two back focal lengths (14.52 mm), therefore creating the desired $2f$ separation. Correct positioning of the adapter, such that the front lens sits at f from the object, and the back lens at f from the bundle, is achieved experimentally, using a phantom with a known feature pitch, and adjusting the position of the adapter vertically to approximately obtain a unitary magnification.

To facilitate illumination, the object fibre-tip is positioned at the edge of $L1$. This was implemented using the distal illumination set-up described in Chapter 3, i.e. with the fibre slotted through a needle, and the needle mounted to a rotation-XYZ stage, as illustrated in Fig.4.3(b).

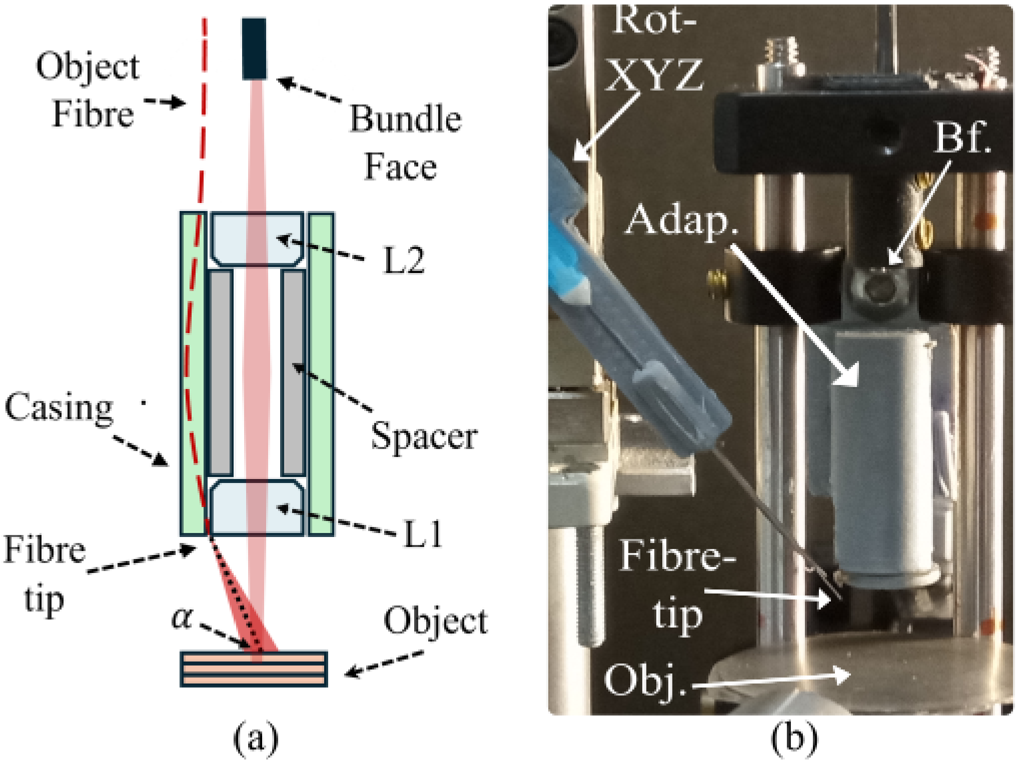

Figure 4.3: Object imaging with the adapter; (a) Illustration of the components of the adapter, and (b) photograph of the adapter assembly, with Adapter (Adap.) next to Bundle face (Bf.)

Size of Adapter

The effective length of the adapter, L, from object to bundle is $L = 4f = 32\,mm$. The outer diameter, $\oslash$, is equal to that of the supporting casing, which was; $\oslash = 8\,mm$. At these sizes, the adapter is not amenable to endoscopy. A sensible goal with regards to size would be to subceed the diameter of the working channel of typical endoscopes, which requires $\oslash \leq 3.7\,mm$ [64]. However, the sizes of the lenses used are of a similar order to that required for endoscopy, and some of the difficulties of imaging with small optics are encountered within our experimentation.

4.2.6 Phantom Imaging and Calibration

We first perform imaging of a phantom; a semi specular rough-metal disc, featuring a perforated pattern of holes with a fixed pitch, Fig. 4.4. This object was deemed appropriate, as it produced ample intensity at the camera when illuminated from off-axis, owing to its semi-specular nature. The large feature pattern was also useful for finding focus and calibrating the adapter.

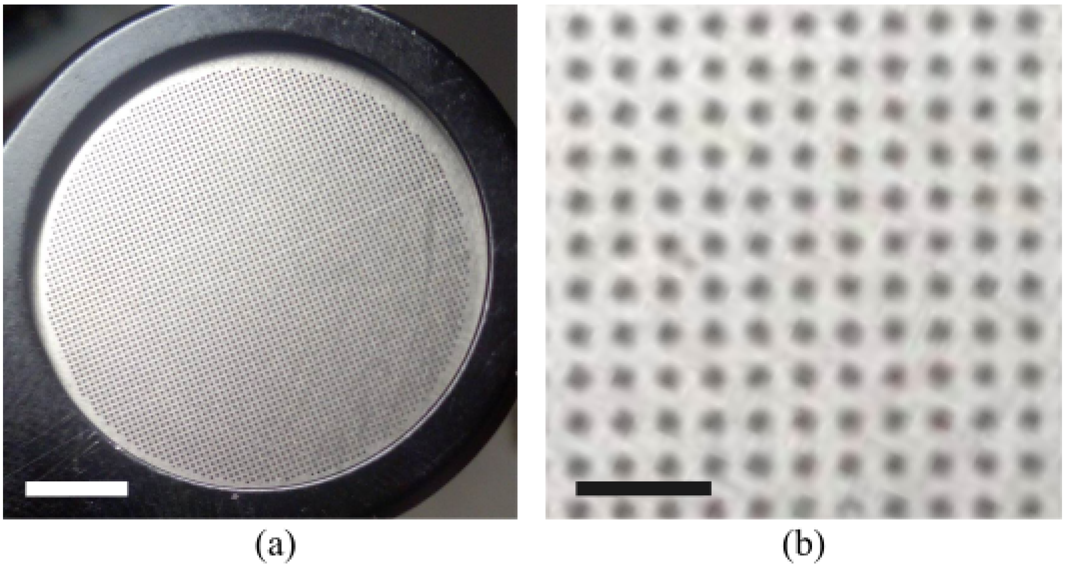

Figure 4.4: Photographs of phantom, (a) entire phantom, with 5 *mm* scale bar, and (b) cropped region illustrating regular pitch of phantom with 1 *mm* scale bar.

Physical measurements of the phantom were taken using vernier callipers, giving 68 pitches across a width of 22.64 *mm*, and therefore a phantom pitch of 332 μm.

The image obtained of the phantom with the adapter is given in Fig. 4.5.

We can use this image to perform a scale calibration, calculating the real distance across the object covered by a single pixel in the image. In an ideal placement of lenses within the adapter, with unitary magnification, the pixel coverage would be the camera

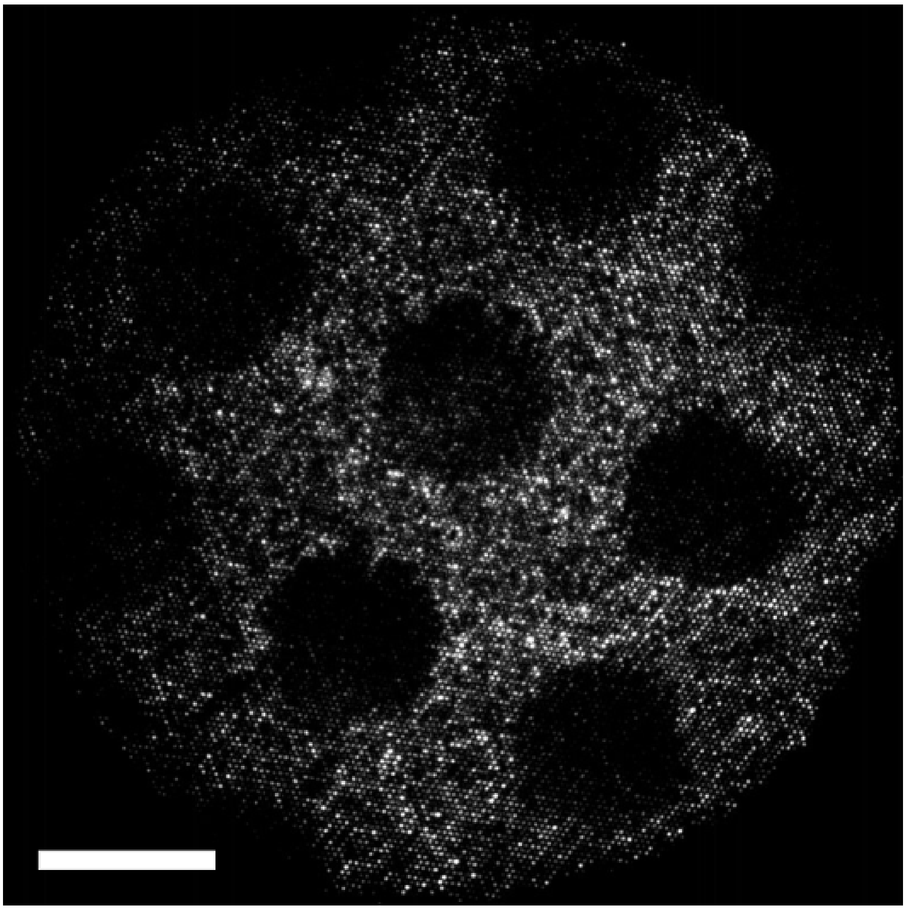

Figure 4.5: Image of phantom obtained from adapter, with 200 μm scale bar and total FOV of 1.09 mm

pixel size over the magnification of the proximal objective, giving $\Delta_{x,y} = \frac{14\,\mu m}{9.987} = 1.401\ \mu m$. However, in practice the adapter can have a slight departure from unitary magnification, due to imperfect spacing of lenses, or different distances of the adapter from the object/bundle.

We can measure the combined magnification of the adapter and proximal objective, using the known pitch of our phantom. The pixel span across a single phantom pitch was measured as 243 pixels. Therefore, one image pixel covers a real object distance of:

$$\delta_{x,y} = \frac{332\mu m}{243} = 1.366\,\mu m \tag{4.8}$$

The combined magnification of the proximal objective and the adapter, M, is hence:

$$M = \frac{14\mu m}{1.366\mu m} = 10.249 \tag{4.9}$$

We can then see that the magnification of the 4f telescope, M_{4f} is given by

$$M_{4f} = 10.249/9.9867 = 1.026. \tag{4.10}$$

This is approximately equal to our expected $M_{4f} = 1$, but indicates a slight discrepancy of either inter-lens spacing or vertical position of the adapter.

4.2.7 USAF Imaging and Lateral Resolution

To characterise the lateral resolution of our system, we next performed imaging onto a USAF test target. Due to the angled illumination, and imaging of a specular target, we tilt the USAF, enabling the reflected light to be imaged onto the bundle.

We demonstrate imaging with and without the 40° diffuser in place, cropped to group 4, with the highest resolvable line pairs circled in blue, as shown in Fig.4.6, and characterise the lateral resolution in each case.

Without the diffuser, the highest resolvable line pair is group 4, element 6, with a spatial frequency of 28.5 lp/mm, and resolvable feature size of 35.1 μm. This is somewhat lower than the theoretical value of 62.5 lp/mm. With the diffuser in place, only up to group 4, element 3, can be resolved, with $20.16 lp/mm$ and $49.6\,\mu m$ resolution. There is hence a loss in lateral resolution with the 40° diffuser in place. However, as was established in chapter 3, this is a necessary compromise in order to achieve coupling of our angled divergent beam, as is required for our common-path OCT design.

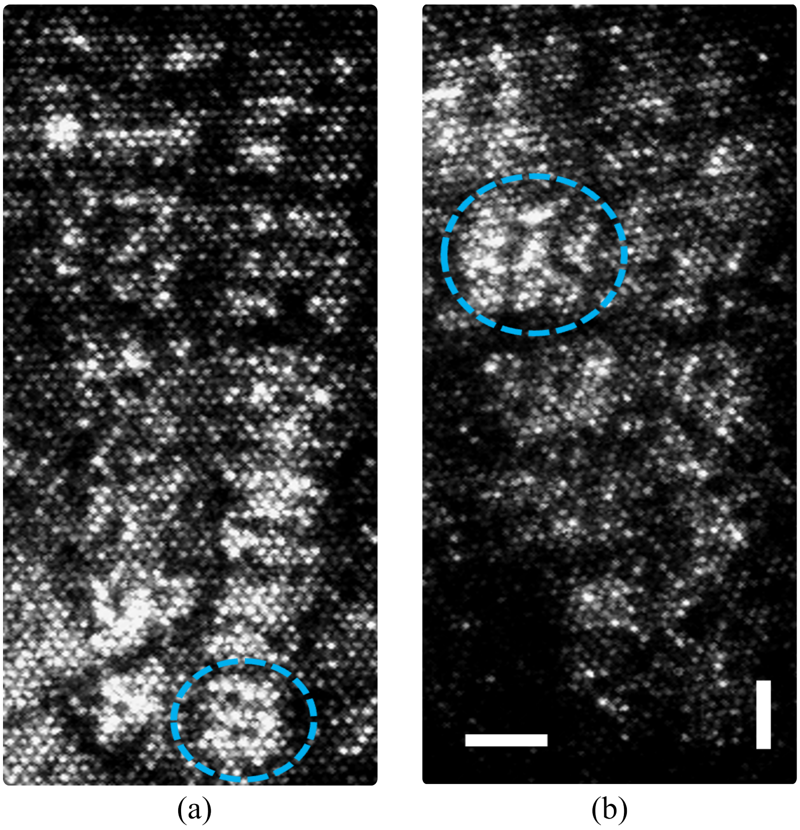

Figure 4.6: USAF test images with 50 μm scale bars; (a) without diffuser at bundle face and (b) with diffuser at bundle face.

4.2.8 Gaussian smoothing

Next, we experiment with a method of removing the core pattern from our images. A simple approach is to apply a 2D Gaussian filter in post-processing, which effectively smooths out the core pattern. More sophisticated approaches exist, for instance interpolation by Delaunay triangulation [9]. This however requires a flat-field calibration image to find the co-ordinates of each core.

To demonstrate the effect of Gaussian smoothing, and to characterise any loss of resolution, we apply a Gaussian filter of size 10 pixels (13.7 μm) to each of the USAF images.

In both cases, the same line pairs are still resolved after the filter

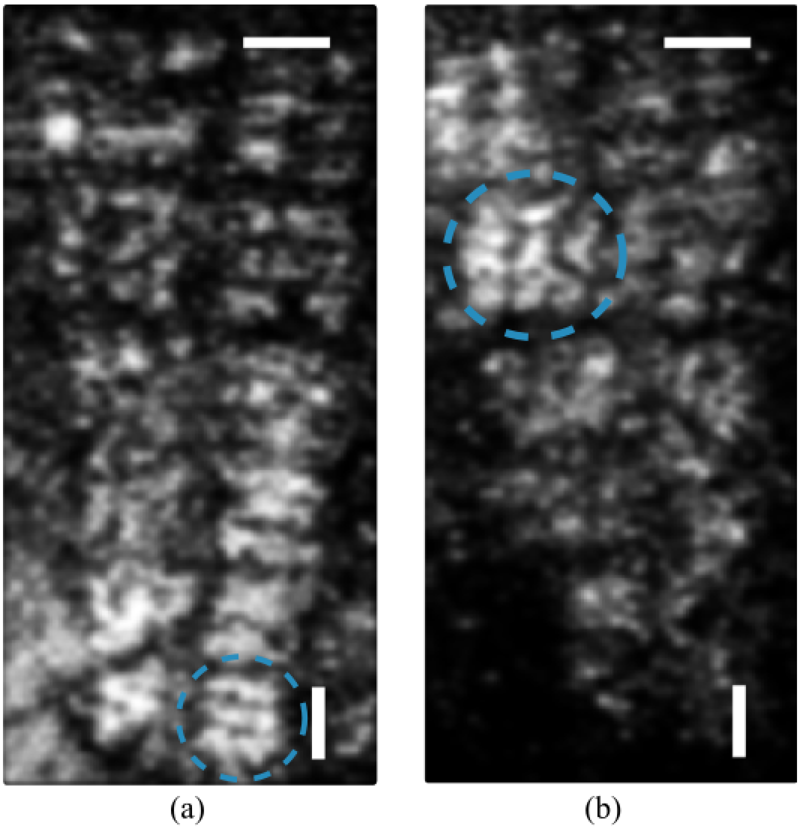
(a) (b)

Figure 4.7: USAF test images with Gaussian smoothing filter applied onto (a) image without diffuser, and (b) image with diffuser. Images with 50 μm scale bars.

has been applied, and the core pattern successfully smoothed. We can conclude that Gaussian smoothing is a good solution for our imaging system. This is because the core pitch at 8μm, is much less than our imaging resolution, i.e. 49.68μm with the diffuser in place. Hence, we can successfully apply a Gaussian filter of 13.7 μm, to smoothen cores, without any significant loss of imaging resolution.

4.2.9 Impracticality of core calibration

In incoherent fibre bundle imaging techniques, such as fluorescence endomicroscopy, a calibration of core intensities is typically performed prior to imaging, often having the effect of greatly improving image quality. This calibration compensates for irregularities in the intensities delivered across cores, due to manufacturing inaccuracies such as core imperfections and irregularities in core diameters.

Core calibration can be achieved by obtaining a flat field calibration image. From the flat-field input image, the intensities delivered from each core at the proximal end can be measured, and each core appropriately weighted, therefore normalising intensities across all cores.

However, this is difficult to achieve in practice with a coherent light source, due mainly to speckle-variance, induced by the coherent superposition of coupled modes. When the bundle is in use, the speckle delivered by each core randomly fluctuates, mainly due to bending of the bundle inducing deviations in OPD. These random fluctuations in intensity are difficult to calibrate for prior to imaging, although some methods have been explored [65].

Speckle-variance is also likely to be particularly pronounced under off-axis illumination, due to preferential coupling into higher order modes. As such, it was deemed impractical to perform a core calibration with the adapter.

4.3 OCT superposition via co-angled reference fibre

We have discussed in Chapter 1 that a common-path configuration is preferred for fibre bundle OCT. The method of generating a common-path arrangement is given in Fig.4.8. In addition to our object imaging set-up, we introduce a reference beam, derived from the reference fibre port of the fibre coupler. The tip of the reference fibre is positioned at the edge of L2, at the opposite side of the adapter, and is tilted at the same angle α, delivering a similarly diverging angled reference beam onto the bundle face. The reference beam comes into superposition with the image formed by the telescope at the bundle face, enacting a common-path.

In Fig.4.8, the diverging section of the object path is illustrated from the tip of the object fibre, at O_{Obj}, to the imaged plane on the sample, at points A, B, C, while the diverging section of reference path covers lengths from the tip of the reference fibre, at O_{Ref}, to the face of to the bundle at points A',B',C'.

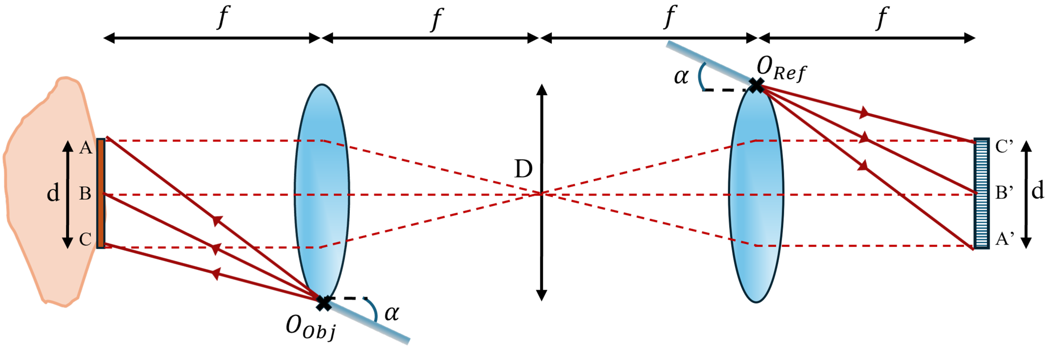

Figure 4.8: Diagram of common-path design with superposition at bundle face, by co-angled fibres projecting divergent beams onto the object and onto the bundle.

4.3.1 OPD Matching

Due to the sample and reference beams being divergent and tilted with respect to the optical axis, a varying OPD between the two arms of the interferometer can exist along the face of the bundle if the fibres are not correctly positioned as shown in Fig.4.8, resulting in a tilt or distortion in the OCT image.

Let us consider a single divergent section, the path covered by the reference beam, as illustrated in Fig. 4.9. Let us calculate the path lengths covered from the fibre to points A', B' and C' on the bundle face.

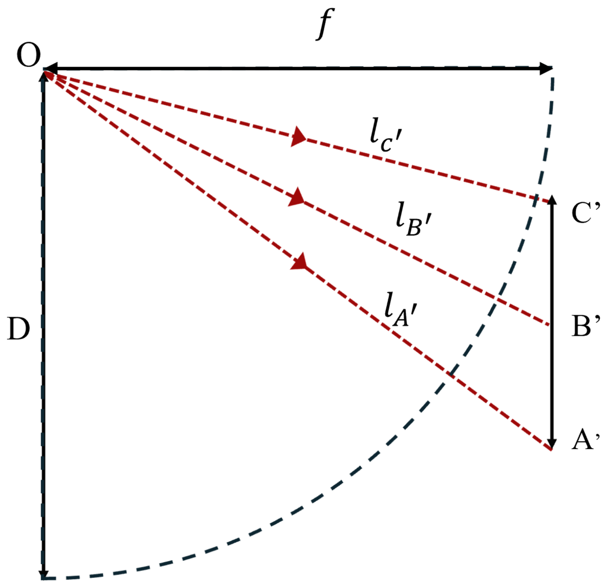

Figure 4.9: Diagram of the path lengths covered along the diverging section of the reference path.

By a simple geometric calculation, where d is the bundle diameter, we obtain the lengths,

$$
\begin{aligned}
l'_A &= OA' = \sqrt{\left(\frac{D-d}{2}\right)^2 + f^2} = \ 8.3890\,mm \\
l'_B &= OB' = \sqrt{\left(\frac{D}{2}\right)^2 + f^2} = \ 8.2462\,mm \\
l'_C &= OC' = \sqrt{\left(\frac{D+d}{2}\right)^2 + f^2} = \ 8.1348\,mm
\end{aligned}
\tag{4.11}
$$

Similarly, we can consider the path lengths along the diverging section of the object beam, from the fibre-tip to the points A, B and C on the object, as the lengths l_A, l_B and l_C. If the object and reference fibres are positioned on opposite sides of the adapter, both making the same angle with the tissue/bundle, and assuming the lenses form a unitary magnification telescope, as illustrated in Fig.4.8, then the length variations for both the object and reference beams are identical, that is;

$$
\begin{aligned}
l_A &= l'_A \\
l_B &= l'_B \\
l_C &= l'_C
\end{aligned}
\tag{4.12}
$$

We can arbitrarily define OPD as object path minus reference path. For this correctly aligned case, when we calculate the OPD at points on the bundle A',B' and C', there is no variation in OPD across the face of the bundle.

Misaligned case

However, let us now consider a case of extreme misalignment, whereby the object fibre is instead positioned on the same side of the adapter as the reference fibre, as illustrated in Fig. 4.10. Of course, we could have moved the reference fibre equally to obtain the same effect.

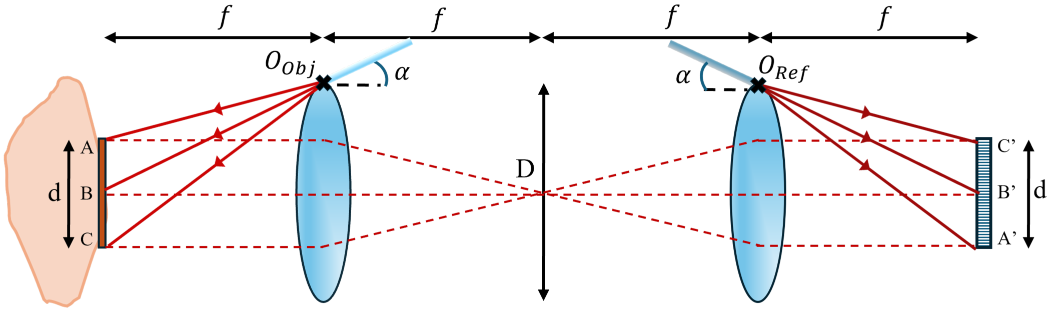

Figure 4.10: Diagram of common-path design with misaligned fibres, with object fibre at same side of adapter as reference fibre.

In this case the lengths of the object path are reversed, such that when expressed in terms of reference path lengths, we obtain;

$$\begin{aligned} l_A &= l'_C \\ l_B &= l'_B \\ l_C &= l'_A \end{aligned} \tag{4.13}$$

Making the substitution into terms of reference path lengths, as given in (4.11), and completing the OPD, we obtain:

$$\begin{aligned} OPD(A') &= l'_C - l'_A = -0.2542\,mm \\ OPD(B') &= l'_B - l'_B = 0\,mm \\ OPD(C') &= l'_A - l'_C = 0.2542\,mm \end{aligned} \tag{4.14}$$

This in theory creates a tilted OPD along the bundle face, with an OPD from A' to C' of $\Delta OPD = 0.5084\,mm$. Completing the calculation based on ΔOPD we obtain:

$$\theta = \arctan\left(\frac{0.5084\,mm}{1.05\,mm}\right) = 25.84^\circ \tag{4.15}$$

4.4 System set-up

The full system set-up is given in Fig. 4.11, which for illustrative purposes is split into distal and proximal parts. The two illuminating fibres take light from the proximal to the distal part, while the superimposed object and reference fields are returned from the distal to proximal part via the fibre bundle.

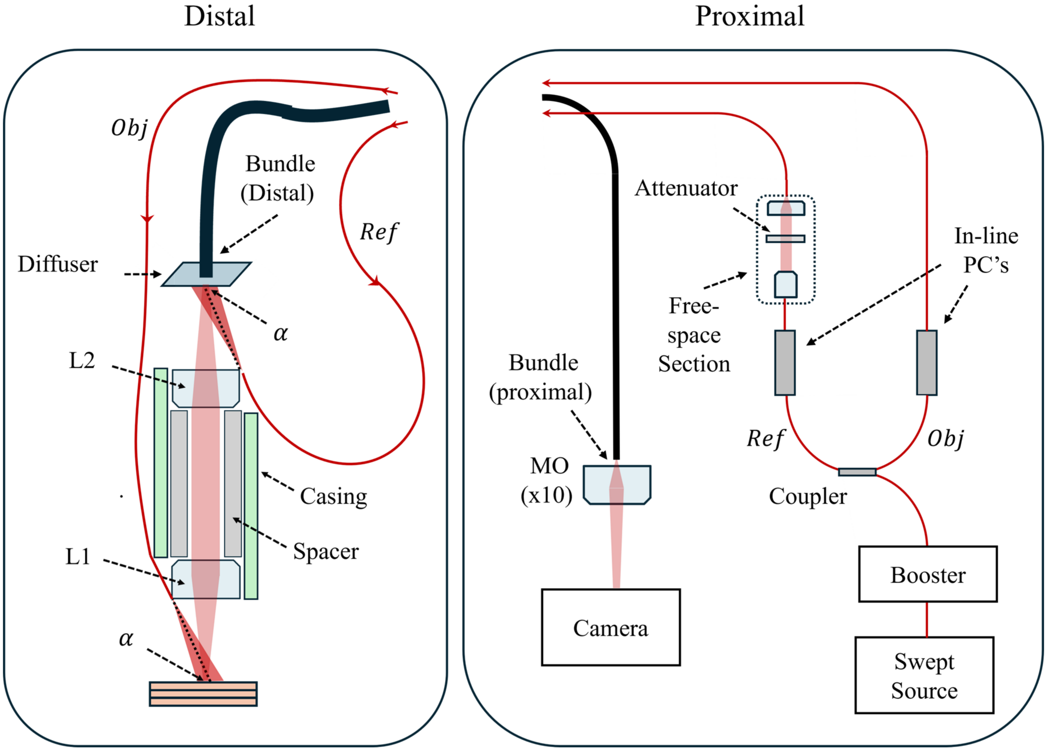

(a) (b)

Figure 4.11: Illustration of complete system set-up; split into (a) distal components, and (b) proximal components. PC: Polarization controller.

Light from our swept source (Superlum BroadSweeper-840 BS0002), is first amplified through a booster (Superlum BB-840-HP-OEM), from 5 mW to 35 mW. The source is connected to the booster with an especially designed 1m patchcord, also from Superlum. The boosted light is delivered to a 99/1 ratio fibre couple

(AFW Technologies - FOSC-2-840-01-L-1-2). The output ports of the coupler are the object (*Obj*) and reference (*Ref*) fibres, which deliver light to the adapter for the object and reference beams respectively. From the object fibre, approximately $15mW$ is delivered to the object, while from the reference fibre, after free-space attenuation, approximate 60 μW is delivered to the bundle. This was found to match the reference image saturation to that of the object.

The superposition of object image and reference fields at the distal face of the bundle is relayed to the proximal end, where it is imaged onto the camera through a microscope objective (MO). Inline polarization controllers (PC's) are positioned in both arms and adjusted to maximize interference contrast. A free space section is included in the reference arm, allowing the reference power and path length to be adjusted. Power in the reference arm is controlled with a variable free space attenuator. The collimator delivering the free-space beam is mounted onto a translation stage to provide adjustment of path length.

4.4.1 Power Optimization

We recall from Chapter 2, that the SNR is maximised when $P_R = P_O$. Therefore at the camera, were interference takes place, we wish to match the reference power to that of the object image. Let us consider the power emitted from the object and reference fibres at the adapter, as this is what we can control, and from the powers emitted the resultant fractions returned to the camera.

We know from our experiment with angled injection of the reference beam, that at 14°, a relatively large fraction of 0.2 is returned to the camera, as given in Fig. 3.13. In comparison, only a very small fraction of the power emitted onto the object is returned to the camera, perhaps due to the relatively small lens NA of 0.25. We estimate that approximately 0.08% of power projected onto the object is returned to the camera.

As such we desired a large coupling ratio, and secured a 99/1 ratio coupler for our system. However, even with 1% power to the reference fibre, the reference image was still oversaturated at the exposure required for half saturation of the object image. To control the reference power, a free space section with a variable attenuator was introduced, and the power emitted from the reference fibre was reduced to approximately 60 μW. At this reference power the object and reference images were both close to half saturation.

To estimate the fraction of object power returned onto the camera, we assume that the object and reference intensities at the camera are equal. The reference fibre delivers a power of 60 μW, of which 0.2 is delivered to the camera, giving approximately 12 μW of reference power at the camera. The object fibre delivers approximately 15 mW to the sample, and by assuming equal intensity at the camera, we estimate 12 μW is delivered to the camera. Hence, the fraction of object power returned to the camera can be estimated as $\frac{12\,\mu W}{15mW} = 0.0008$.

4.4.2 Source Tuning and Image Acquisition

A schematic of the system process for source tuning and image acquisition is given in Fig. 4.12.

A function generator (FG), (Stanford Research Systems - DS345) provides the tuning voltage to the swept source via a coaxial cable (COAX). The tuning voltage is in the form of a saw-tooth function, with a periodicity, phase and amplitude all controlled from the FG. The tuning frequency was set to 0.5 Hz.

A Transistor-Transistor Logic (TTL) trigger, synchronised with the tuning voltage, is sent to the frame grabber (Native Instruments - NI PCIe-1429). With each received 'on' switch of the TTL, a signal is sent through a camera link (CL) cable from the frame grabber to the the camera, triggering a burst of exposures of a pre specified length, $N = 800$. With each exposure within the burst, the captured image is relayed to the frame grabber in real time, and streamed into a LabView virtual instrument (VI) for real time acquisition and processing.

The camera is set at a speed of 400 fps, with [800x800] size

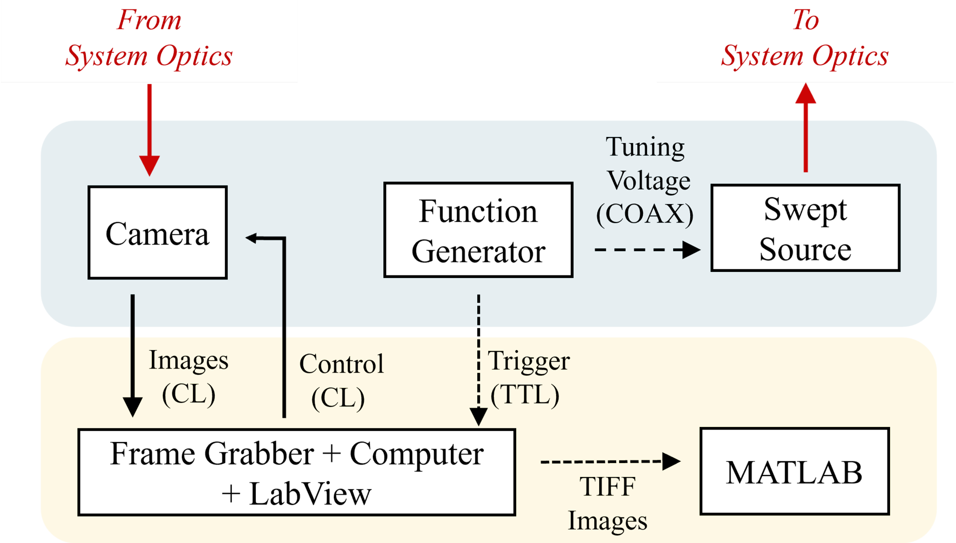

Figure 4.12: Schematic of the source tuning and image acquisition aspects of the system, with analogue processes in blue block and digital processes in yellow block.

images. Hence at the tuning speed of 2 Hz, 800 frames are captured with each tuning cycle of the source.

LabView and MATLAB

In the LabView VI there are two main sections, an acquisition component and a processing component. Within each tuning cycle of the source, the images streamed from the camera are enqueued into an array. Once the array has reached the pre-specified number of images, N, the enqueuing is stopped and the stack of images are input into the processing loop. The processing loop principally exports each image as a 'Tagged Image File Format' (TIFF), creating a stack of TIFF images which can then be imported into MATLAB for post-processing into OCT images. In principle, OCT images could be produced within LabView in real-time, however MATLAB was preferred for implementation and testing of different image processing methods.

FFT Processing.

The raw TIFF images imported into MATLAB are extracted as double precision arrays for processing. The most basic procedure for producing a volume is by taking a 1D Fast Fourier Transform (FFT) along the spectral direction for each spatial pixel in the stack of images.

4.5 OPD Tilt Experiment

To test our hypothesis of OPD matching by co-angled beams, we perform OCT onto the phantom with the object fibre positioned firstly at the the incorrect position, as in Fig.4.10, and then in the correct position, as in Fig.4.8. Stacks of $N = 800$, of images size $[800, 800]$, were obtained and imported to Matlab.

In MATLAB the images are rotated by 43°, aligning the angle of the titled reference beam along the horizontal. An FFT is performed on both stacks, and the resultant OCT volumes smoothed with a Gaussian filter. B-scans were selected from a region across the metal plate with no holes, in order to demonstrate the apparent OPD tilt of the sample. The B-scans are cropped to the central 550 lateral pixels and 65 axial points in depth, covering the region spanned by the apparent OPD tilt. The cropped B-Scan for either case are given in Fig.4.13.

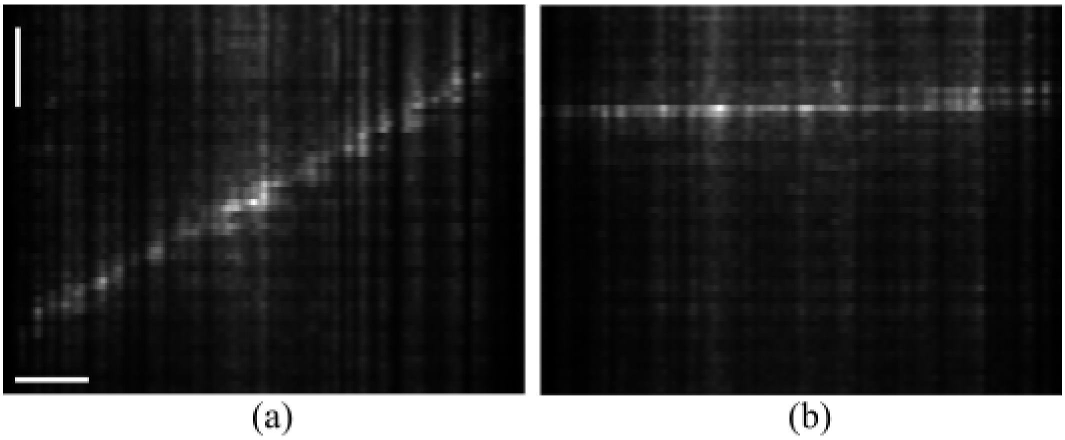
(a) (b)

Figure 4.13: B-scans demonstrating the apparent OPD of the object, for (a) misaligned case, and (b) co-aligned case. Scale bars are 100 μm in both lateral and axial directions.

In the mismatched case, (a), the object is tilted. The OPD across 0.3 mm of the object was measured to be 0.63 mm, giving an apparent angle tilt of $\theta \approx 25.46°$, approximately matching the expected tilt of $\theta = 25.84°$.

There is also a slight apparent tilt of the object in the correctly aligned case, (b), which was measured at $\theta = 1.6°$. This suggests that the fibres were not exactly co-aligned when the experiment was performed.

No background subtraction or averaging was performed in this experimentation. In the following chapter we demonstrate the full processing pipeline for producing OCT images either by a windowed FFT or by the CMS method.

Conclusion

In this chapter, we have detailed the design and experimentally validated a forward-viewing fibre bundle OCT adapter, implementing angled divergent illumination for both object and reference paths, achieving superposition directly at the distal bundle face without requiring a beamsplitter.

Through comparing potential distal optics, we selected a 4f configuration, for its superior field flatness and improved handling of off-axis illumination. A calibration phantom was used to measure the adapter's magnification, while a USAF target was used to characterize lateral resolution. Gaussian smoothing was found to effectively remove the core pattern without sacrificing resolution. The lateral resolution, when using the diffuser and after smoothing was found to be approximately 50 μm.

Geometric modelling of the optical path length variation across the bundle face highlighted the sensitivity of the design to angular misalignment of the object and reference fibres. Our experimental OPD tilt test validated this theory, with the measured tilt in the misaligned case closely matching the expected value of $\sim 26°$. A small residual tilt was also apparent in the co-aligned case, indicating the sensitivity to correct alignment. In practice, any misaligned angle and the apparent OPD tilt would be fixed, and hence it would in theory be possible to artificially correct in post processing, returning a true representation of the object orientation.

Chapter 5

OCT Results and Image Processing Methods

5.1 Introduction

In this chapter we produce OCT images of our phantom, demonstrating the OCT performance of the adapter. Quantitative metrics are used to analyse images and compare them with those acquired from a bench-top ‘in-bulk’ OCT system.

Images are first produced by the FFT approach. We then explore the practicality of employing the CMS processing method, and present solutions to the difficulties faced in this approach.

5.2 Phantom design

We take the phantom used for image calibration in Chapter 4, and adapt it so as to give it depth resolvable features. We applied layers of clear polymer tape directly underneath the metal plate. In this way, light can be scattered from the tape at regions directly underneath the holes, and is occluded under solid regions of the plate.

To understand the structure of phantom, before attempting

OCT with our system, we first acquired an OCT volume using a bench-top point-scanning SS-OCT system, centred at 1300 *nm*. The phantom is mounted in air, i.e. with only air directly underneath the bottom layer of tape.

Volumes were acquired over a FOV of 1 *mm* by 1 *mm*, with a depth of 5 *mm*. A B-scan across the centre of the object was extracted, across a region with holes, such that the layers of polymer tape are seen in the B-scan, as shown in Fig. 5.1. In the axial direction, each pixel represents 10 μm, while in the lateral direction each pixel represents $2 \mu m$. The B-Scan shown in Fig. 5.1 is cropped to a width of 0.57 *mm*, and a depth of 1.07 *mm*.

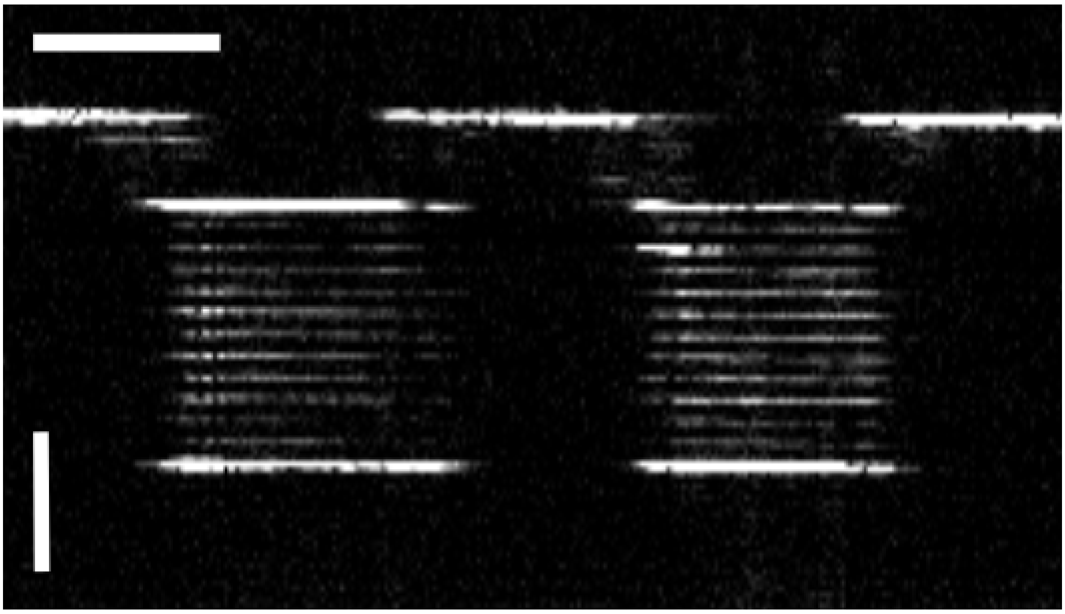

Figure 5.1: B-Scan across holes of the phantom, obtained from a bench top SS-OCT system, with 100 μm lateral scale bar and 250 μm axial scale bar.

Measurements of the phantom were then taken from the B-scan. The metal plate was found to have a thickness of $160\,\mu m$, while the polymer layers were found to be 460 μm thick, making for a total phantom thickness of 620 μm. This was in agreement with the thickness measured with callipers, which was $\approx 0.6\,mm$. The SNR retuned from the metal plate was measured, taking the standard deviation of the last 50 points in the A-scan as the value for noise, coming to an SNR of 39.48 dB.

5.3 OCT by FFT method

Let us now perform OCT onto the phantom with our adapter. We first produce OCT images using an FFT approach. Stacks of length $N = 800$, with images of size 800 by 800 pixels, are collected across a single tuning cycle. We first obtained a 'signal' stack, i.e. a stack of images across a single sweep, in which the adapter has both object and reference beams active. We then obtain two additional stacks, an 'object' and a 'reference' stack, in which power is removed from each arm in turn. The object and reference stacks are used for background subtractions. Performing a background subtraction is crucial for improving the SNR in our system, considering we cannot perform a balanced detection with our design. In general background subtraction is difficult in FF-OCT, as it requires two cameras, and in our case it is not at all possible as both arms must be superimposed onto the bundle.

Images are first cropped to a 600x600 pixel region about the centre of the image. We have cropped to this region because in performing the acquisition, the reference and object fibres were brought closer to the sample/bundle. This had the effect of increasing intensity over the central region, at the loss of some FOV.

The mean images across each stack are shown in Fig. 5.2, where a single image was produced for each stack by averaging over all 800 images.

Exposure optimization

As we saw in the previous chapter, there exists a sporadic and large fluctuation of intensities between cores, in both the object and reference stacks. This is particularly apparent in the object

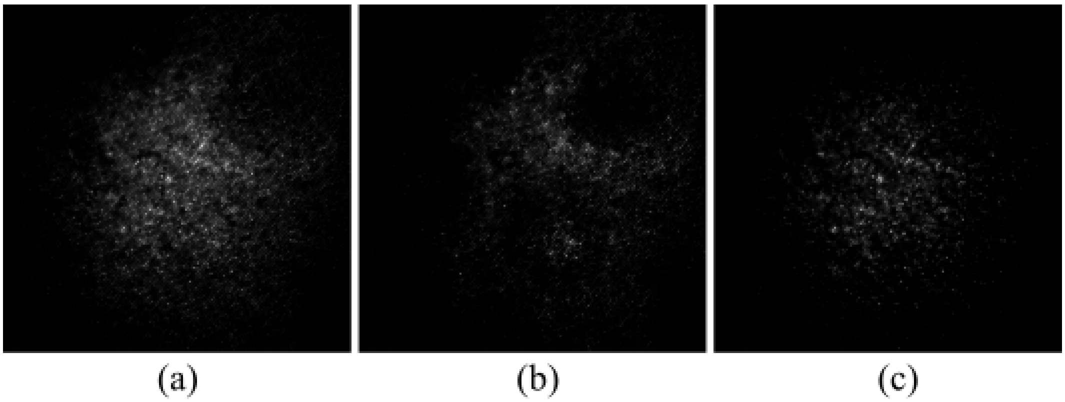

Figure 5.2: Average image from each of the acquired image stacks; (a) signal stack with both arms superimposed, (b) object stack with reference arm blocked, and (c) reference stack with object arm blocked.

images, whereby the intensities across cores range from practically no intensity to being oversaturated.

The exposure must therefore be kept sufficiently low as to avoid having lots of oversaturated pixels, as these would lead to saturation streaks along depth in the resultant FFT stack. To prevent these, we must sacrifice intensity, reducing our attainable SNR in order to prevent an overwhelming number of saturation streaks.

The averaged images are shown again in Fig. 5.3, this time with a contrast adjustment applied, such that the brightest pixels are represented as saturated. In these images we clearly see the large fluctuations of intensities, and a large number of saturated pixels. This explains why the raw stacks, Fig. 5.2, are necessarily dim.

Before continuing with processing, for each stack, we computed and plotted the average intensity of each frame. These are given in Fig. 5.4. We see that each stack represents a Gaussian spectrum, as expected. We also see that the object and reference intensities are well-matched. However, there is a large discrepancy between the signal intensity and the sum of reference and object intensities. This is most likely due to an automatic adjustment of intensities performed by the camera.

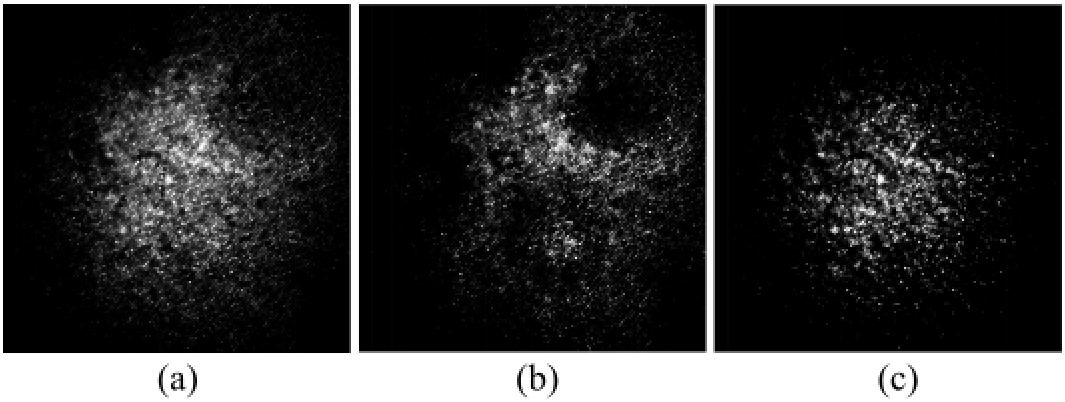
(a) (b) (c)

Figure 5.3: Averaged images with contrast mapping applied, demonstrating the sporadic pattern of oversaturated and dim pixels.

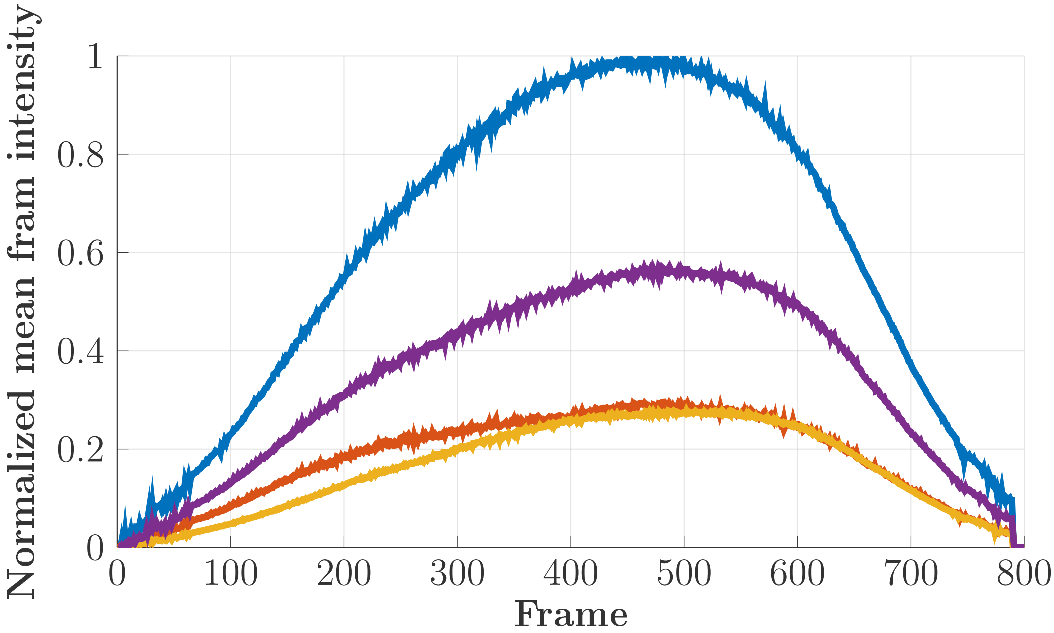

Figure 5.4: Average intensity of frame vs frame number for each stack: signal stack (blue), object stack (orange), reference stack (yellow), and sum of object and reference stacks (purple).

Windowed FFT and Gaussian smoothing

Each stack is windowed using a Hamming filter (MATLAB - hamming). By default, the MATLAB hamming window has values ranging from approximately 0.08 (at the edges) to a peak amplitude of 1 (at the centre). When applied, the centre of the stack retains full intensity, while the edges are tapered down smoothly to avoid spectral leakage or edge artefacts. We changed the amplitude of the Hamming filter to 0.8, which ensured minimal intensity clipping, whilst still securing the desired spectral shaping.

A 1D FFT is then applied along the spectral direction of each pixel, producing three windowed FFT stacks. An absolute operation is then performed on each of the three windowed FFT stacks, returning arrays of real values. After taking the absolute, a background subtraction is then performed, whereby the object and reference absolute valued FFT stacks are subtracted from the absolute valued FFT signal stack. After the subtraction, all values ≤ 0 are set to zero. A Gaussian smoothing filter of size 10 pixels (13.7 μm) is then applied to each frame of the subtracted stack to remove the core pattern.

We then perform an average en-face subtraction. Here, a single en-face image is produced by averaging all en-face frames. The averaged frame is then subtracted from each en-face frame, removing any fixed pattern noise common across all depths.

Depth Calibration

To perform a calibration of depth, OCT volumes were obtained at differing OPD, by increasing the length of the free space section of the reference arm. Stacks were obtained at increments of 500 μm OPD. A-scans were plotted for all three depths and the average distances from the start of each A-scan peak was measured. An OPD of 500 μm was found to span 31 axial pixels, therefore in terms of OPD, each axial pixel, d_{OPD}, represents an interval of;

$$d_{OPD} = 16.13\,\mu m \tag{5.1}$$

In terms of depth, our axial pixel size is halved, giving us a true depth interval, dz, of;

$$dz = 8.06\,\mu m \tag{5.2}$$

B-Scan and En-face Averaging

To improve SNR, averaging is performed in two axis, generating two averaged stacks; by averaging over B-scans in the horizontal direction and over en-face frames in depth. For B-scan averaging, every 10 B-scans are averaged, producing a resultant stack with 60 B-scans. Similarly, every 10 en-face images are averaged, generating an averaged en-face stack with 80 frames. We recall that in FF-SS-OCT, half of the frames in the FFT stack represent the conjugate signal mirror terms of the FFT operation, and hence the actual number of en-face images is 40.

5.3.1 B-Scans

Selected averaged B-Scans, taken at a region across a hole, and a region with no holes, are shown in Fig. 5.5 and Fig. 5.6 respectively. Images are shown across 500 lateral pixels, equalling a width of 0.683 mm, while in depth, the images are shown along 0.8 mm.

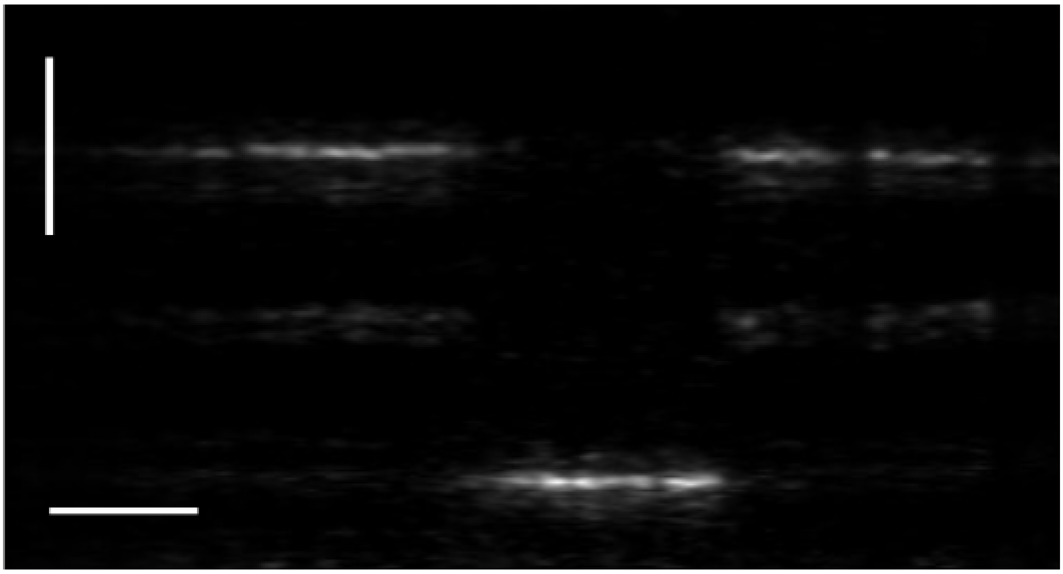

Figure 5.5: B-scan of phantom across region featuring holes, with 100 μm lateral scale bar and 250 μm axial scale bar.

We see two distinct bands. The top band clearly represents the metal plate, as it features a hole. The second band corresponds to the bottom surface of the layers of polymer tape. We interpret this as where dirt has adhered to the bottom of the tape, from which light is scattered with sufficient intensity to be imaged. In our B-scan, the layers of tape have not been resolved, meaning our sensitivity was too low to resolve reflections at the boundary of layers of tape. Hence, to demonstrate OCT imaging from a scattering object, we have relied upon off-axis scattering of light from dirt at the bottom of the layers of tape.

In the B-scan from the bench-top system, Fig. 5.1, the top and bottom surfaces of the layers of tape are of a similar brightness, whereas in our B-scan the top surface of the layers of tape is not even resolved, while the bottom layer is of a similar brightness to the metal plate. The distinction perhaps comes from the difference between on-axis backscattering in the bench-top case, vs the off-axis scattering in our system.

Measurements

The distance between bands is measured at 74 pixels, equalling a thickness of 76 * 8.065 $\mu m = 612.94\ \mu m$. There is slight discrepancy from the length measured in the OCT images obtained from the bench-top system of 620 μm, however, this is likely due to the inaccuracy in measuring the positions of each band.

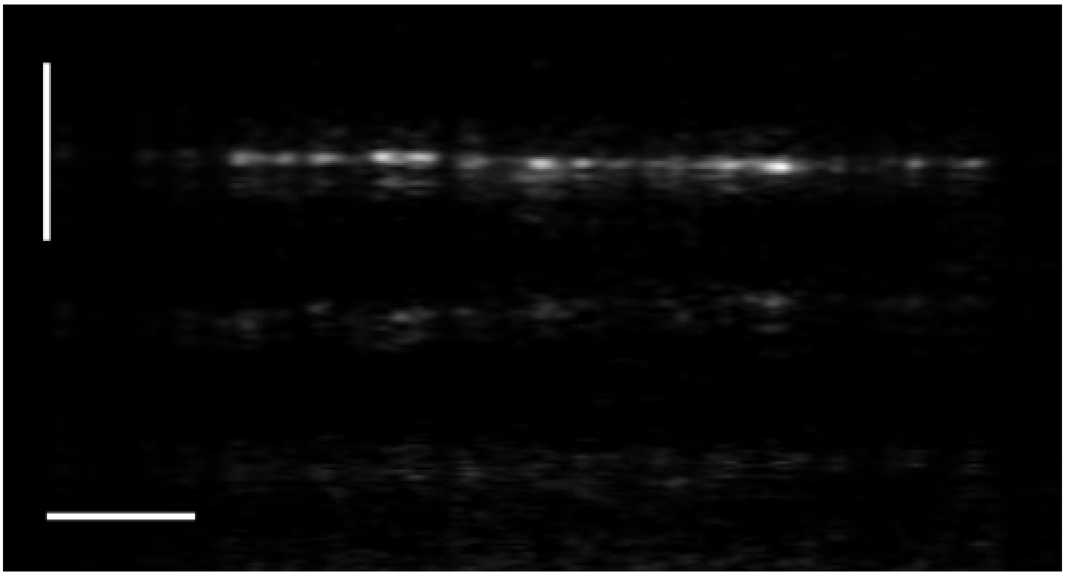

Figure 5.6: B-scan across region with no holes, with 100 μm lateral scale bar and 250 μm axial scale bar.

We also present a B-scan from a region with no holes, Fig. 5.6 demonstrating the case when the under-layers are occluded.

Multiple reflections

The second B-scan corroborates a feature apparent in both B-scans, which is a faint band approximately 0.2 mm below the band produced from the metal plate. We can conclude this considering that it appears at the same depth in both B-scans, and in both resembles the metal plate i.e with a hole in the first and continuous in the second. This is interpreted as a multiple reflection signal, perhaps from the cover slip of the camera sensor.

5.3.2 En-face images

Selected en-face images were extracted at cross-sections along the metal plate and the polymer layer, which are shown in Fig. 5.7 and Fig. 5.8 respectively.

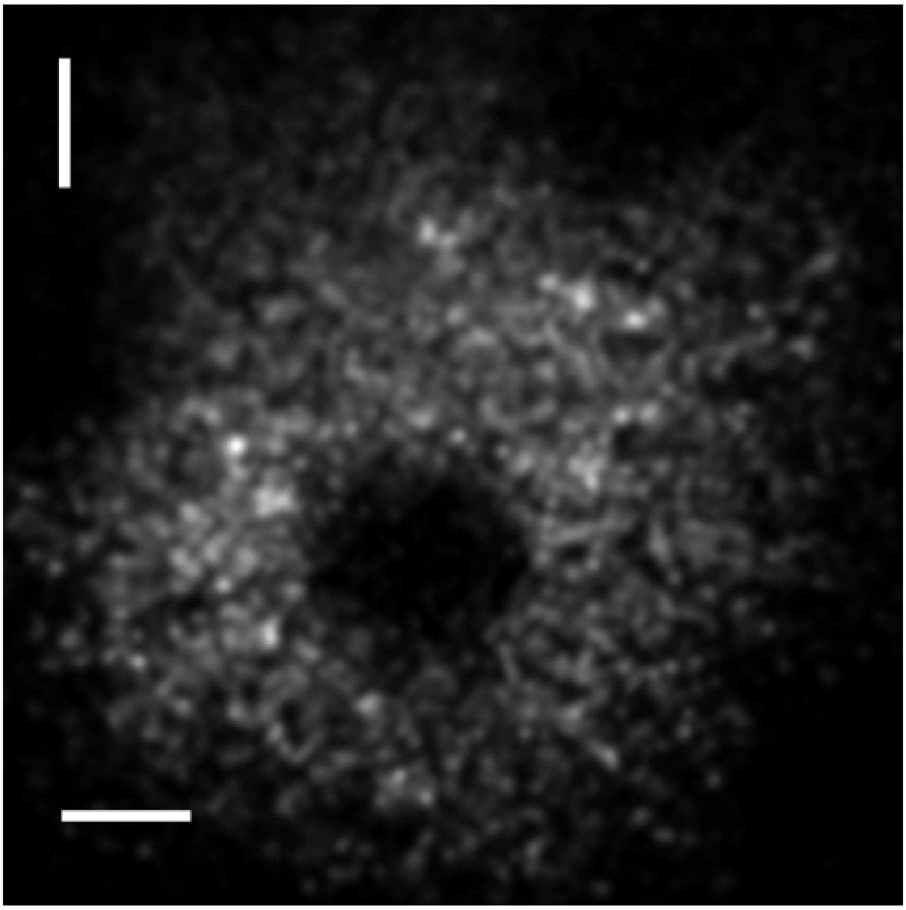

Figure 5.7: Selected en-face frame across hole region of metal plate, with 100 μm scale bars in x and y directions.

We clearly see the distinction between the two images, the first representing the metal plate and the second representing the polymer tape. We see that the images feature a pattern of intensities resembling a speckle pattern, as was apparent in the independent object and reference images. We see that the pattern of differing intensities is too large to have been smoothed by the Gaussian filter.

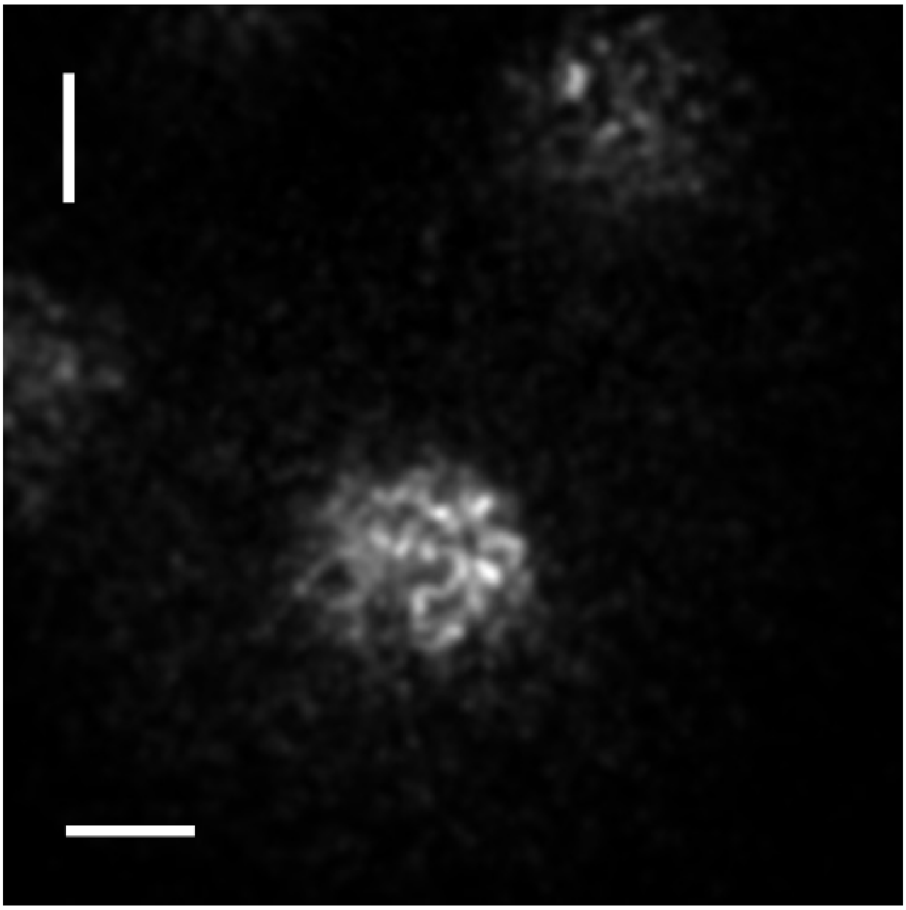

Figure 5.8: Select en-face frame across polymer layer, visible below holes of metal plate, with 100 μm scale bars in x and y directions.

5.3.3 SNR

We have established that our sensitivity was not capable of resolving the polymer layers of tape, and we should establish the SNR of the system to understand what could be resolved with our current sensitivity.

To measure the SNR, OPD was adjusted such that the signal returned from the plate was below the zero OPD, just clear of the DC lobe. The signal amplitude was taken as the maximum value of the A-scan peak returned from the metal plate, while the noise was calculated by taking the standard deviation of the last 50 points in the A-scan. These were taken after subtraction, without setting all the values ≤ 0 to 0, or performing averaging of en-face or B-scans. The experimentally measured value of SNR was:

$$SNR = 32\,dB \tag{5.3}$$

5.3.4 Signal drop off

We next measured the drop-off of signal amplitude vs OPD, by adjusting the path length in the reference free space section and acquiring a signal stack at different OPD. Values of amplitude were normalised to the amplitude at close to zero OPD, i.e. at OPD with an SNR of 32 dB.

We observe an expected drop-off of amplitude with depth. The -3dB OPD was found to be 1.66 mm. We can attribute some of this drop in amplitude to the instantaneous coherence envelop. With a tuning range of $47\,nm$, sampled with $M = 800$ spectral points, the effective linewidth is, $\delta\lambda = 0.0588$. With a central wavelength of $849.5\,nm$ we can estimate the -3dB length of instantaneous coherence curve as:

$$z_{-3dB} = \frac{\ln 2}{\pi} \cdot \frac{(849.5\,nm)^2}{0.0588} = 2.71\,mm \tag{5.4}$$

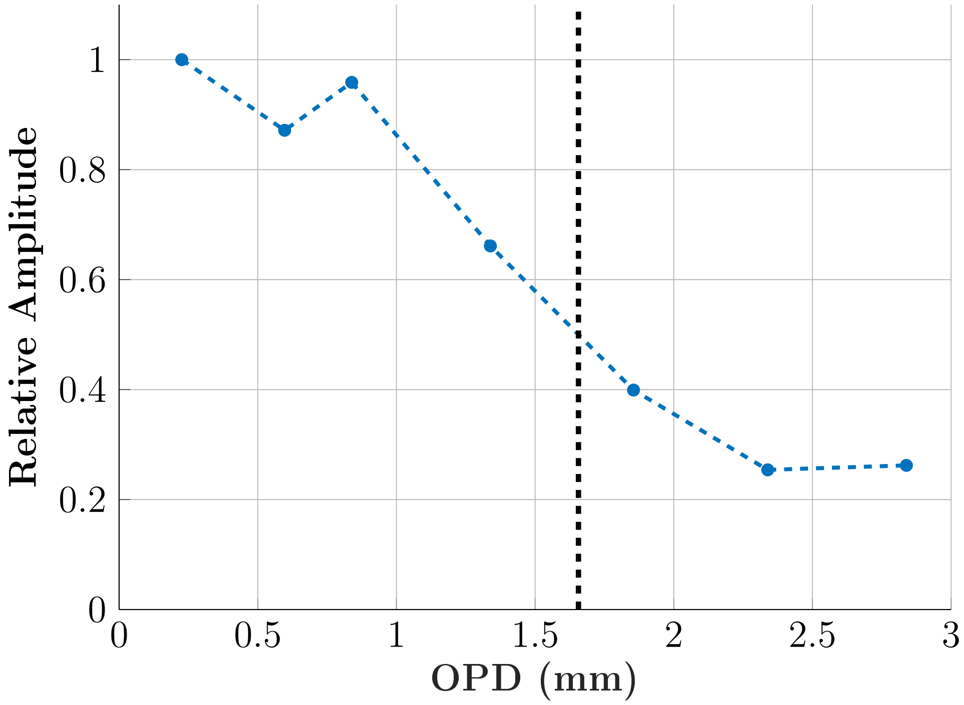

Figure 5.9: Roll-off of signal amplitude vs OPD (blue dashed line), with a -3dB OPD of 1.66 mm (black dashed line).

5.3.5 Axial resolution vs OPD

The same data set of stacks with varying OPD was used to produce a graph of axial resolution vs OPD. The A-scan was inspected at a pixel over the metal plate, with MATLAB's peak finding function used to obtain the position of each peak. The FWHM of each peak was then measured to obtain the axial resolution.

To improve the accuracy of the FWHM measurement, a linear interpolation was applied to the region about the peak. The intensity values in the selected range were resampled using MATLAB's interp1 function with the 'linear' method. This generated a set of 1000 interpolated data points across the interval. The FWHM was then found by locating the two interpolated positions at which the signal crossed the half-maximum level. The measured values of axial resolution vs OPD are given in Fig. 5.10.

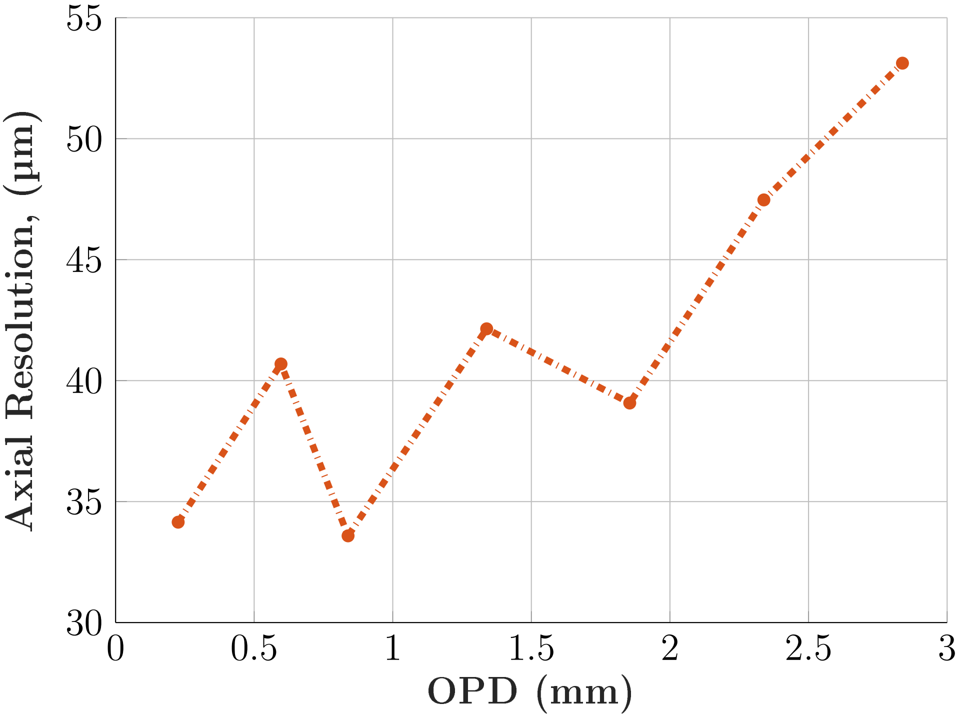

Figure 5.10: Broadening of axial resolution with OPD.

We observe a general broadening of axial resolution along OPD, although the resolution was found to oscillate along OPD, with the greatest axial resolution actually at an OPD of 0.84 mm. At close to zero, we achieved an axial resolution of;

$$\delta z_{OPD\approx 0} = 34.15\,\mu m \tag{5.5}$$

While the greatest axial resolution at OPD of 0.84 mm was;

$$\delta z_{best} = 33.58\,\mu m \tag{5.6}$$

This is somewhat better than our lateral resolution, which is 49.7 μm. However, as we go into depth, the axial resolution degrades to a similar order. At the -3 dB depth we obtain an axial resolution of approximately 40 μm.

We can compare our measured axial resolution to a simple theoretical calculation. With a tuning range of 47 nm, at a central wavelength of 849.5 nm, the expected axial resolution in SS-OCT, in air, without any degradation from practical effects, is given by:

$$\delta z = 0.6 \cdot \frac{(849.5\,nm)^2}{47\,nm} = 9.21\mu m \tag{5.7}$$

5.4 CMS Method

We next present OCT images of the phantom generated via the CMS method [45]. We capture stacks with both object and reference arms unblocked, at three different OPD. For the first stack, OPD is adjusted such that the FFT A-scan peak is clear from the DC signal. This is taken as the signal stack to be processed into an OCT volume. For the two calibration stacks, OPD was increased in intervals of $250\mu m$ OPD. For the signal stack, the average image over all frames was calculated, and is shown in Fig. 5.11, with an image size of 600x600 pixels, equalling a FOV of 0.82 mm by 0.82 mm. The pixel used to extract channelled spectrum (CS), for the purpose of measuring the g and h functions and generating masks, is circled in blue.

5.4.1 Creating Masks

Typically, masks are created from calibration spectra obtained from a mirror in the object arm. However, given the geometry of the adapter, it was difficult to place a mirror into the correct position that could be tilted at the right angle, and so we abandoned the attempt of using a specular calibration target. We instead investigated using the phantom as the reflector for obtaining calibration spectra.

A mirror is typically used, as the calibration spectra must represent a ‘clean’ CS, approximately resembling a singular modulation. However, the CS obtained from the phantom, at the selected pixel with co-ordinates, y = 432 and x = 391, shown in Fig. 5.12, had several modulations, as seen in the FFT from the selected pixel given in Fig. 5.13

Two potential causes of these could be; self interference in the object field from different scattering points along the object, or, an effect of higher order modal coupling of the reference field into the bundle. For instance, with regards to core injection of the reference field, when tuning over k, the mode profiles of each core

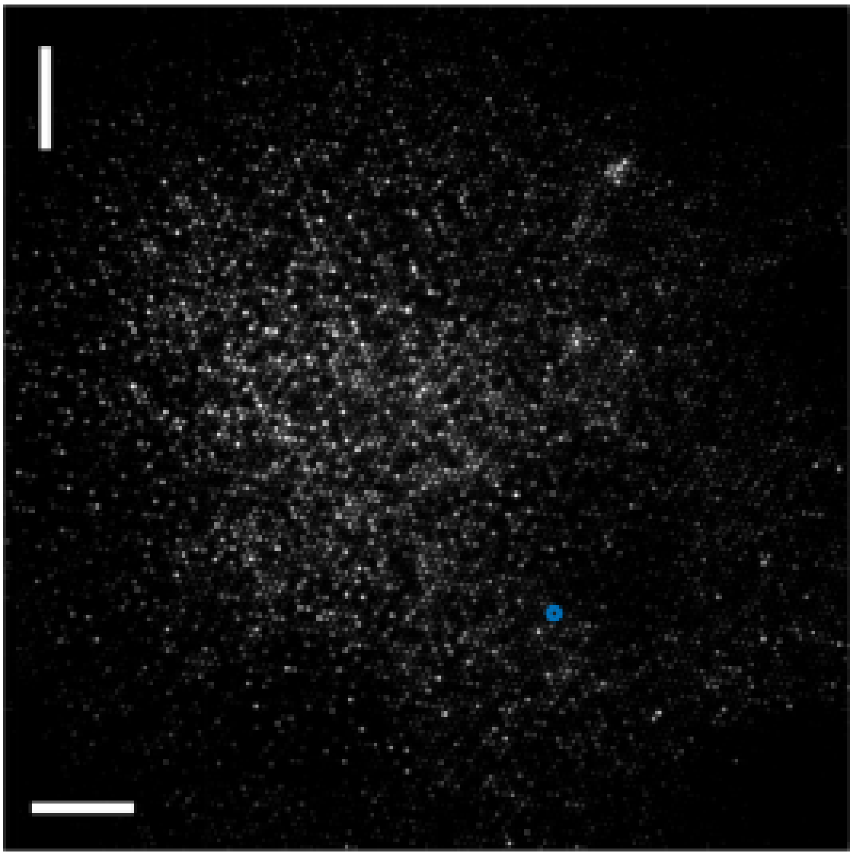

Figure 5.11: Average image across all frames of signal stack, with pixel used to extract CS circled in blue.

rotate. This induces a low frequency modulation along k at each pixel. Owing to the different shapes of the mode profiles, and their different rotational frequencies, differing modulations are induced at different pixels, both between cores, and at pixels over a single core.

The A-scan from the signal stack, at the selected pixel, is shown in Fig. 5.13, over a range of 1 mm of OPD, with amplitude normalised to the DC value.

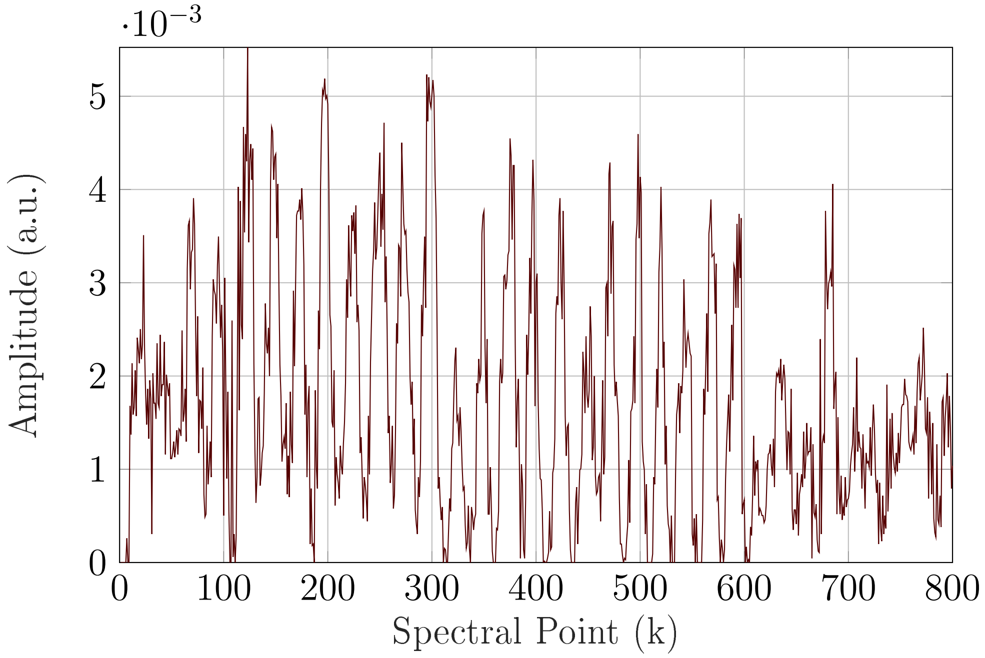

Figure 5.12: CS from selected pixel (y = 432, x = 391)

Bandpass filtering

To clean the calibration spectra we use a bandpass filter (MATLAB's `fpass` function).

We first locate a suitable pixel from which to extract the spectra. This is done by first taking an FFT over the signal stack. We then locate the position of local maxima for each pixel's A-scan, using a peak-finder function (MATLAB - `findpeaks`), which locates local maxima by amplitude. We then compute the SNR of the A-scan at each pixel, and select the pixel having the highest SNR A-scan. This selected the pixel at y = 432 and x = 391, as plotted with a blue circle in Fig. 5.11. CS are extracted from each of the three stacks at the selected pixel.

We then apply the fpass filter onto the set of 3 CS, manually adjusting the frequency limits to obtain an approximately singular modulation. The CS and the FFT A-scan from the signal stack, i.e. the first calibration depth, before and after applying the bandpass

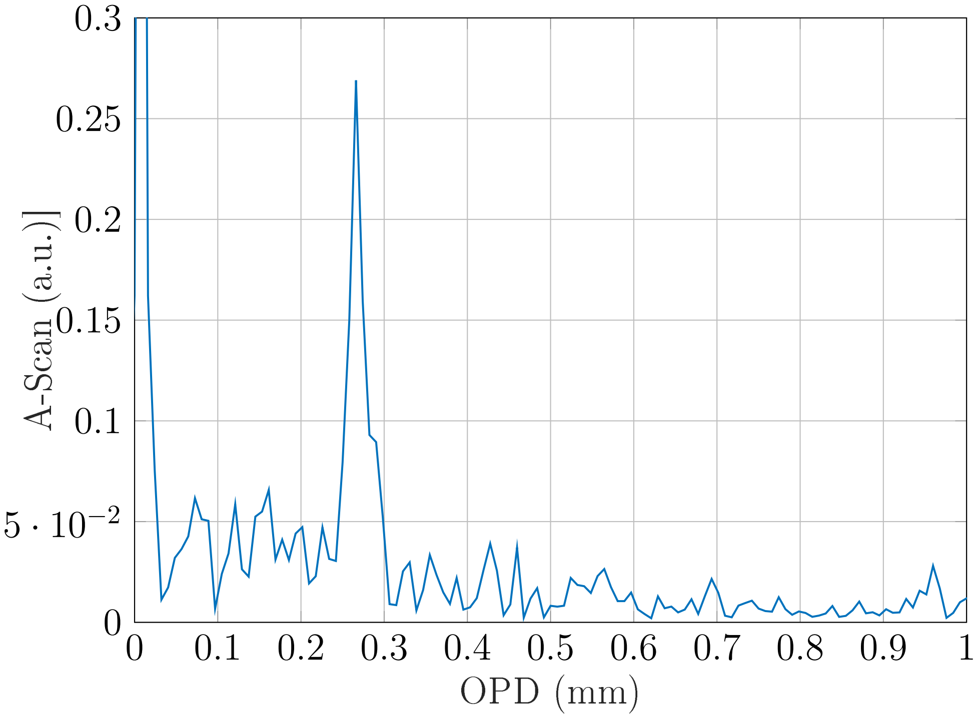

Figure 5.13: A-scan from selected pixel (y = 432, x = 391)

filter, are shown in Fig. 5.14, where, the top row shows the CS and FFT without filtering, and the bottom row with filtering.

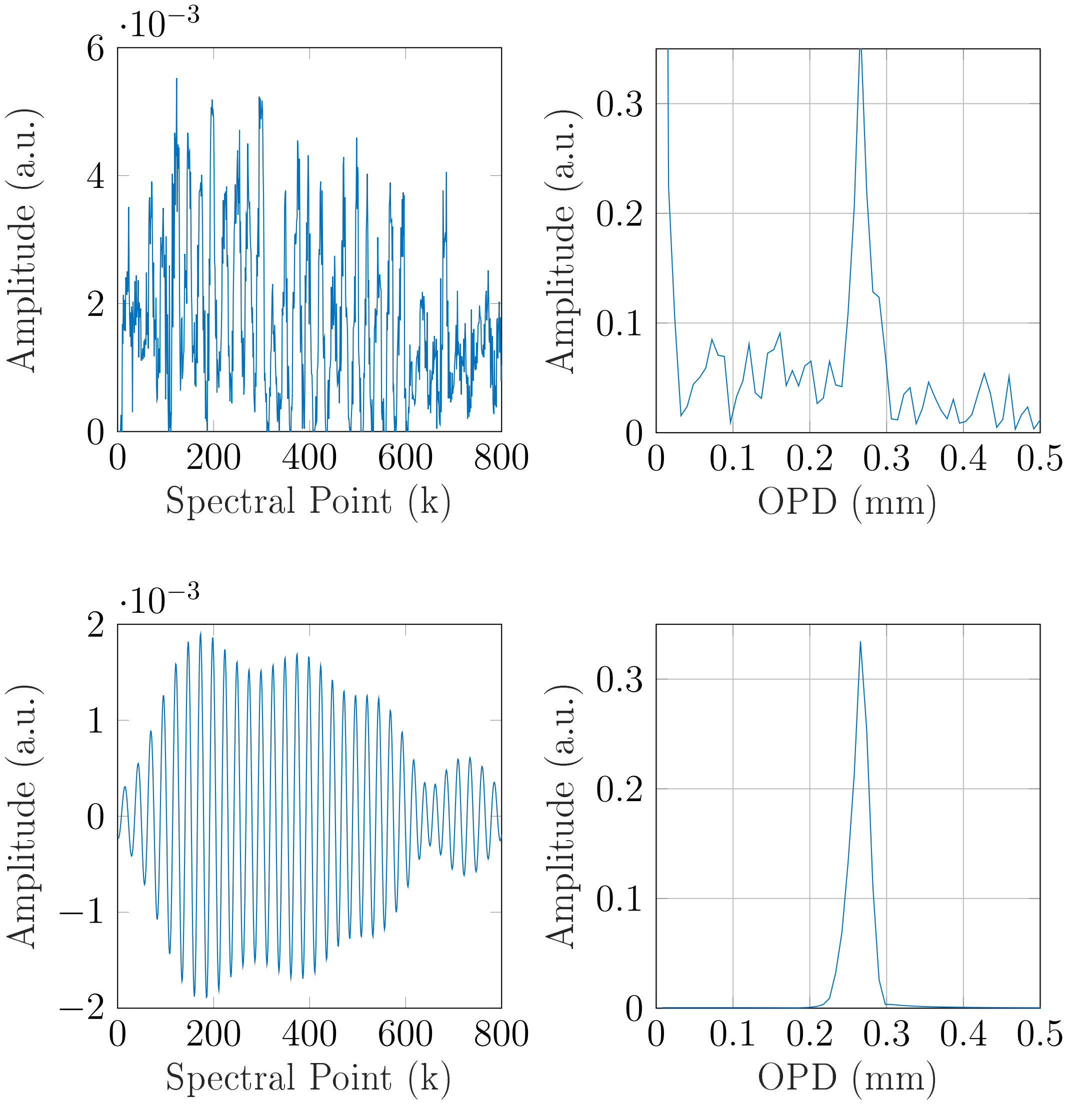

Figure 5.14: Unfiltered and filtered CS and their resultant FFT. Top row: unfiltered CS (left) and its FFT from 0 to 0.5 mm OPD (right). Bottom row: filtered CS (left) and its FFT (right).

The g and h functions

The filtered CS are then used to obtain the functions of g, non-linearity of tuning, and h, system dispersion, which are shown in

Fig. 5.15. We observe the expected approximate linearity of the g function. The h function however shows some unusual behaviour. Typically h is one directional across k, whereas in our case we observe h switching direction.

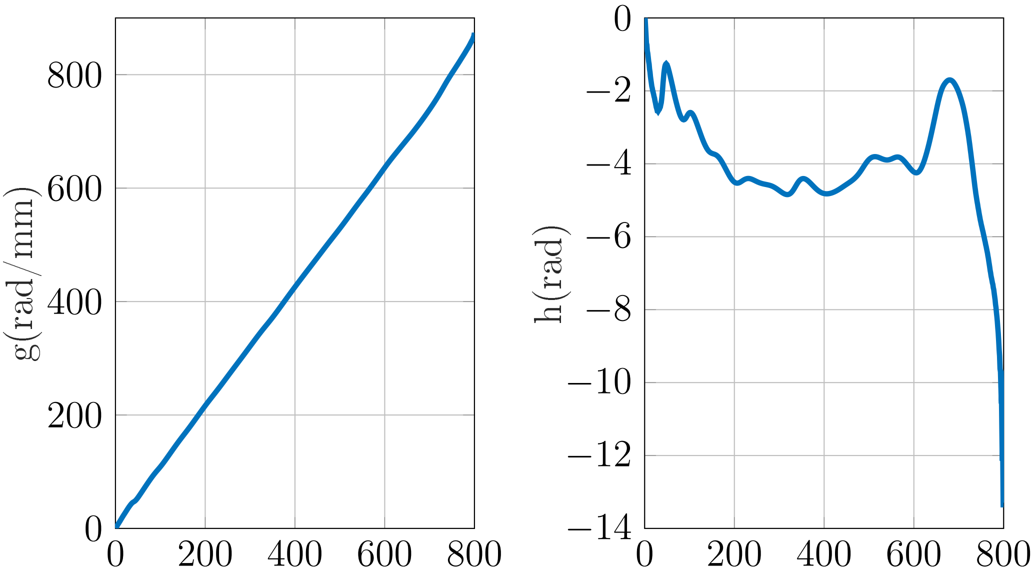

Figure 5.15: The g and h functions obtained from the selected pixel, with g in units of $radians/mm$ (left), and h in units of $radians$ (right).

The g and h functions are then used to synthesise the masks. With the masks acquired we can produce an A-scan from the selected pixel, taking the matrix product of the pixel's CS with the set of masks. The A-scans of all 3 depths are given in Fig. 5.16, normalised to the amplitude at the first depth, in linear (left) and logarithmic (right) scales.

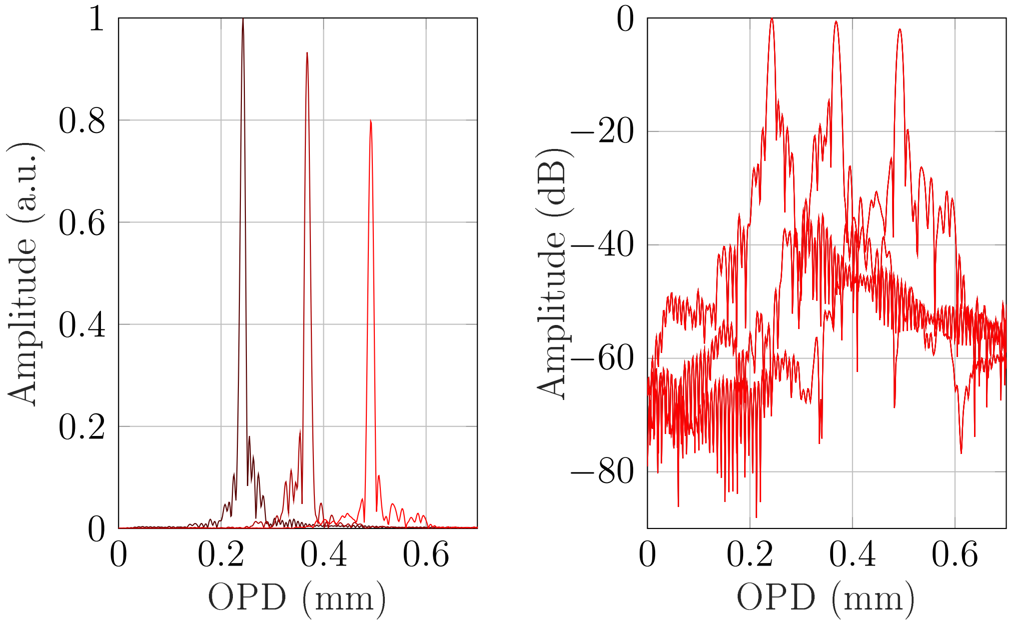

Figure 5.16: CMS A-scan at selected pixel for three different OPD, normalised to amplitude at first depth, in linear scale (left) and logarithmic scale (right).

DC Term

At the time of collecting data sets, the object and reference stacks were not successfully acquired, and hence the method of background subtraction used in the FFT method could not be repeated. Instead, to remove the DC component, we calculated the mean along k for each pixel, and then at each pixel subtracted the mean from the value at each frame. This is performed after measuring the g and h functions and synthesising masks, so as not to affect their measurements.

Matrix Multiplication and Processing

After the DC cleaning step, we perform the matrix multiplication of the cleaned signal stack with the masks. We then apply a Gaussian smoothing filter to all en-face frames in depth, as well as an average en-face subtraction, as was enacted in the FFT method.

5.4.2 B-Scans

As with the presented FFT results, every successive 10 B-scans were averaged, forming a total number of 60 B-Scans.

A B-scan taken from a region across a hole is presented in Fig.5.17, cropped to a width of 0.82 *mm*, and a depth of 0.375 *mm*, with 100 μm axial and lateral scale bars. We notice vertical streaks along the B-Scan. These are perhaps indicative of an ineffective background subtraction, and may potentially be removed with a typical subtraction.

We notice that the signal retuned from the polymer part is returned from the first surface of the polymer, not the lower surface as in the FFT results. The band representing the polymer layer is found at a depth of approximately 0.16 *mm*, matching the thickness of the metal plate

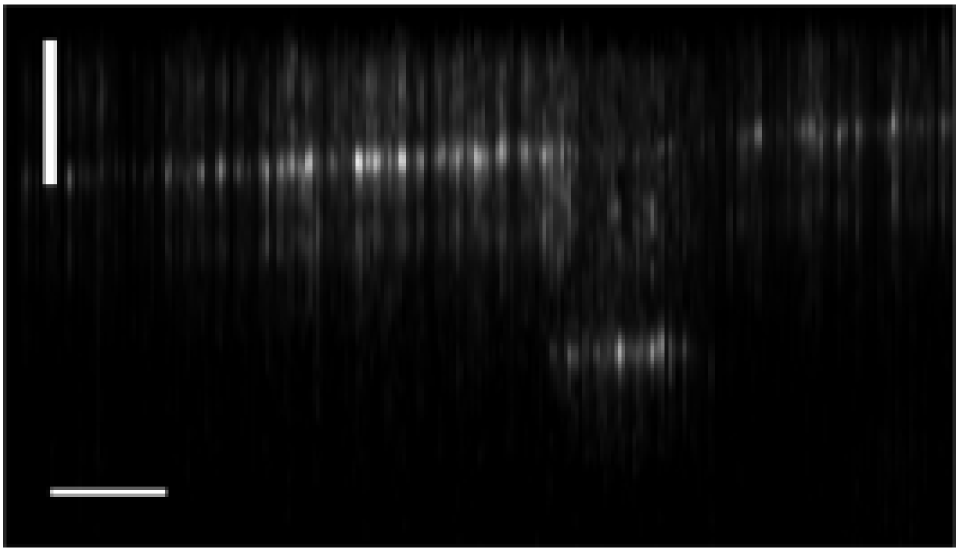

Figure 5.17: CMS B-Scan, across a region with a hole, with 100 μm axial and lateral scale bars.

A B-scan taken from across a solid region of the plate with no holes is presented in Fig.5.18, cropped to the same size with the same length scale bars. Again, we notice vertical streaks along the B-Scan.

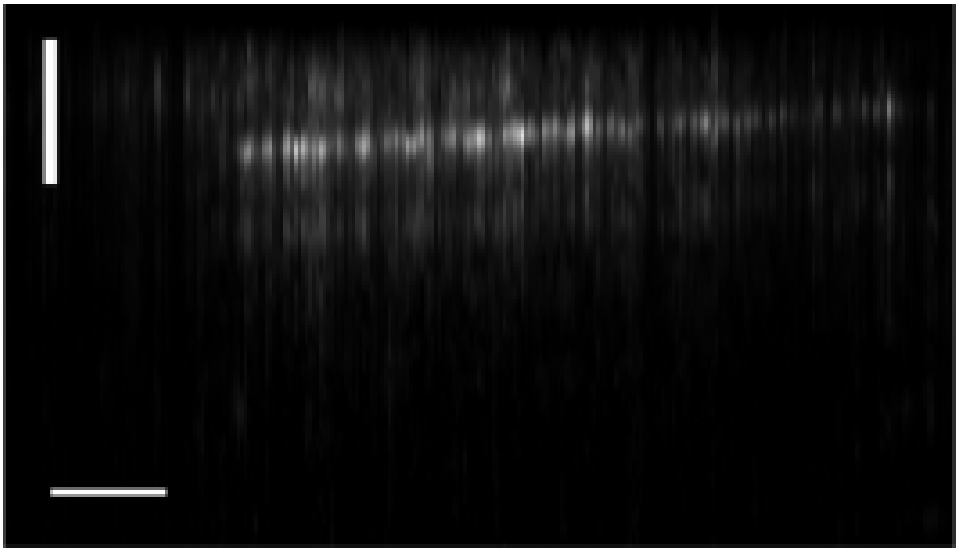

Figure 5.18: CMS B-Scan, across a solid region of the plate, with 100 μm axial and lateral scale bars.

Axial Resolution

The axial resolution at the selected pixel is computed via the same method used in the FFT analysis. The A-scan peak, along with the interpolated signal, and the measured FWHM, are plotted in Fig. 5.19. We obtained a value of:

$$\Delta z = 20.03\,\mu m \tag{5.8}$$

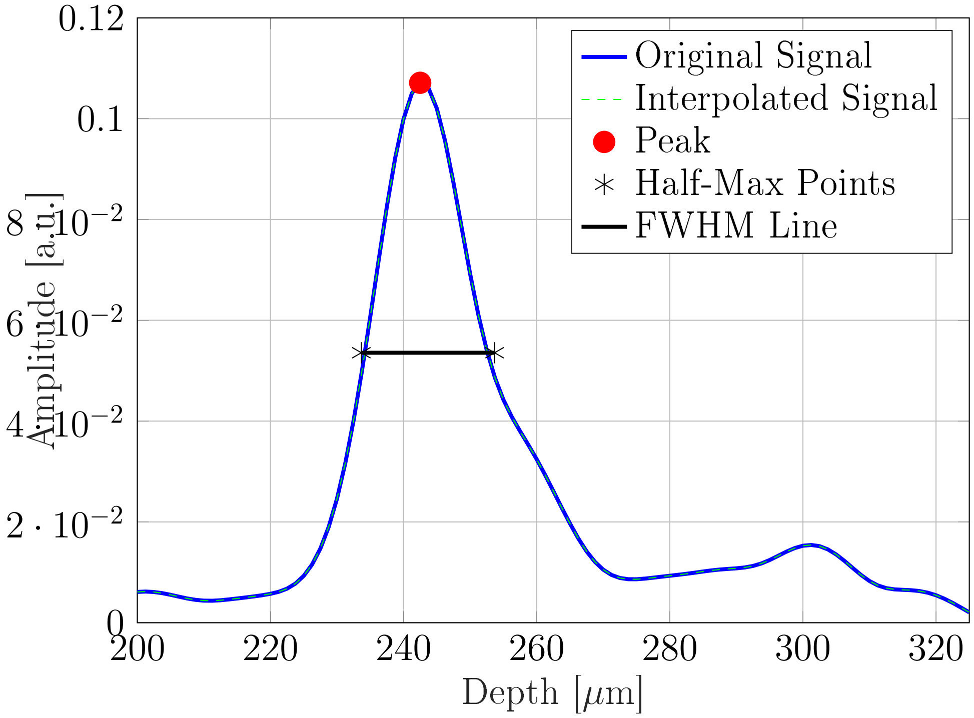

Figure 5.19: Axial resolution of the CMS A-Scan at the selected pixel.

Hence, despite the artefacts present in the CMS B-Scans, we have secured a greater axial resolution than via the FFT approach. We can speculate that if a successful background subtraction could have been performed, we might expect to see better B-scan images from CMS than FFT.

SNR

To attain a value of noise, we calculated the standard deviation between 0.1 mm and 0.16 mm, i.e. in the region just before the plate. We obtained a value of;

$$SNR = 27\, dB \tag{5.9}$$

This is less than the value obtained in the FFT approach, which could be explained by the lack of an effective background subtraction.

5.4.3 En-face

For en-face images, we again averaged every 10 en-face frames. Enface averaging was necessary due to the tilted representation of the sample, induced by slight misalignment of the object and reference fibres.

An averaged en-face frame, across the metal plate, is shown in Fig. 5.20, cropped to a FOV of 0.82 *mm* by 0.82 *mm*, with 100 μm scale bars in both the x and y directions. Even with every 10 frames averaged, we still see the apparent tilt of the sample, cutting through the en-ace frame at an angle.

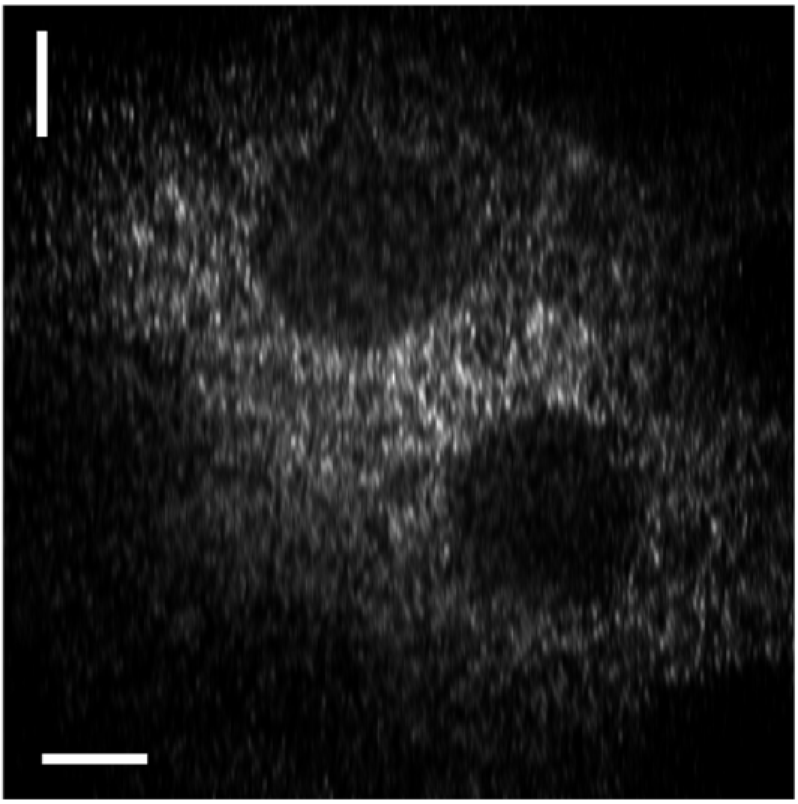

Figure 5.20: Averaged CMS en-face across plate, with 100 μm scale bars in both the x and y directions.

An averaged en-face frame, across the polymer layer is shown in Fig. 5.21, cropped to a FOV of 0.82 *mm* by 0.82 *mm*, with 100

μm lateral scale bars.

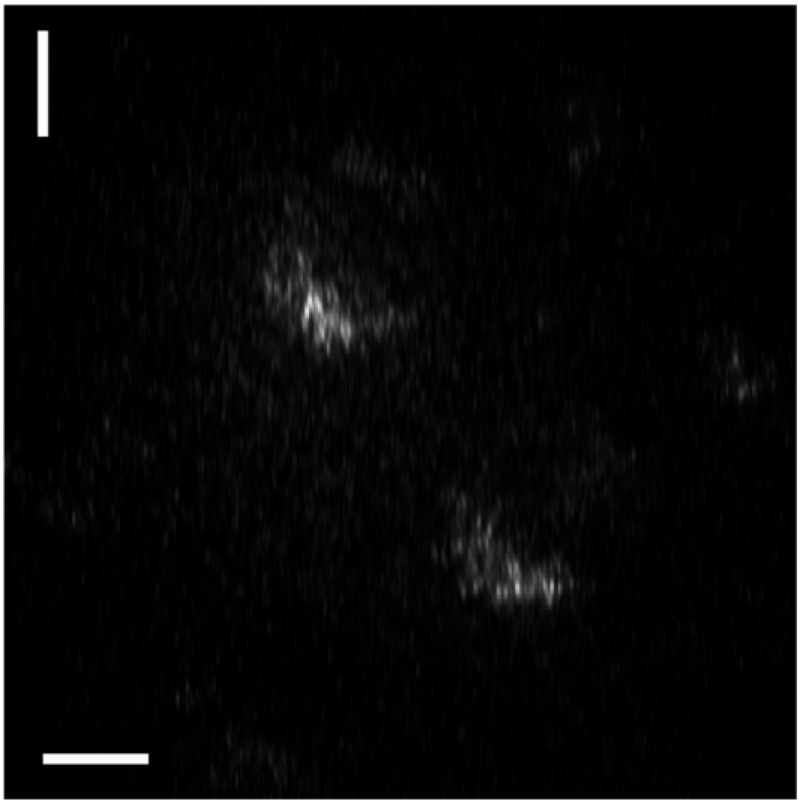

Figure 5.21: Averaged CMS en-face across polymer, with 100 μm scale bars in both the x and y directions.

Here, we observe an interesting phenomenon, whereby only a semi-circle of the polymer layer is visible. We can contrast this to the FFT en-face in which the whole circle is seen. This is perhaps due to the different depth of the polymer layers resolved in each case. In the CMS, the layer is at 0.16 mm, and perhaps at this depth half of the polymer layer is occluded by the metal plate. In contrast, in the FFT case, the layer is deeper and light reaching the polymer has scattered through the layers of tape, diffusing the beam so as to now illuminate across the whole circular region of polymer.

We cannot conclude that the method of processing has made a difference in what layers of polymer are resolved. Instead, we suggest that the off-axis object beam was perhaps in a different arrangement in the CMS and FFT data collections.

5.5 Conclusion

In this chapter, we have evaluated the performance of our OCT fibre bundle adapter, trying two different protocols, based around FFT or a CMS processing.

In the FFT approach, we obtained an SNR of $32\,dB$. This was sufficient to establish the presence of a polymer layer at a depth of approximately $0.6\ mm$. However, it was insufficient to resolve individual layers of tape, and would be incapable of resolving layers of tissue. Therefore, the sensitivity of the system would have to be refined in order to achieve OCT imaging from tissue.

The axial resolution achieved was comparable to the lateral resolution presented in chapter 4, of approximately $50\ \mu m$, although was found to degrade with OPD, having a best axial resolution of approximately $34\ \mu m$, and dropping to $\geq 40\ \mu m$ after $2\ mm$ of OPD. We can compare these obtained values of lateral and axial resolution to those typical of OCT, as presented in chapter 1 in Fig. 1.2. The values we have achieved are at the higher end of what is capable from OCT. However, the achieved resolutions are better than those typical of Ultrasound, at approximately half of the values given in Fig. 1.2.

The CMS method was explored as an alternative reconstruction strategy that could improve axial resolution. We successfully demonstrated mask synthesis and A-scan reconstruction by the CMS method. A superior axial resolution of approximately $20\ \mu m$ was delivered, albeit at a reduced SNR of $27\,dB$, and with persistent artefacts such as vertical streaking.

In comparing the two methods, the FFT approach currently provides more robust OCT results, while the CMS method shows promising axial resolution performance.

Chapter 6

Conclusion

6.1 Outcome of Thesis

In the introduction, we established the motivation for the thesis, i.e. that there currently exists a strong desire for forward-viewing E-OCT for clinical practice. Conventional scanning E-OCT has presented difficulties with regards to the attainable image quality and FOV, and from this we came to understand that fibre bundles, by allowing Full-field OCT without distal or proximal scanning, provide an exciting prospect for realizing forward-viewing E-OCT.

We have discussed the different ways in which OCT has been performed through fibre bundles, as reported in the referenced literature, and we understood that a common-path is desired for OCT. However, each of the common-path methods proposed in the literature have had drawbacks, preventing them from reaching clinical enrolment. There was therefore a motivation for a new method, which we have provided with our common-path adapter with angled divergent illumination. Having established the motivation, and the significance of the findings, we can now discuss the success of the work.

To have been a successful thesis, we have had to either disvalidate or validate our proposed way of performing OCT through a fibre bundle, either proving that the system can work, or by proving that it could not work. Both outcomes would present a development in the science of optics for medical imaging.

In that most core sense, the thesis has been successful, achieving rudimentary imaging results, and therefore demonstrating that it is indeed possible to perform OCT through a fibre bundle with our new compact adapter. With this advancement, we have provided a means of transforming a fibre bundle into a depth resolved imaging instrument. With further refinement and development, this new technology could perhaps become enrolled into clinical practice, potentially having great implications in medicine.

However, whilst we have proved the concept, a working version of this technology, fit for clinical adoption, is still some stages away from realization. OCT imaging from a biological sample has not yet been demonstrated. This is a key advancement, that realistically, would have to be proven in order for commercial interest, and hence for the funding to be made available to develop a clinical system. Attempts were made to obtain OCT imaging from biological samples, however, due to perhaps low collection of light from the sample through the adapter, we were not able to obtain clear OCT images in which structures could be identified.

As such, the achievement of imaging from tissue would be the next milestone in the continuation of research. In our experimentation, we were unable to achieve imaging from tissue, principally due the system's low SNR and sensitivity. We demonstrated that individual layers of polymer tape could not be resolved, despite being resolved when imaged with an'in bulk' OCT system. In considering future work we must therefore present potential ways in which the sensitivity could be improved. These are discussed in section 6.2 'Future work'.

6.1.1 Key Findings

In the process of achieving our principle goal, we also achieved a couple of significant findings. One of the key achievements of the thesis was the demonstration of close to on-axis coupling of fibre bundle cores from large angular injection of light. The key finding, to the best of my knowledge not elsewhere reported, was to use a thin diffuser flush at the distal face. With the diffuser in place we achieved a coupling enabling OCT to be performed. This finding was a critical result, as without this discovery, it would have been impossible for the proposed method to have worked.

A secondary key finding was the successful performance of CMS-OCT from our system. As mentioned in Chapter 2, CMS-OCT presents many benefits over traditional FFT-OCT. By proving the feasibility of performing CMS, we have opened up the avenue for the CMS method in an eventual clinically revision of the system. One of the main advantages of the CMS method is the securing of a greater axial resolution, due to the mitigation of the effects of dispersion, and with regards to SS-OCT, the effects of non-linear source tuning. We successfully demonstrated that the CMS method can secure a greater axial resolution. However, it was challenging to obtain high quality masks, and the true potential of this approach has not been realised. Due to these imperfections in the execution of the method, i.e. not successfully capturing object and reference stacks for background subtraction, we cannot fairly compare the method to the FFT approach. It is possible that the SNR of the CMS method could have rivalled or even exceeded that of the FFT results, although unfortunately we can not make this claim without further experimentation.

6.1.2 Fibre bundle availability

Due to limitations of available funding, it was hard to acquire different fibre bundles and compare their suitability for use with the adapter. Ideally, we would have liked to have compared fibre bundles from different manufactures, principally in testing the effects of angled coupling, for instance comparing leached (e.g. Schott) vs wound (e.g. Fujikura), as well as testing the same types with different parameters, e.g. different core size and core pitch.

However, a single high-resolution flexible fibre bundle, for instance from Schott or Fujikura, can typically cost upwards of £1000. These bundles are also fragile, and the cores are easily susceptible to damage, which if apparent over enough cores, makes the bundle obsolete.

Schott leached fibre bundles were acquired with the given funding, preferred due to their demonstrated suitability for FF-SS-OCT, exhibiting less cross-talk and less multimoding than alternative wound or fused bundles [7]. As such, with the given limited funding, it was sensible to acquire Schott leached bundles.

We acquired 3 Schott bundles within the available funding, two with a core pitch of 11.6 μm, and one bundle with 8 μm pitch, the latter being the bundle used in the results presented in the thesis.

The other two bundles, with 11.6 μm core pitch, were used in the process of initial experimentation, in which the set-ups for imaging of the proximal end and illumination of the distal end were established. In this process, both bundles were made obsolete due to damaged cores. As such we only had the 8 μm bundle left for characterization and OCT imaging. It would have been beneficial to have had the availability of more bundles for testing.

6.2 Future Work

6.2.1 CMS with background subtraction

The first thing to implement would be the correct performance of the CMS method, with successful acquisition of object and reference stacks for background subtraction.

A comprehensive study comparing the CMS method against the conventional FFT with dispersion compensation and tuning linearization could then be performed. In this study we could compare quantitative imaging metrics, such as axial resolution and SNR and determine the more suitable method.

6.2.2 Reference injection with an Ultra Thin Diffuser

An exciting line of research would be to experiment with ultra-thin diffusers. Such diffusers are available from 'WaveFront Technology', having a thickness as low as 25 to 35 μm [66], significantly thinner than the diffuser currently used, at 250 μm. With a thinner diffuser we would expect less attenuation of the object beam when imaged through the diffuser onto the bundle.

We would first have to establish the effects onto reference injection, to test if a similar or better coupling could be achieved. The available diffusing angles from 'Wavefront Technology' range from 5° to 50°, and therefore we would wish to again characterise the effects onto the object and reference beams for different diffusing angles. We would determine the most appropriate diffusing angle, and ensure a suitable coupling could be achieved without degrading lateral resolution of the object image.

We would expect an ultra-thin diffuser to secure more intensity in the object image received at the camera than with a conventional 250 μm thick diffuser. If so, we could match the power in the reference field at the camera by reducing the free-space section attenuation. This would deliver greater intensity at the camera, achieving a greater SNR and sensitivity. It may also allow for the exposure time to be reduced, enabling for faster OCT.

6.2.3 Experimentation at longer wavelengths - 1300 nm

An interesting line of research would be to switch to a swept source operating at a longer wavelength, such as at 1300 nm, for which FF-SS-OCT has been demonstrated [67].

At longer wavelengths we would expect less multimoding of cores [68], as well as reduced cross-talk between cores [59]. As such, we might expect to achieve a more suitable coupling for OCT of the angled reference beam. At longer wavelengths we also expect better penetration of light through a sample [69], albeit at a trade-off of a slightly broadened axial resolution.

However, performing OCT at 1300 nm presents its own difficulties. We require a camera sensitive to 1300 nm, such as a camera with an Indium-Gallium-Arsenide (InGaAs) sensor. These cameras are typically more expensive, noisier and slower than CMOS alternatives, as well as typically having less pixels across the sensor, limiting the attainable FOV and lateral resolution [70]. Furthermore, at 1300 nm, lenses exhibit greater aberrations due to increased dispersion [71]. With the small lenses used in the adapter, this may result in a significant reduction in the useable FOV.

However, despite these challenges, it would be sensible to acquire a 1300 nm swept source and a 1300 nm sensitive camera, and to repeat experiments of characterizing modal coupling under angled illumination, both with and without a diffuser in place. If this attains a significant improvement in coupling, it would be promising to reconstruct the adapter with lenses designed for 1300 nm and to experiment at generating OCT images at this longer wavelength.

6.2.4 An Improved Camera

Sensitivity and Bit-depth

Another potential way to improve SNR and sensitivity would be to use a camera with a greater sensor sensitivity, and a lower camera noise.

The camera sensitivity is predominately determined from the sensors quantum efficiency (QE), which for the Mikrotron camera we used was 35 % at 550 nm (and less still at 850 nm). To secure greater intensity, we would like a higher QE at 850 nm. This could be achieved with alternative CMOS cameras, such as the Dhyana 95 V2, which has a superior QE at 850 nm of over 45 %, as given in the appendices in Table. A.1 and Table. A.2. These cameras also have lower noise, and operate at 12-bit, further improving the attainable SNR.

Alternatively, we could consider using a camera with a sensor more sensitive to NIR light, such as a InGaAs sensor. Although, as a caveat, the state-of-the-art InGaAs cameras are typically noisier and slower than the leading CMOS alternatives [72], [73].

By using a camera more sensitive at 850 nm, and with less noise, we might expect to secure a greater SNR and sensitivity. However, this would only be true if the camera noise has dominated over other sources of noise, which in our system is more likely from other causes, such as noise due to multimoding and cross-talk.

A more sensitive camera could potentially permit a reduced exposure time, therefore acquiring frames in a shorter period an enabling for faster OCT.

Selecting a new camera

Market research was conducted across a wide range of manufactures, to find a 12-bit camera, suitable for FF-SS-OCT, i.e. with streaming and trigger input. A table comparing the parameters of a selected range of cameras has been produced, which is given in the appendix A.1.

Realistically, the selection of camera is limited by the desired end-price for a clincial instrument. With ample funding, the Dhyana 400 BSI V3 would perhaps be the best option, principally for its far superior QE at 850 nm (50%), and its 16-bit bit-depth. One caveat that would need to be addressed is whether the cover slip could be removed, as this creates multiple reflections, as were perhaps the cause of the multiple signal bands in the OCT images obtained with the adapter. This information was not readily disclosed from the manufacturer. If the cover slip can not be removed, it may be more beneficial to select a less well performing camera with a removable cover slip, such as the Adimec SAPPHIRE S-65A70, as given in Table. A.1 and Table. A.2, avoiding the effect of multiple reflections due to the cover-slip.

6.2.5 Application of Off-axis Holography

Off-axis Holography

The adapter features a superposition of an off-axis diverging reference wave with an on-axis object field, at the bundle face. This is similar to the set-up in Off-axis Holography, in which a collimated reference beam is tilted at a small angle relative to the object field resulting in a spatial modulation across the sensor of a camera.

The induced modulation has the effect of shifting the detected interference signal in the spatial frequency domain, displacing the signal from the zero-frequency (i.e. D.C.) component. By filtering in the spatial-frequency domain, the interference signal can be isolated from the D.C signal. In this way the off-axis geometry replaces the need for phase shifting, as is typically required in On-axis Holography.

Off-axis Holography is used for high-resolution surface topography, quantitative phase imaging of translucent samples, and highly sensitive vibrometry [74], [75].

Off-axis FF-SS-OCT

The principles of Off-axis Holography have already been applied to FF-SS-OCT. In this approach, named Off-axis FF-SS-OCT, [76], [77], [78], the reference arm is tilted to introduce a known spatial carrier frequency across the camera sensor. This shifts the cross-correlation terms to higher spatial frequencies, such that, in the spatial-frequency space, the signal term is separated from the D.C. signal and the mirrored complex conjugate signal.

A 2D-spatial Fourier transform is applied onto each frame captured by the camera. In the spatial frequency domain, a filter is then applied onto each image to isolate the signal term. This removes the D.C component and the conjugate signal term, i.e. the mirror term in FF-SS-OCT. The reverse 2D-spatial FT is then applied to the filtered signal, and finally an FFT along the spectral direction of each pixel performed to produce an OCT volume, as in conventional FF-SS-OCT.

Off-axis FF-SS-OCT has achieved real-time volumetric imaging with high sensitivity [79], and is particularly well-suited to detecting dynamic phase changes, such as in cellular motility studies [80].

Off-axis carrier detection

The equation for the spatial frequency of modulation obtained from an off-axis angle, θ, is given by

$$f = \frac{n}{\lambda} \cdot \sin(\theta) \tag{6.1}$$

Given the Nyquist sampling limit, the maximum resolvable spatial frequency from the Mikrotron camera with pixel pitch, p, is;

$$f = \frac{1}{2p} \tag{6.2}$$

Assuming $n = 1$, equating the two expressions and rearranging to give the critical angle, we obtain:

$$\theta_c \geq \arcsin(\frac{\lambda}{2p}) \tag{6.3}$$

With our camera of pitch, $p = 14\,\mu m$, and with our source at fixed central wavelength of $\lambda = 850\,nm$, we obtain a critical angle of, $\theta_c = 1.7°$. The angle of the reference wave in our adapter far exceeds this limit, which could create difficulties for performing Off-axis Holography with the current adapter and camera. However, it perhaps possible that an alias of the off-axis carrier modulation could be detected by our camera. Attempting the detection of a lower frequency aliased signal would be an interesting avenue for future work.

Alternatively, to capture the true non-aliased signal, we would need to either reduce the angle or opt for a camera with a much higher pixel pitch. For example, the Adimec Sapphire S-65A70, listed in Table. A.1 and Table. A.2, has a pixel pitch of 3.2 μm. At this pitch we could extend our angle up to $\theta_c = 7.63°$. This is a more realistically attainable angle of injection given the adapters geometry, although the NA would still need to be reduced below $NA = 0.13$.

Application with a fibre bundle

It would be beneficial to apply the D.C. and mirror term removal feature of Off-axis Holography with the fibre bundle adapter. Let us consider using the adapter with the Schott leached fibre bundle with $8\mu m$ core pitch.

Even with a suitable camera, the highest detectable spatial frequency is now limited by the core pitch. We could attempt to use a bundle with a much smaller core-spacing, such as the Fujikura FIGH-10-350S, with $3.4\mu m$ core pitch [81]. However, reducing the core pitch would introduce other problems, such as increased cross-talk. As such, we are mostly likely left resorting to detection of an aliased signal.

6.2.6 Further Miniaturization

Another step in future work is to reduce the size of the adapter, allowing it to be integrated into endoscopes, which could be achieved by reducing the size of the lenses. However this presents its own difficulties, for instance it could be harder to assemble the adapter and still keep a reasonable accuracy in the positioning of lenses. Furthermore, smaller lenses typically exhibit increased aberrations, which could reduce the useable FOV, and which would be further exacerbated with an inaccurate positioning of the lenses.

A potential way to mitigate these effects would be to replace the Plano-Convex lenses with Achromatic Doublets, having the effect of reducing chromatic aberrations. Commercially available achromats typically go down to a diameter of 2 mm, for instance from Edmund Optics [82], reaching a size amenable to endoscopy. At this diameter, lenses with 4 mm focal length are available, matching the NA and hence the angle of illumination in the current system. However, this would still generate an adapter 8 mm in length, which would present difficulties for endoscopy. As such, the focal length may have to be reduced further. This would have the consequence of increasing the angle of illumination, and hence further experimentation would need to be conducted into assessing the suitability of modal coupling at larger angles of injection. Also, the effects on object imaging at greater angles of illumination would also need to be tested.

6.3 Summary

In summary, a new method of performing OCT through an imaging fibre bundle, by angled divergent illumination, has been presented, in a small compact package well-suited to miniaturization. This 'adapter', can transform a fibre bundle into a depth resolved imaging instrument. With further development, perhaps in pursuing and achieving the approaches suggested for future work, this approach may lead to a forward-viewing depth-resolved endoscope, which could reduce patient suffering, by delivering real-time high resolution sub-surface images, as well as potentially working as a tool for highly accurate guidance of biopsies.

References

[1] T. Xie, D. Mukai, S. Guo, M. Brenner, and Z. Chen, "Fiber-optic-bundle-based optical coherence tomography," *Optics Letters*, vol. 30, no. 14, pp. 1803–1805, 2005. DOI: `10.1364/OL.30.001803`.

[2] A. Podoleanu, M. Marques, and M. Hughes, "Imaging apparatus and method, U.S. patent US11717154B2," 2023. [Online]. Available: `https://patents.google.com/patent/US11717154B2`.

[3] G. J. Tearney, M. E. Brezinski, S. A. Boppart, E. A. Swanson, J. F. Southern, and J. G. Fujimoto, "In vivo endoscopic optical biopsy with optical coherence tomography," *Science*, vol. 276, no. 5321, pp. 2037–2039, 1997. DOI: `10.1126/science.276.5321.2037`.

[4] M. J. Gora and G. J. Tearney, "Endoscopic optical coherence tomography: Technologies and clinical applications," *Biomedical Optics Express*, vol. 8, no. 5, pp. 2405–2444, 2017. DOI: `10.1364/BOE.8.002405`.

[5] X. Wu, L. Guo, H. Tian, X. Wang, and H. Li, "High-speed forward-viewing optical coherence tomography probe based on lissajous sampling and sparse reconstruction," *Optics Letters*, vol. 49, no. 13, pp. 3652–3655, 2024. DOI: `10.1364/OL.49.003652`.

[6] A. M. Jacobs, D. Kluge, R. Ladurner, A. Meining, S. Götz, and M. J. Gora, "Evaluation of a novel forward-looking opti-

cal coherence tomography probe for endoscopic applications: An ex vivo feasibility study," *Surgical Endoscopy*, 2024. DOI: `10.1007/s00464-024-11353-1`.

[7] H. D. Ford and R. P. Tatam, "Characterization of optical fiber imaging bundles for swept-source optical coherence tomography," *Applied Optics*, vol. 50, no. 5, pp. 627–640, 2011. DOI: `10.1364/AO.50.000627`.

[8] L. M. Wurster et al., "Endoscopic optical coherence tomography with a flexible fiber bundle," *Journal of Biomedical Optics*, vol. 23, no. 7, p. 071 204, 2018. DOI: `10.1117/1.JBO.23.7.071204`.

[9] A. Perperidis, D. Stoyanov, S. Ourselin, and T. Vercauteren, "Image computing for fibre-bundle endomicroscopy: A review," *Medical Image Analysis*, vol. 46, pp. 239–251, 2018. DOI: `10.1016/j.media.2018.03.005`.

[10] D. Huang et al., "Optical coherence tomography," *Science*, vol. 254, no. 5035, pp. 1178–1181, 1991. DOI: `10.1126/science.1957169`.

[11] K. Wang and C. Xu, "Optical coherence tomography for noninvasive imaging of epithelial tissue," *Journal of Biomedical Optics*, vol. 25, no. 6, p. 060 901, 2020. DOI: `10.1117/1.JBO.25.6.060901`.

[12] P. Gholami and V. Lakshminarayanan, *Optical coherence tomography image retinal database: Normal retinal oct images*, Ann Arbor, MI: Inter-university Consortium for Political and Social Research, 2019. DOI: `10.3886/E108503V1-24743`. Accessed: Jul. 14, 2025. [Online]. Available: `https://doi.org/10.3886/E108503V1-24743`.

[13] Edmund Optics. "Optical coherence tomography (oct) whitepaper," Edmund Optics Inc., Accessed: May 15, 2025. [Online]. Available: `https://www.edmundoptics.com/ViewDocument/OCT_Whitepaper_18.pdf`.

[14] W.-C. Kuo, J. Kim, N. D. Shemonski, et al., "Real-time three-dimensional optical coherence tomography image-guided core-needle biopsy system," *Biomedical Optics Express*, vol. 3, no. 6, pp. 1149–1161, 2012. DOI: `10.1364/BOE.3.001149`.

[15] P. Gholami et al., "Core needle biopsy guidance based on tissue morphology assessment with ai-oct imaging," *Biomedical Optics Express*, 2023. DOI: `10.3390/diagnostics13132276`.

[16] K. Groux et al., "Dynamic full-field optical coherence tomography module adapted to commercial microscopes allows longitudinal in vitro cell culture study," *Communications Biology*, vol. 6, p. 575, 2023. DOI: `10.1038/s42003-023-05378-w`.

[17] J. G. Fujimoto and E. A. Swanson, "The development, commercialization, and impact of optical coherence tomography," *Investigative Ophthalmology & Visual Science*, vol. 57, no. 9, OCT1–OCT13, 2016. DOI: `10.1167/iovs.15-17964`.

[18] J. F. de Boer, R. Leitgeb, and M. Wojtkowski, "Twenty-five years of optical coherence tomography: The paradigm shift in sensitivity and speed provided by fourier domain oct," *Biomedical Optics Express*, vol. 8, no. 7, pp. 3248–3280, 2017. DOI: `10.1364/BOE.8.003248`.

[19] A. F. Fercher, W. Drexler, C. K. Hitzenberger, and T. Lasser, "Optical coherence tomography – principles and applications," *Reports on Progress in Physics*, vol. 66, no. 2, pp. 239–303, 2003. DOI: `10.1088/0034-4885/66/2/204`.

[20] M. A. Choma, M. V. Sarunic, C. Yang, and J. A. Izatt, "Sensitivity advantage of swept source and fourier domain optical coherence tomography," *Optics Express*, vol. 11, no. 18, pp. 2183–2189, 2003. DOI: `10.1364/OE.11.002183`.

[21] A. C. Boccara, É. Beaurepaire, M. Lebec, L. Blanchot, and H. Saint-Jalmes, "Full-field optical coherence microscopy," *Optics Letters*, vol. 23, no. 4, pp. 244–246, 1998. DOI: `10.1364/OL.23.000244`.

[22] E. Auksorius, D. Borycki, and M. Wojtkowski, "Crosstalk-free volumetric in vivo imaging of a human retina with fourier-domain full-field optical coherence tomography," *Biomedical Optics Express*, vol. 10, no. 12, pp. 6390–6407, 2019. DOI: `10.1364/BOE.10.006390`.

[23] D. Lorenser, X. Yang, R. W. Kirk, B. C. Quirk, R. A. McLaughlin, and D. D. Sampson, "Ultrathin side-viewing needle probe for optical coherence tomography," *Optics Letters*, vol. 36, no. 19, pp. 3894–3896, 2011. DOI: `10.1364/OL.36.003894`.

[24] B. C. Quirk, R. A. McLaughlin, A. Curatolo, and D. D. Sampson, "In situ imaging of lung alveoli with an optical coherence tomography needle probe," *Journal of Biomedical Optics*, vol. 16, no. 3, p. 036 002, 2011. DOI: `10.1117/1.JBO.16.3.036002`.

[25] P. Liang, X. Liang, J. Zhou, et al., "Endoscopic optical coherence tomography: Technologies and clinical applications," *Journal of Biomedical Optics*, vol. 22, no. 8, pp. 1–16, 2017. DOI: `10.1117/1.JBO.22.8.080901`.

[26] Z. Yang, L. Wang, W. Chen, et al., "Eb-oct: A potential strategy on early diagnosis and treatment for lung cancer," *Frontiers in Oncology*, vol. 13, p. 1 156 218, 2023. DOI: `10.3389/fonc.2023.1156218`.

[27] X. Li, G. Wei, X. Wang, Y. Li, and J. G. Fujimoto, "Integrated endoscopic optical coherence tomography and laser-induced fluorescence for tissue characterization," *Optics Letters*, vol. 38, no. 20, pp. 3969–3972, 2013. DOI: `10.1364/OL.38.003969`.

[28] A. G. Douglas-Jones, P. R. Newstead, C. C. Erroll, and R. F. Hobson, "Diagnostic difficulty arising from displaced epithelium after core biopsy in intracystic papillary lesions of the breast," *Histopathology*, vol. 41, no. 5, pp. 428–432, 2002. DOI: `10.1046/j.1365-2559.2002.01406.x`.

[29] D. C. Adler and B. E. Bouma, "Submillimeter-diameter rotary-pullback fiber-optic endoscope for narrowband-red and swept-source optical coherence tomography," *Journal of Biomedical Optics*, vol. 25, no. 3, p. 032 005, 2020. DOI: `10.1117/1.JBO.25.3.032005`.

[30] Abbott. "Optical coherence tomography (oct) intravascular imaging," Abbott Cardiovascular, Accessed: Apr. 14, 2026. [Online]. Available: `https://web.archive.org/web/20250215061535/https://www.cardiovascular.abbott/us/en/hcp/products/percutaneous-coronary-intervention/intravascular-imaging/optical-coherence-tomography-oct.html`.

[31] Z. Qiu and W. Piyawattanametha, "Mems actuators for optical microendoscopy," *Micromachines*, vol. 10, no. 2, p. 85, 2019. DOI: `10.3390/mi10020085`.

[32] Y. Fan, S. Luo, L. Huo, and H. X. Kang, "An imaging analysis and reconstruction method for multiple-micro-electro-mechanical system mirrors-based off-centre scanning optical coherence tomography probe," *Journal of Biophotonics*, vol. 13, e202000041, 7 2020. DOI: `10.1002/jbio.202000041`.

[33] OmniVision Technologies, Inc., *Ov7251: Low-power, small-form-factor global shutter camerachip™ sensor datasheet*, `https://www.ovt.com/products/ov7251/`, 2024.

[34] H. D. Ford and R. P. Tatam, "Imaging fibre bundles for fizeau-based optical coherence tomography," in *Coherence*

Domain Optical Methods and Optical Coherence Tomography in Biomedicine XII, SPIE Proceedings Vol. 7168, 2008, 71682P. DOI: `10.1117/12.808953`.

[35] H. D. Ford and R. P. Tatam, "Fibre imaging bundles for full-field optical coherence tomography," *Measurement Science and Technology*, vol. 18, no. 9, pp. 2949–2956, 2007. DOI: `10.1088/0957-0233/18/9/030`.

[36] D. Hillmann, H. Spahr, H. Hainich, G. Hüttmann, and R. Huber, "Full field swept source oct for high speed en-face oct imaging," *Biomedical Optics Express*, vol. 1, no. 3, pp. 752–764, 2009. DOI: `10.1364/BOE.1.000752`.

[37] C. K. Hitzenberger, H. Sattmann, E. Sticker, M. Pircher, M. El-Zaiat, and A. F. Fercher, "Measurement and imaging of thicknesses of transparent tissues of the anterior eye by partial coherence interferometry," *Optics Express*, vol. 1, no. 6, pp. 73–74, 1997. DOI: `10.1364/OE.1.000073`.

[38] M. Wojtkowski, R. A. Leitgeb, A. Kowalczyk, T. Bajraszewski, and A. F. Fercher, "In vivo human retinal imaging by fourier domain optical coherence tomography," *Journal of Biomedical Optics*, vol. 9, no. 1, pp. 123–129, 2004. DOI: `10.1117/1.1626019`.

[39] R. Huber, D. C. Adler, and J. G. Fujimoto, "Buffered fourier domain mode locking: Unidirectional swept laser sources for optical coherence tomography imaging at 370,000 lines/s," *Optics Letters*, vol. 31, no. 20, pp. 2975–2977, 2006. DOI: `10.1364/OL.31.002975`.

[40] J. F. de Boer, B. Cense, B. H. Park, M. C. Pierce, G. J. Tearney, and B. E. Bouma, "Improved signal-to-noise ratio in spectral-domain compared with time-domain optical coherence tomography," *Optics Letters*, vol. 28, no. 21, pp. 2067–2069, 2003. DOI: `10.1364/OL.28.002067`.

[41] K. Hoh, B. Potsaid, V. Jayaraman, A. Cable, and J. G. Fujimoto, "Real-time k-space linearization for high-speed swept-source optical coherence tomography using an optical clock," *Optics Letters*, vol. 39, no. 19, pp. 5562–5565, 2014. DOI: `10.1364/OL.39.005562`.

[42] Y. Ling, K. Wang, M. Zhao, and Z. Chen, "Phase noise in swept-source optical coherence tomography due to timing jitter," *Optics Letters*, vol. 42, no. 23, pp. 4837–4840, 2017. DOI: `10.1364/OL.42.004837`.

[43] M. W. Jenkins, J. M. W. Brown, A. P. M. Michel, A. J. Welch, and T. E. Milner, "Phase-sensitive swept source optical coherence tomography using a fourier domain mode locked laser," *Optics Express*, vol. 15, no. 12, pp. 7634–7641, 2007. DOI: `10.1364/OE.15.007634`.

[44] J. P. Fingler, "Motion contrast using optical coherence tomography," Ph.D. dissertation, California Institute of Technology, Pasadena, CA, USA, Jul. 2007.

[45] S. Rivet, M. Maria, A. Bradu, T. Feuchter, L. Leick, and A. Podoleanu, "Complex master slave interferometry," *Optics Express*, vol. 24, no. 3, pp. 2885–2904, 2016. DOI: `10.1364/OE.24.002885`.

[46] A. G. Podoleanu, "Master–slave interferometry for long optical coherence tomography coherence lengths," *Electronics Letters*, vol. 44, no. 21, pp. 1228–1230, 2008. DOI: `10.1049/el:20082006`.

[47] A. Podoleanu and A. Bradu, "Master-slave interferometry for parallel spectral domain interferometry sensing and versatile 3d optical coherence tomography," *Optics Express*, vol. 21, no. 17, pp. 19 324–19 338, 2013. DOI: `10.1364/OE.21.019324`.

[48] R. Cernat et al., “Gabor fusion master slave optical coherence tomography,” *Biomedical Optics Express*, vol. 8, no. 2, pp. 813–827, 2017. DOI: `10.1364/BOE.8.000813`.

[49] A. Bradu and A. G. Podoleanu, “Master-slave interferometry – ideal tool for coherence revival gated dynamic oct,” *Biomedical Optics Express*, vol. 8, no. 1, pp. 326–346, 2017. DOI: `10.1364/BOE.8.000326`.

[50] A. Bradu, N. M. Israelsen, M. Maria, et al., “Recovering distance information in spectral domain interferometry,” *Scientific Reports*, vol. 8, p. 15 445, 2018. DOI: `10.1038/s41598-018-33805-1`.

[51] J. Wang, A. Bradu, G. Dobre, and A. Podoleanu, “Full-field swept-source master-slave optical coherence tomography,” *Optics Letters*, vol. 40, no. 15, pp. 3570–3573, 2015. DOI: `10.1364/OL.40.003570`.

[52] D. Hillmann et al., “Aberration-free volumetric high-speed imaging of in vivo retina,” *Scientific Reports*, vol. 6, p. 35 209, 2016. DOI: `10.1038/srep35209`.

[53] J. Fergusson, “Full-field swept source optical coherence tomography,” Ph.D. dissertation, Cardiff University, 2012. DOI: `10.13140/RG.2.2.14005.91364`.

[54] D. Hillmann et al., “Holographic optical coherence tomography with long multimode fiber illumination,” *arXiv preprint*, 2023. DOI: `10.48550/arXiv.2309.08486`.

[55] T. N. Ford and J. Mertz, “Phase-gradient microscopy in thick tissue with oblique back-illumination,” *Nature Methods*, vol. 7, no. 4, pp. 307–309, 2010. DOI: `10.1038/nmeth.1430`.

[56] W. Qi, Q. Li, and X. Liu, “Full-field optical coherence tomography based on a 2d fibre bundle,” *Biomedical Optics Express*, vol. 4, no. 6, pp. 915–926, 2013. DOI: `10.1364/BOE.4.000915`.

[57] AMS Technologies. “Fiber bundles and assemblies product page,” AMS Technologies, Accessed: Jul. 14, 2025. [Online]. Available: `https://shop.amstechnologies.com/Products/Optical-Technologies/Fibers-Fiber-Optics/Patch-Cables-Bundles-Assemblies/Fiber-Bundles-Assemblies/`.

[58] National Institutes of Health and the Laboratory for Optical and Computational Instrumentation. “Imagej - image editing software,” ImageJ.net, Accessed: Apr. 7, 2026. [Online]. Available: `https://imagej.net/ij/`.

[59] J.-H. Han and J. U. Kang, “Analysis of multimode fiber bundles for spectral-domain optical coherence tomography,” *Applied Optics*, vol. 54, no. 12, pp. 3574–3581, 2015. DOI: `10.1364/AO.54.003574`.

[60] W. Wang, K. Zhang, Q. Ren, and J.-U. Kang, “Comparison of different focusing systems for common-path optical coherence tomography with fiber-optic bundle as endoscopic probe,” *Optical Engineering*, vol. 48, no. 10, p. 103 001, 2009. DOI: `10.1117/1.3250270`.

[61] X. Liang, S. A. Boppart, and C. Xu, “Design of miniaturized optical coherence tomography probes for in vivo imaging,” *IEEE Journal of Selected Topics in Quantum Electronics*, vol. 18, no. 4, pp. 1227–1239, 2012. DOI: `10.1109/JSTQE.2012.2186195`.

[62] Z. Qin, C. Chen, S. He, J. Qu, et al., “Adaptive optics two-photon endomicroscopy enables deep brain imaging at synaptic resolution over large volumes,” *Science Advances*, 2020. DOI: `10.1126/sciadv.abc6521`.

[63] J. Zhu, Y. Qu, S. Yang, and Y. Zhang, “Fabrication and characterization of high na ball-lensed fiber tips for optical coherence tomography,” *Optics Express*, vol. 20, no. 6, pp. 5834–5840, 2012. DOI: `10.1364/OE.20.005834`.

[64] Olympus Corporation. "Specifications of olympus echoendoscopes," Olympus Corporation, Accessed: Jul. 14, 2025. [Online]. Available: `https://www.olympus.co.uk/medical/en/Products-and-Solutions/Products/Endoscopy/`.

[65] M. Plöschner, T. Tyc, and T. Čižmár, "Seeing through chaos in multimode fibres," *Nature Photonics*, vol. 9, no. 8, pp. 529–535, 2015. DOI: `10.1038/nphoton.2015.112`.

[66] Wavefront Technology, Inc., *Tailored ultra-thin diffusers*, `http://www.wft.bz/lightfilms/utmd.htm`, Accessed: 2025-07-13, n.d.

[67] S. J. Leigh, S. Choudhury, M. S. Brewer, M. J. Biggs, and L. M. Baker, "Full-field swept-source optical coherence tomography at 1310nm for neurosurgical guidance," *Communications Biology*, vol. 3, p. 678, 2020. DOI: `10.1038/s42003-020-01252-3`.

[68] Z. A. Steelman, S. Kim, E. T. Jelly, M. Crose, K. K. Chu, and A. Wax, "Comparison of imaging fiber bundles for coherence-domain imaging," *Applied Optics*, vol. 57, no. 6, pp. 1455–1462, Feb. 2018. DOI: `10.1364/AO.57.001455`.

[69] D. Huang, T. Fussell, P. Keating, and J. Miller, "Enhanced tissue penetration in optical coherence tomography imaging at 1310nm," *Physics in Medicine Biology*, vol. 63, no. 9, p. 095 020, 2018. DOI: `10.1088/1361-6560/aab4e9`.

[70] Edmund Optics. "Understanding camera sensors for machine vision applications," Accessed: Apr. 15, 2026. [Online]. Available: `https://www.edmundoptics.com/knowledge-center/application-notes/imaging/understanding-camera-sensors-for-machine-vision-applications/`.

[71] C. Joo, T. Akkin, B. Cense, B. H. Park, and J. F. de Boer, "Spectral-domain optical coherence phase microscopy for quantitative phase-contrast imaging," *Optics Letters*, vol. 31, no. 9, pp. 1260–1262, 2006. DOI: `10.1364/OL.31.001260`.

[72] W. Wieser, B. R. Biedermann, C. M. Eigenwillig, T. Klein, and R. Huber, "Multi-megahertz oct: High quality 3d imaging at 20 million a-lines per second," *Optics Express*, vol. 18, no. 14, pp. 14 685–14 704, 2010. DOI: `10.1364/OE.18.014685`.

[73] L. Liu, R. K. Wang, P. He, and R. K. Wang, "High-speed optical coherence tomography imaging of the retina using a 1.6-mhz swept source at 1.06 µm," *Biomedical Optics Express*, vol. 2, no. 7, pp. 1864–1878, 2011. DOI: `10.1364/BOE.2.001864`.

[74] E. Cuche, P. Marquet, and C. Depeursinge, "Digital holography for quantitative phase-contrast imaging," *Optics Letters*, vol. 24, no. 5, pp. 291–293, 1999. DOI: `10.1364/OL.24.000291`.

[75] G. Coppola, P. Ferraro, and D. Alfieri, "Off-axis holography: A review of fundamentals and emerging applications," *Applied Sciences*, vol. 8, no. 9, p. 1576, 2018. DOI: `10.3390/app8091576`.

[76] J.-M. Schmitt and T. Lasser, "Full-field optical coherence tomography: A new technology for 3d microscopy," *Nature Methods*, vol. 1, pp. 93–94, 2004. DOI: `10.1038/nmeth711`.

[77] B. Baumann, S. Zotter, M. Pircher, and C. K. Hitzenberger, "Off-axis full-field swept-source optical coherence tomography: A method for complex signal acquisition without phase-shifting interferometry," *Optics Letters*, vol. 33, no. 11, pp. 1141–1143, 2008. DOI: `10.1364/OL.33.001141`.

[78] D. Hillmann et al., "Off-axis reference beam for full-field swept-source oct and holoscopy," *Optics Express*, vol. 25, no. 22, pp. 27 770–27 784, Oct. 2017. DOI: `10.1364/OE.25.027770`.

[79] Y. Watanabe, T. Takahashi, H. Koizumi, and T. Yatagai, "Off-axis full-field swept-source optical coherence tomography using a high-speed camera," *Optics Express*, vol. 25, no. 4, pp. 4114–4128, 2017. DOI: `10.1364/OE.25.004114`.

[80] R. K. Wang, "Label-free imaging of blood vessels using optical microangiography," *Microscopy Research and Technique*, vol. 74, no. 10, pp. 927–938, 2011. DOI: `10.1002/jemt.20978`.

[81] O. Hirsch, S. A. Boppart, and L. Bates, "Use of imaging fiber bundles for coherence-domain imaging," *Journal of Biomedical Optics*, vol. 23, no. 12, p. 121 610, 2018. DOI: `10.1117/1.JBO.23.12.121610`.

[82] Edmund Optics. "Vis-nir coated achromatic lenses," Edmund Optics, Accessed: Jul. 14, 2025. [Online]. Available: `https://www.edmundoptics.com/f/vis-nir-coated-achromatic-lenses/13536/`.

Appendix A

Supplementary Material

A.1 Camera Market Research

In considering future work, we identified upgrading the camera as a promising direction. Market research was conducted to identify and compare features of the market-leading Machine Vision cameras. We first narrowed down our search by demanding a 12-bit or greater bit-depth. A total number of 12 cameras were identified and compared, presented along with the current camera (EoSens MC1360-63) along the first row, and are presented over two tables; in Table. A.1 and Table. A.2.

Camera	Frame Size	Pixel Size (μm)	Sensor Size (mm)	Bit-depth	DR (dB)	SNR (dB)	1.3Mp fps
Mikrotron [EoSens CL_MC1360-63]	1280 x 1040	14.00	22.9 (D)	10	60.2	N/S	512
Emergent [HB-1800-S-M]	1604 x 1100	9.00	N/S	12	53.7	N/S	896
Lambert [HS1000]	1280 x 1024	6.60	N/S	12	60.2	45	1000
Mikrotron [EoSens 1.3MCL-CM]	1280 x 1040	14.00	17.92 x 14.34	10	N/S	N/S	506
Mikrotron EoSens 10MCX12-CM	4608 x 2176	4.50	20.74 x 9.79	12	N/S	68.8	3686
Thorlabs Kiralux CS505MU	2448 x 2048	3.45	8.45 x 7.07	12	N/S	71	134
Adimec SAPPHIRE S-65A70	9344 x 7000	3.20	37.4 mm (D)	12	N/S	62.3	206
Dhyana: 400 BSI V3	2048 x 2048	6.50	13.3 x 13.3	16	N/S	86	82
Dhyana: 401D	2048 x 2048	6.50	13.3 x 13.3	16	N/S	N/S	82
C-BLUE One 1.7 MP	1608 x 1104	9.00	17.6 (D)	12	53.7	N/S	2716
Optronis [CP70-1-M/C-1000]	1280 x 1024	6.60	8.45 x 6.76	12	55.8	45	1040
Phantom [S641]	2560 x 1600	10.00	10.82 (D)	12	N/S	41.7	4568
Phantom [S710]	1280 x 800	20.00	25.6 x 16.0	12	N/S	59.6	4521

Table A.1: Camera Comparison – Part 1. Acronyms; DR: Dynamic Range, N/S: Not Stated, D: Diagonal.

Camera	Cover Slip	Cost	Dark Current	Dark Noise	FWC (k e-)	QE (550 nm)	QE (850 nm)	Streaming Interface
Mikrotron [EoSens CL_MC1360-63]	N/S	£3000	200 mV/s	N/S	N/S	35%	~18%	Camera Link Full
Emergent [HB-1800-S-M]	Yes	£5126	N/S	N/S	N/S	N/S	N/S	25GigE
Lambert [HS1000]	N/S	N/S	N/S	N/S	N/S	53%	23%	CXP-6
Mikrotron [EoSens 1.3MCL-CM]	N/S	N/S	N/S	N/S	N/S	35%	12%	Camera Link
Mikrotron EoSens 10MCX12-CM	Yes	£8190	N/S	N/S	30	68%	16%	CXP-12
Thorlabs Kiralux CS505MU	Removable	£2035	<0.25 e/px/s	2.5	120	72%	20%	USB3.0
Adimec SAPPHIRE S-65A70	Removable	N/S	N/S	N/S	10	64%	10%	CXP-12
Dhyana: 400 BSI V3	N/S	£8950	0.15 e/px/s	1.1	45	95%	50%	Camera Link
Dhyana: 401D	N/S	£4250	N/S	2.1	45	72%	34%	Camera Link
C-BLUE One 1.7 MP	N/S	£15,047	N/S	2.33	94	73%	19%	CXP
Optronis [CP70-1-M/C-1000]	N/S	£5200	N/S	N/S	17	54%	24%	Camera Link
Phantom [S641]	N/S	~£35k	24517 e/s	4.53	23.8	58%	21%	CXP12 (8ch)
Phantom [S710]	N/S	<£40k	N/S	N/S	29.0	N/S	N/S	CXP12 (16ch)

Table A.2: Camera Comparison – Part 2. Acronyms; FWC: Full Well Capacity, QE: Qauntum Efficiency, N/S: Not Stated, e/px/s: electrons per pixel per second, CXP CoaXPress.

List of Data Sheets

- **Mikrotron EoSens 1.3MCL-CM**: `https://mikrotron.de/en/high-speed-cameras/mik-camera-detail.php?id=EoSens%C2%AE1.3MCL-CM`
- **Emergent HB-1800-S-M**: `https://honzhigan.com/wp-content/uploads/2021/12/Datasheet-HB-1800-S.pdf`
- **Lambert HS1000**: `https://www.lambertinstruments.com/hs1000#hs1000-specs`
- **Mikrotron EoSens 10MCX12-FM**: `https://mikrotron.de/en/high-speed-cameras/mik-camera-detail.php?id=EoSens%C2%AE10MCX12-FM`
- **Thorlabs Kiralux CS505MU**: `https://www.thorlabs.com/thorproduct.cfm?partnumber=CS505MU`
- **Adimec SAPPHIRE S-65A70**: `https://www.adimec.com/cameras/machine-vision-cameras/sapphire-series/the-sapphire-s-65a70-camera/#1660045795774-ecc2e701-0a6c`
- **Dhyana 400 BSI V3**: `https://www.tucsen.com/scmos-dhyana-400bsi-v3-product/`
- **Dhyana 401D**: `https://www.tucsen.com/dhyana-400d-product/`
- **C-BLUE One 1.7 MP**: `https://www.first-light-imaging.com/wp-content/uploads/2023/06/Datasheet_C-BLUE-One_09.06.2023.pdf`
- **Optronis CP70-1-M/C-1000**: `https://optronis.com/wp-content/uploads/2017/01/CP70-1-MC-1000-C.pdf`

- **Phantom S641 (Machine Vision)**: `https://www.phantomhighspeed.com/products/cameras/machinevision/s641`
- **Phantom S710 (Machine Vision)**: `https://www.phantomhighspeed.com/products/cameras/machinevision/s710`

A.2 Matlab Code

Specialised MATLAB scripts were developed throughout the course of the thesis, of which a selection used in the thesis are presented here. The section titled ‘Attaining g and h functions and masks from filtered CS’, is not my original material, and the rightful authors are mentioned in the acknowledgements.

The developed MATLAB scripts are presented in order of their use in the thesis.

A.2.1 Chapter 3

Measuring reference beam FWHM

```
%% Measure FWHM of beam

%% Apply Gaussian blur

filterSize = 100;
filter = fspecial('Gaussian', filterSize, filterSize);
Image_blur = imfilter(Image_0, filter);

%% Rotate Image to align beam along x

angle = 8.8;
Image_rot = imrotate(Image_blur,angle,'crop');


%% Extract line profile

line = zeros(800,1);
line = squeeze(Image(:,400)));

%% Measure FWHM of beam

x = 1:800;  % X indicies
y = line;   % Y values

% Find indices where y crosses 0.5
idx = find((y(1:end-1) < 0.5 & y(2:end) > 0.5) | (y(1:end-1) >
    0.5 & y(2:end) < 0.5));

% Linear interpolation for accuracy
```

```
x_half = x(idx) + (0.5 - y(idx)) ./ (y(idx+1) - y(idx)) .* (x(
    idx+1) - x(idx));

% Display results
disp(['X-values where Y = 0.5: ', num2str(x_half)]);
```

Listing A.1: Measuring FWHM of reference beam FWHM

Measuring mean intensity of coupled reference light

```
%% Computing coupled intensity in region about centroid of beam


%% Rotate image to align beam along x

angle = 8.8;
I = imrotate(Image_raw,angle,'crop');


%% Computing Centroid

centroid = zeros(1,2);

size_image = size(I);
% Create coordinate matrices
[X, Y] = meshgrid(1:size_image(2), 1:size_image(1));
% Compute centroid
M = sum(I(:));  % Total intensity
centroids(i,1) = sum(X(:) .* I(:)) / M;  % x co-ord
centroids(i,2) = sum(Y(:) .* I(:)) / M;  % y co-ord


%% Crop image about centroid

% vaulating a 100 by 100 pixel region
crop = 100;

I_crop = I(centroids(1,2) - crop : centroids(1,2) + crop -1 , centroids(1,1) - crop : centroids(1,1) + crop -1);


%%  Find weighted intenisty of cropped image

M = sum(I_Crop,'all');
val = M / ( size_image(2)*size_image(1));


%% Applying beam size correction
% (to normalize fibre to bundle distance)

% distance normalization factor (measured in previuis script) e.g;
d = 1.28;

%distance normlaized intensity value
val_d = zeros(1,2);
```

```
val_d = val .* (1/d);
```

Listing A.2: Measuring mean intensity of beam in 100 by 100 pixel region about centroid, with beam distance correction factor applied.

A.2.2 Chapter 5

Windowed FFT and background subtraction

```
%% Windowed FFT with background subtraction

% S = Signal stack
% Obj = Object stack
% Ref = Refernce stack

%% Windowing with Hamming filter

size_image = size(S);
M = size_image(3);
size_ham = 0.8 % Size of Hamming filter

ham = reshape(0.8 * hamming(M), [1, 1, M]); % Reshaping filter

S = S .* ham;
Ref = Ref .* ham;
Obj = Obj .* ham;

%% FFT and background subtractions

FFT_S = abs(fftshift(fft(S, [], 3), 3));
FFT_Obj = abs(fftshift(fft(Obj, [], 3), 3));
FFT_Ref = abs(fftshift(fft(Ref, [], 3), 3));

FFT_sub = FFT_S - FFT_Obj - FFT_Ref;

%% Setting all < 0 to 0

FFT_sub(FFT_sub < 0) = 0;
```

Listing A.3: Windowing with Hamming filter, performing FFT over signal and background stacks, and peforming background subtraction.

Performing average en-face subtraction

```
%% Average en-face subtraction

% V = Volume before en-face subtraction
% Volume = Volume after en-face subtraction

```

```
% Compute mean across en-face frames (dimension 2)
meanImage = mean(V, 2);  % size: [rows, 1, cols]

% Subtract mean image from each en-face frame
Volume = V - meanImage;

%Set all values < 0 to 0
Volume(Volume < 0) = 0;
```

Listing A.4: Subtracting average of all en-face images from each en-face image.

Measuring Axial resolution of A-scan peak

```
%% Axial resolution measuremnt:

%% 1. Find region of peak

A_scan = squeeze(Volume(y,:,x));

figure
plot(A_scan);
% e.g. range 160 to 260

%% 2. Compute FWHM

% Define scaling factor
depthScale = 1.25;  % micrometers per index

% Define the range of interest
rangeStart = 160;
rangeEnd = 260;

% Extract region of interest
x_region = (rangeStart:rangeEnd)';
depth_um = x_region * depthScale;  % Convert index to
    micrometers
y_region = Volume(cs_y, rangeStart:rangeEnd, cs_x);

% Find peak in the region
[peakValue, localIdx] = max(y_region);
peakIdx = x_region(localIdx);  % Index where peak occurs
peakDepth = peakIdx * depthScale;  % Convert to micrometers

% Compute half maximum
halfMax = peakValue / 2;
```

```
fprintf('Half max: %.4f\n', halfMax);
fprintf('Value: %.4f\n', peakValue);

% Create fine resolution x values (interpolated)
x_fine = linspace(rangeStart, rangeEnd, 1000);
depth_fine = x_fine * depthScale;  % Fine depth in micrometers
y_fine = interp1(x_region, y_region, x_fine, 'linear');

% Find where y_fine crosses halfMax
crossings = depth_fine(abs(y_fine - halfMax) < 0.005); % Tolerance for crossing

if length(crossings) < 2
    error('Could not find two valid crossings for FWHM.');
end

% Assign FWHM boundaries
x1 = crossings(1);
x2 = crossings(end);
FWHM = x2 - x1;
```

Listing A.5: Measuring axial resolution of A-scan peak.

Calculating SNR of A-scan

```
%% SNR Calculation - by Standard deviation

%% 1. Find region of peak

A_scan = squeeze(Volume(y,:,x));
figure
plot(A_scan);

%Maually determine region of peak
% e.g.  160 - 260

%Maually determine region of noise
% e.g.  80 - 130

%% Perfrom SNR calculation

% Measure signal amplitude
signalPeak = max(Volume(y,160:260,x));

% Measure standard deviation of noise
noiseRegion = Volume(y,80:130,x);
noiseStd = std(noiseRegion);

% SNR using standard deviation of noise
SNR_dB = 20 * log10(signalPeak / noiseStd);
```

Listing A.6: Calculating SNR of A-scan.

Selecting pixel with greatest SNR to extract CS

```
%% locate_pixel_for_CS_vectorized_SNR_method

function [y, x, FFT] = locate_CS_pixel(S1, crop, delta_OPD_um)

% INPUTS:
%  S1:  signal stack
%  crop:  margin to exclude at edges
%  delta_OPD_um:  OPD step size per depth pixel, in microns (e.g., 16)

% OUTPUTS:
%  y,x:  Co-ordinates of selected pixel
%  FFT:  FFT stack of S1

% Get size
size_image = size(S1);
M = size_image(3);  % Number of spectral points (k-steps)

% FFT stack (magnitude)
FFT = abs(fftshift(fft(S1, [], 3), 3));  % [Y x X x K]

% Parameters
dc_exclude = 30;                         % Exclude central DC peak
signal_range = (M/2 + dc_exclude):M;     % Region for signal estimation
noise_range = (M - 100 + 1):M;           % Tail region for noise

% Initialize SNR map
snr_map = zeros(size_image(1), size_image(2));

% Compute SNR for each pixel
for i = 1+crop : size_image(1) - crop
    for j = 1+crop : size_image(2) - crop
        ascan = squeeze(FFT(i, j, :));  % 1D A-scan

        % Signal and noise
        signal = max(ascan(signal_range));
        noise = mean(ascan(noise_range));

        % SNR calculation
        if noise > 0
            snr_map(i, j) = signal / noise;
        else
            snr_map(i, j) = 0;
```

```
        end
    end
end

% Find best pixel by SNR
[~, linear_idx] = max(snr_map(:));
[y, x] = ind2sub([size_image(1), size_image(2)], linear_idx);

end
```

Listing A.7: Selecting pixel with greatest SNR A-scan

Applying Bandpass Filter to CS at selected pixel

```
%% Bandpass Filter

%Bandwidth of bandpass filter
delta_f = 80;

%Lower bounds of bandpass filter;
f1 = 350;  % OPD 1
f2 = 550;  % OPD 2
f3 = 850;  % OPD 3

%Bandpass Filter
[filt] = bandpass_filter(S1,S2,S3,y,x,delta_f,f1,f2,f3);

%INPUTS:
% S1,S2,S3: Raw Stacks at 3 differnet OPD
% cs_y,cs_x: Co-ordinates of selected pixel

%OUTPUT:
%filt: 3 CS at differnet OPD
```

Listing A.8: Applying bandpass filter onto CS at selected pixel

Attaining g and h functions and masks from filtered CS

```matlab
%% Appendix Attaining g and h and mask array

% Sequence of nestled functions, with user input of vsriables to first
% function; [masks,g,h] = g_h_and_masks(filt, interval,z_start,z_finish);

%  Inputs:
% filt: Array of 3 filtered CS
% interval:  distance between stacks (mm) (distance in z, not OPD)
% z_start: start of depth (mm)
% z_finish: dend of depth (mm)

% Outputs:
% masks: M by M mask array of complex values
% g: g function
% h: h function

%% Inputting variables to g_h_and_masks function

% Define depth interval
interval = 0.125;

% Choose depth of CMS reconstruction
z_start = 0;
z_finish = 1;

[masks,g,h] = g_h_and_masks(filt, interval,z_start,z_finish);


%% Function - g_h_and_masks

function [masks,g,h] = g_h_and_masks(filt,interval,z_start,z_finish);

 M = length(filt(1,:));
 size_array= size(filt(:,1));
 L = size_array(1);

% Assign CS to variable in synatx for subsequent function
E = zeros(M,L);
for i = 1:L
E(:,i) = filt(i,:);
end

```

```
% Generate g,h and masks
[masks,z,g,h] = generate_new_masks(E,interval,z_start,z_finish,M);

end

%% Function - generate_new_masks

function [masks,z,g,h]=generate_new_masks(m,dz,zmin,zmax,n)

% === INPUTS ===
% n:    int16, Number of masks to be generated over the range zmin,zmax
% m:    NxP matrix, the experimental P masks of size N
% === OUTPUTS ===
% cs:   nxN matrix, the generated masks
% z:    nx1 array, z vector for the Ascan plot

% clf;
warning off;
% figure()
% [g,h]=g_h_2spectra(m,dz);
[g,h]=g_h(m,dz);


%[z_new,N_new]=create_z(m,dz,zmin,zmax,n);
%[z_new,N_new]=create_z_from_2CS(m, dz, zmin, zmax, n);

z=linspace(zmin,zmax,n);
l=length(g);

% == Window ==
% W=hamming(l);   % Hamming apodization
W=ones(l,1);     % No apodization

% == Low pass filter (??) ==
F=zeros(l,1);
ll=5:round(l/2);
F(ll)=ones(length(ll),1);

% == Generation of the masks ==
for u=1:length(z)
    phase(:,u)=z(u)*g+h;              %    phase(:,u)=z(u)*g+h;
    dg=diff(g);
    dg(length(dg)+1)=dg(length(dg)); % Add one point in the end (?)

    masks(:,u)=dg.*exp(+1i*phase(:,u));

```

```
    masks(:,u)=ifft(fft(masks(:,u)).*F); % Filtering

    masks(:,u)=masks(:,u).*W; % Windowing

end

end


%% Fucntion: g_h

function [g,h,dg,z] = g_h(E,dz)

% === INPUTS ===
% E: [m,n] matrix. M = # of points in CS, n = # of Experimental CS.
% dz: float, distance between two consecutive spectra [in mm]
% === OUTPUTS ===
% g: nx1 array,
% h: nx1 array,

    [m,n]=size(E);
    %% Peak detection (FFT space)
    for i=1:n
        [mx,idv(i)] = max(fftnospline(E(:,i)));
    end
    slope = (idv(n)-idv(1))/((n-1)*dz);

   % disp(dz);

    %slope = dv/dz = sepertion of peaks in spectral / seperation of dept in real space of experimental masks)

    %% Phase extraction (CS space)
    for i=1:n
        z(i)=idv(i)/slope;
        E(:,i) = hilbert(E(:,i));
        dphase(:,i)=diff(unwrap(angle(E(:,i)))); % Phase difference for each 2 consecutive spectra
    end


    %% Generation of g and h for each 2 consecutive spectra
    tmp1=0;tmp2=0;
    for k=1:(m-1) % Going through the wavenumber array
        f=dphase(k,:);  %Vector of all the phase difference along k, 1 vector for each CS's phase difference along k
        p=polyfit(z,f,1); %  polyfit(x,y,degree of polynolial)
```

```
        dg(k)=p(1);    %i.e gradient of fit functin over interval of k = interval piece of g function (dg/dk)
        dh(k)=p(2);    %i.e.  intercept of fit function over inerval of k = interval piece of h function (dh/dk)
        g(k)=tmp1+dg(k);  % cumulative sum of dg/dk
        h(k)=tmp2+dh(k);  % cumulative sum of dh/dk
        tmp1=g(k);
        tmp2=h(k);
    end

    % ^ i.e. above, with each iteration we found pieces of g and h,
    % then made vectors g and h and added each piece onto the next entry in vector,
    % therefore building the g and h curves.

    % Adding on last value to the end of g and h , and dg and dh
    % (i.e. the last point k=M, which is exluded from the for loop)
    h=[h h(k)];
    g=[g g(k)];
    dg=[dg dg(k)];dg=dg';
    dh=[dh dh(k)];dh=dh';

    % Make g and h start at 0
    h=(h-h(1))';
    g=(g-g(1))';

%      x = linspace(1,length(h),length(h));
%      [curve,gof] = polyfit(x,h,7);
%      h1 = polyval(curve,x);
%      h = h1';
end
```

Listing A.9: Attaining g and h functions and masks from filtered CS

D.C. Term removal

```
%% CMS: DC Term Removal (Per-Pixel Mean Over k)

% Input: S_raw  (raw signal stack)
% Output: S   (cleaned signal stack)

[Y, X, K] = size(S_raw);

% Step 1: Permute to [K, Y, X]
S_raw_perm = permute(S_raw, [3, 1, 2]);  % [800, 600, 600]

% Step 2: Reshape to 2D: [K x N_pixels]
S_reshaped = reshape(S_raw_perm, K, Y*X);  % [800 x 360000]

% Step 3: Subtract DC (mean over K)
DC = mean(S_reshaped, 1);                  % [1 x 360000]
S_clean = S_reshaped - DC;                 % [800 x 360000]

% Step 4: Reshape back to [K, Y, X]
signal_stack_clean_perm = reshape(S_clean, K, Y, X);  % [800,
    600, 600]

% Step 5: Permute back to [Y, X, K]
S = permute(signal_stack_clean_perm, [2, 3, 1]);  % [600, 600,
    800]
```

Listing A.10: Applying a D.C. term removal as replacemnt to background subtraction.

CMS Matrix Multiplication

```
%% CMS Processing -

% CMS proccrsing of signal stack, S, using masks.

%% CMS matrix multiplication

V = abs(pagemtimes(S, masks)); % U(:,i,j)' * masks for all i,j
```

Listing A.11: Generation of CMS volume by matrix multiplcation of signal stack with masks

Applying Gaussian Filter to all en-face frames

```
function [S] = Gaussian_smooth(S,filterSize);

%INPUT:
% S: Image Stack
% filterSize: lenght of filter in pixels
imsize= size(S);

filter = fspecial('Gaussian', filterSize, filterSize);
for k = 1:imsize(3);
    S(:,:,k) = imfilter(S(:,:,k), filter);
end

end
```

Listing A.12: Applying Gaussian filter onto all en-face frames

A.3 LabView Code

The LabView code used to acquire images from the camera in real-time, consists of two main components, an image acquisition part and an image extraction and processing part.

Acquisition Part

The block diagram for the acquisition component of the LabView code is given in Fig. A.1.

The camera itself, is controlled via Mikrotron's Camera Control software. In addition, a camera file is required to configure the camera. The camera is integrated into LabView via the Measurement and Automation Explorer (MAX) tool. Images captured in real-time from the camera are continuously enqueued and output from the acquisition part towards the processing part.

Processing Part

The block diagram for the processing component of the LabView code is given in Fig. A.2. Enqueued images are input into the block, which is executed when the number of enqueued images reaches the desired number. When executed, the images are dequeued. From here A-Scans or B-scans produced via an FFT can be displayed. For further processing in MATLAB the images are exported as a stack of TIFF images.

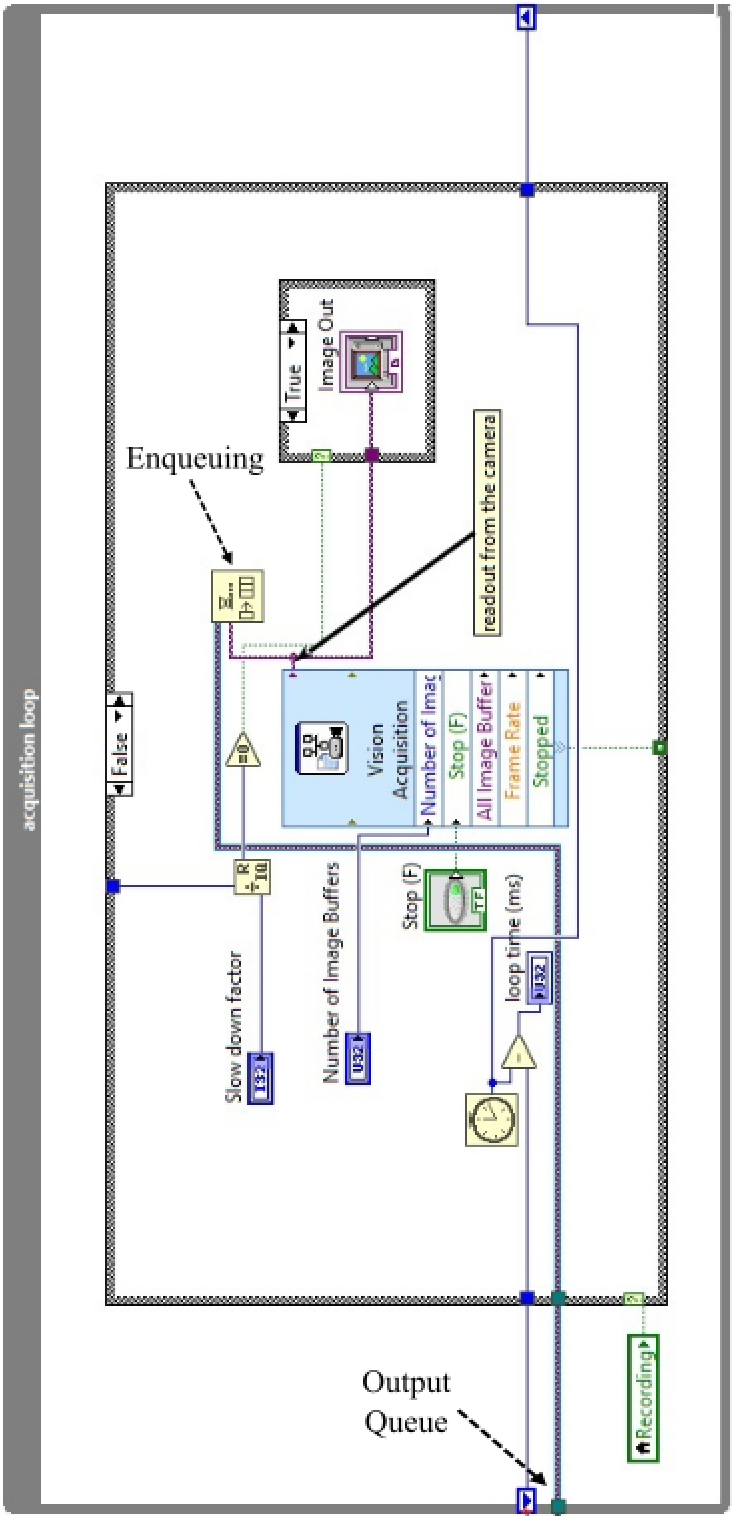

Figure A.1: Screenshot of block diagram for acquisition part of LabView code

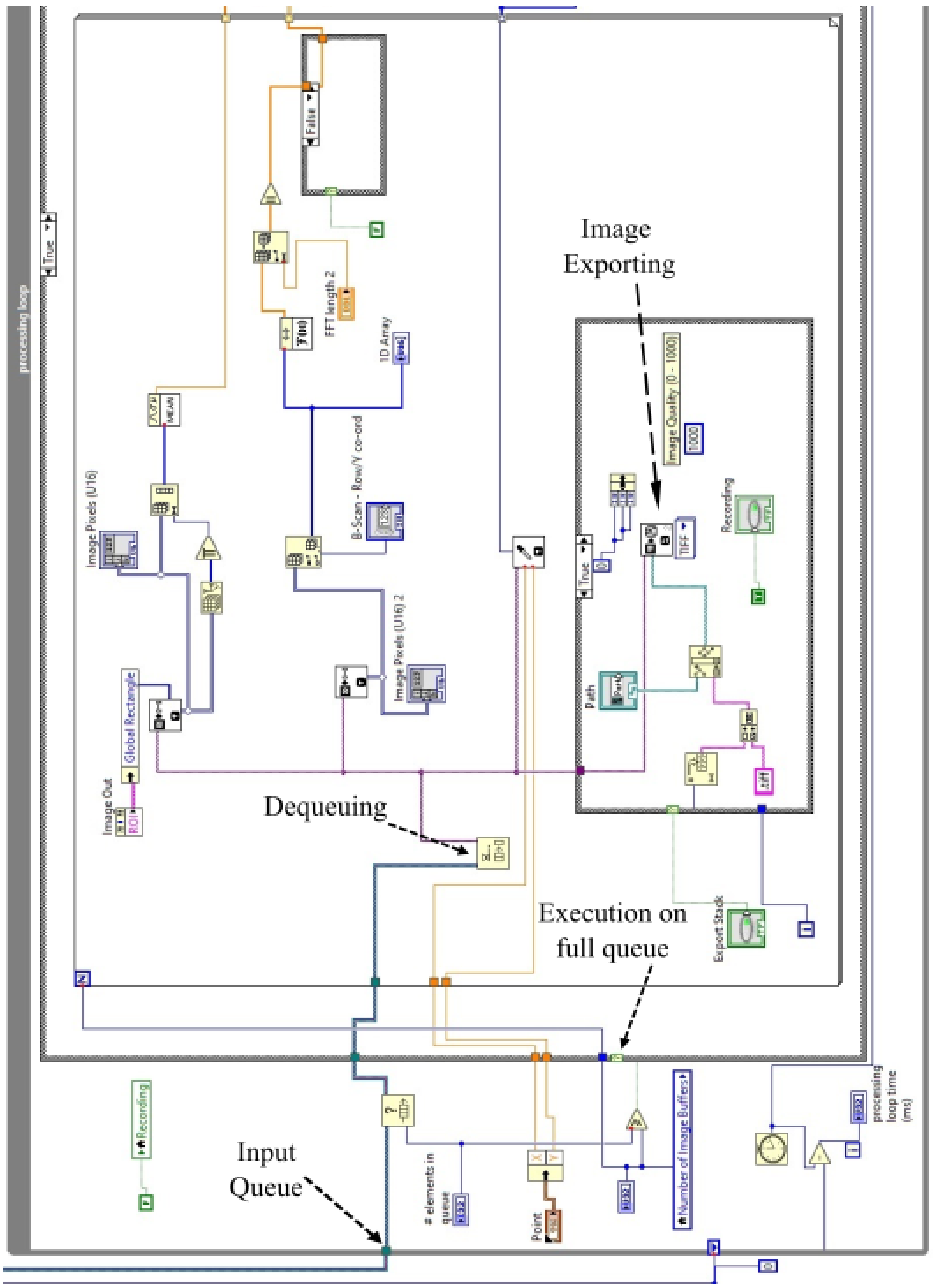

Figure A.2: Screenshot of block diagram for processing part of LabView code.